# LATVIAN JOURNAL of PHYSICS and TECHNICAL SCIENCES

ISSN 0868 - 8257

4

(Vol. 58)

2021

CONTENTS

# LATVIAN JOURNAL of PHYSICS and TECHNICAL SCIENCES

# LATVIJAS FIZIKAS un TEHNISKO ZINĀTŅU ŽURNĀLS

# ЛАТВИЙСКИЙ ФИЗИКО-ТЕХНИЧЕСКИЙ ЖУРНАЛ

Published six times a year since February 1964
Iznāk sešas reizes gadā kopš 1964. gada februāra
Выходит шесть раз в год с февраля 1964 года

4 (Vol. 58) • 2021

RĪGA

Language Editor: O. Ivanova
Computer Designer: I. Begicevs

INDEXED (PUBLISHED) IN

www.scopus.com
www.sciendo.com
EBSCO (Academic Search Complete, www.epnet.com), INSPEC (www.iee.org.com).
VINITI (www.viniti.ru), Begell House Inc/ (EDC, www.edata-center.com).

Issuers: Institute of Physical Energetics,
Institute of Solid State Physics, University of Latvia
Registration Certificate Number: 000700221

Editorial Contacts:
11 Krivu Street, Riga, LV - 1006
Ph.: + 371 67551732
E-mail: leo@lza.lv
www.fei-web.lv

sciendo

LATVIAN JOURNAL OF PHYSICS
AND TECHNICAL SCIENCES
2021, N 4

DOI: 10.2478/lpts-2021-0029

# POWER MODULE TEMPERATURE IN SIMULATION OF ROBOTIC MANUFACTURING APPLICATION

O. Bormanis*, L. Ribickis

Institute of Industrial Electronics and Electrical Engineering
Riga Technical University,
12-k1 Azenes Str., Riga, LV-1048, LATVIA
*e-mail: oskars.bormanis@gmail.com

The paper presents a lifetime consumption estimation model of 6 degrees of freedom industrial robot arm. The primary goal of the research is to provide estimated lifetime data of semiconductor power modules of robot axis power supply circuit, providing new opportunities for cost-saving, predictive maintenance, with highly customized input for different manufacturing applications. Evaluation of thermal stress and estimation of isolated gate bipolar transistor current are completed, based on MATLAB model translating KUKA robot program code to electrical energy consumption, which is a novel approach. Energy losses are considered in the model to provide accuracy of the inverter load current. The simulation results prove that lifetime consumption depends on a robot application type, for more agile movement programs with large power amplitudes, such as handling, the degradation in power modules is significant compared to slower applications, such as gluing or welding. Various options for future development are suggested and considered in the paper.

***Keywords****: Industrial application, lifetime, mission profile, reliability robotics.*

## 1. INTRODUCTION

Selecting operating parameters of electric components is critical for electrical equipment. During the design phase, it is decided what derating method to apply for the required material types. Maximal values are selected to perform safely above the expected operational field life stress, providing a reliability improvement for mission-critical applications, either in a harsh environment, difficult to access or with high downtime costs.

Due to high cost, there is a requirement for semiconductor power modules to decrease absolute maximum values and to

select the material which just barely exceeds the required parameters. As a compromise between cost and performance is required, knowledge and understanding of mission profile are of major importance.

As manufacturing site development is becoming increasingly virtual, and with the introduction of virtual commissioning software, the mission profile is not just an assumption. Process flow and trajectories are set up in a virtual environment during the design phase before deployment with programs as *Delmia Robotics* (*Dassault Systemes*) [1], *RobotStudio* (*ABB*) [2], *Kuka.sim* (*KUKA AG*) [3]. Output code is ready for upload on hardware on-site, as long as the code generation is completed, including the vendor-specific realistic controller simulation module. Virtual machine plugin [4] is launched in a virtual commissioning software environment to generate the same movement as a realistic controller.

In addition to trajectory and process simulation, energy consumption models are developed providing the team with data of expected power consumption of industrial robots and their tools through the manufacturing process. The model discussed in this paper is based on a robot programmed in KUKA robot language that further extends the possibilities of robot trajectory processing to estimate the lifetime of robot semiconductor power modules depending on the intensity of movement program.

The paper investigates the impact of the realistic industrial robot mission profile on junction temperature and lifetime estimation until failure. Robot axis drive inverter isolated gate bipolar transistor junction (IGBT) temperature is calculated from mission profile-specific data set available from the energy consumption model. The input of lifetime estimation model is IGBT junction temperature, where junction temperature swings accelerate packaging degradation due to thermal expansion coefficient mismatch between adjacent materials.

## 2. SIMULATION STUDY

Simulation of energy consumption of industrial robots is a valuable tool for manufacturing site planning, as it is a tool for operation scheduling between multiple robots and trajectory planning for cost-effective production. Lifetime of the developed program is predicted 7 years of production, which is a common cycle in the automotive manufacturing industry; therefore, even minor efficiency improvements provide cost saving through the operating period.

There is a relationship between energy efficiency and reliability, as more efficient power consumption profile is less demanding for electronics of the robot power circuit. In addition, data from the model can provide other possibilities for reliability engineers considering the long-term performance of the system.

The novelty of the research is the calculation of lifetime consumption for power electronics modules of industrial robot inverter, depending on the created robot program and trajectory. Electrical data are known from the mechatronic model of robot, and trajectory is generated by a realistic controller simulation module, degradation of components as well as maintenance intervals can be considered.

Power consumption varies depending on the combined weight of tool and robot application type. It is assumed that degradation of components varies as well, due to the

increased thermal loading on power electronics components, accelerating wear-out of solder joints and bond-wires. More agile application programs (handling, clinching, spot-welding) move or align parts quickly, while slow programs are limited by process quality such as adhesive bonding or painting. Accelerating to higher velocity requires creating larger amplitude power consumption peaks compared to lower velocity, and generates higher power peaks during deceleration as well. Increased kinetic energy provides larger recuperated energy during regenerative braking of robot axis motors.

Sample of KUKA KR220 6-DOF industrial manipulator welding program was generated with the realistic controller simulation module and simulated in kinematic and mechatronic model with different tool mass and analysed for the purpose of the research. Further simulation of handling, clinching and adhesive bonding (gluing) robot programs was conducted to review effects of various mission profiles on inverter semiconductor switch junction temperature.

Differences in simulated combined power consumption of robot motors during the same program with tool mass of 0 kg and 180 kg are shown in Fig. 1, resulting in a 5.9 % difference of average power consumption. More detailed research of robot load weight effect on robot power consumption is available in [4].

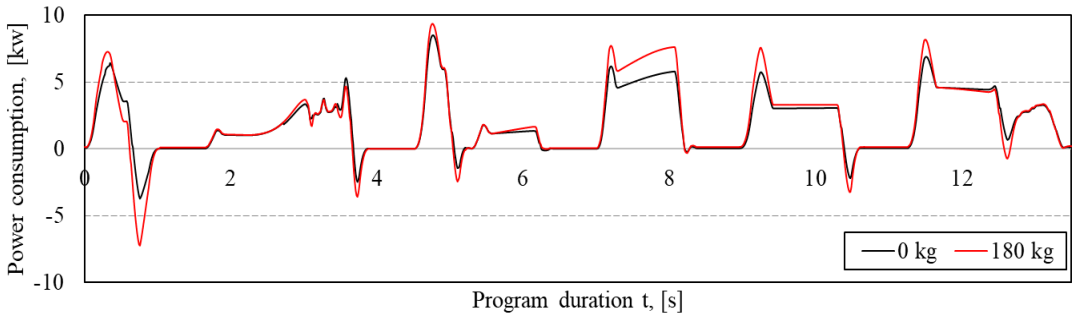


*Fig. 1*. Changing load weight effect on combined power consumption of industrial robot motors during sample welding program.

Mission profile translation from robot code to junction temperature of IGBT is required in order to estimate the lifetime of the power module. The model offers translation from movement path to electrical energy consumed or generated values during the robot movement profile. System performance calculations are supported by a mathematical model, being able to transfer data to and from virtual commissioning software through an application programming interface. In addition to the translation mechatronic model flow, calculation of power losses in inverter and IGBT and calculation of IGBT junction temperature and temperature change are performed as shown in Fig. 2.

The trajectory in the applied model is generated by KUKA specific realistic controller simulation module. The output of trajectory calculation is a file with axis rotation values in degrees. The next step of calculations and further transformation to electrical power losses within the virtual model of robot mechatronic hardware is supported by freeware Robotics Toolbox for MATLAB [5], [6]. Support of differential motion, 3D and 2D transformation functions from this toolbox is involved in data processing within the mechatronic robot model, providing an output of robot torque values.

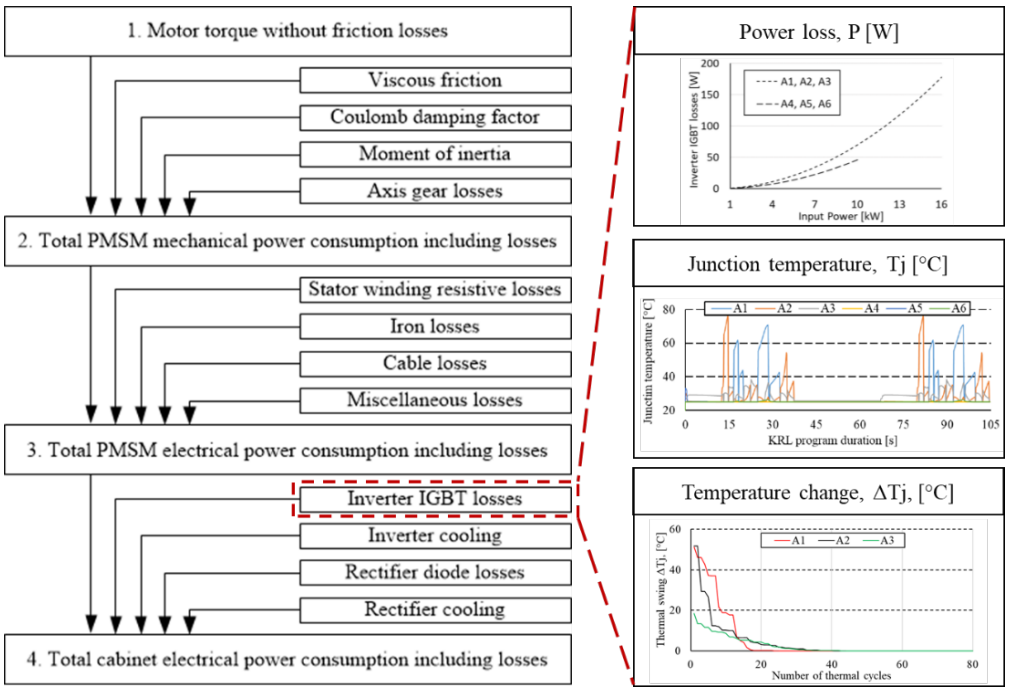


*Fig. 2.* Structure of electrical power consumption in a mechatronic model of the robotic system including mechanical and electrical losses, with capabilities to simulate the thermal profile of inverter semiconductor hardware.

Translated torque values of the simulated sample welding mission profile for each of robot axes through the program duration are shown in Fig. 3, being an input to further calculations in the model. The torque of axes 1–3 is higher, as they have to move more weight through movement, while axes 4–6 have to move significantly less weight; therefore, less torque is required.

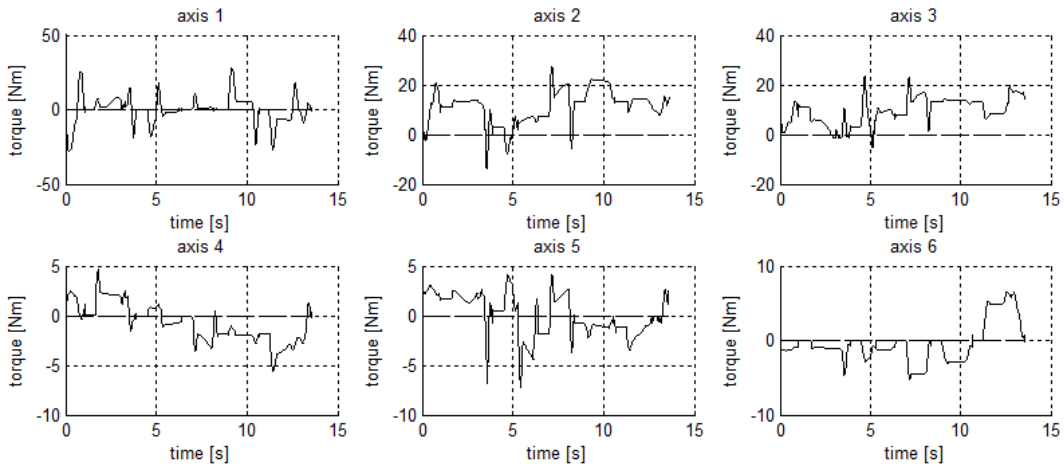


*Fig. 3*. The plot of translated axis torque values of six degrees of freedom industrial robot program code completing welding operation.

Graphics functions, kinetic and dynamic models are just some of the options provided by the toolbox. 3D visualization is integrated into the model presented in this paper to review the specifics of analysed movement and support path planning and optimization research (see Fig. 4-a).

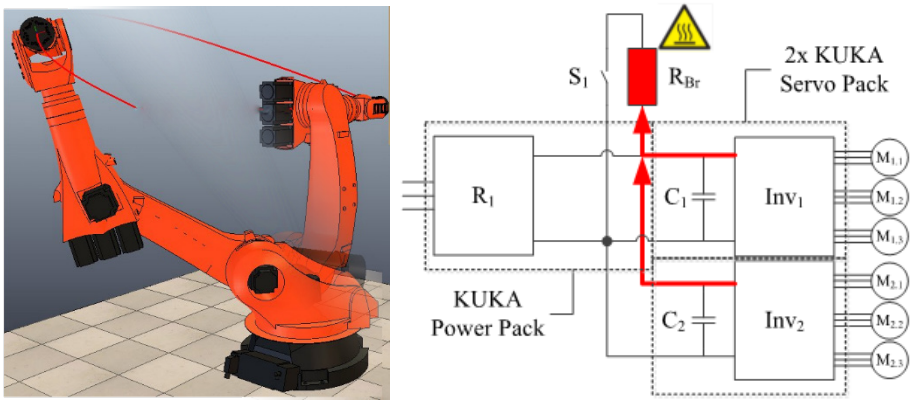


(a) (b)

*Fig. 4.* Sample visualization of V-REP of robot program generated by the realistic controller simulation module with an imported 3D model of the manipulator (a). Typical layout of industrial robot system with single supply during regenerative braking dissipating energy in brake chopper (b).

Torque translation of robot movement axis without any mechanical losses is an input to a robot mechanical model, where additional losses such as friction, inertia, gear losses are considered and calculated [7]. Multiple robot models are supported, with their mass data available for robot links.

Tool weight and mass center are considered in simulation, affecting the instantaneous torque values of robot motors, since increased weight requires more electrical energy to accelerate to the same velocity, and generates more electrical energy during deceleration.

Mechanical torque with losses from robot drive is supplied as an input data to an electrical model of the selected industrial robot. Stator resistive losses, iron and cable losses of permanent magnet synchronous motors are considered at this stage of calculations.

After electrical losses of motors are added, all of the required input data to simulate electric cabinet (see Fig. 4-b) of the industrial robot are available. Cabinet simulation includes motor current, DC bus voltage, current energy stored in the capacitance of DC bus, brake chopper status and losses, as well as inverter and rectifier power losses.

As shown in Fig. 5, combined motor current consumption from DC bus peaks during acceleration, and is zero during deceleration, since no current is consumed when decelerating. The robot is keeping the angular position of its axes during six spot welding operations by holding motors in a fixed position for 0.6 seconds. Depending on the gravity force at each location, more or less current will be consumed during standstill.

Simulated electric cabinet of an industrial robot is a rectifier-inverter permanent magnet synchronous motor drive system with DC link, supported by external capacitance for energy storage and brake chopper for overvoltage protection. Voltage is recti-

fied by KUKA Power Pack (rectifier unit) and inverted by KUKA Servo Pack (inverters), which return rectified voltage to DC link during regenerative braking.

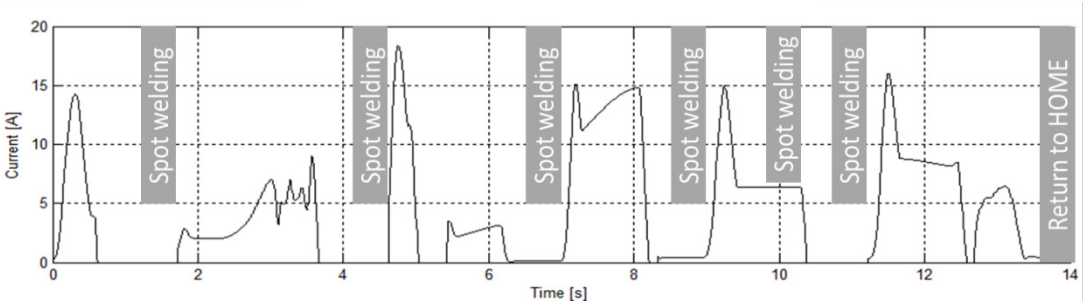


*Fig. 5.* Current in DC bus of the simulated system during sample welding operation with six scheduled spot-welding operations.

Each motor of the robot has its own inverter to control its operation, as shown in the principal power supply layout of KUKA industrial robot in Fig. 6. Six inverters are grouped in two KUKA Servo Pack units by the rated current. Axes 1–3 are supplied by inverters with the rated current of 40 A, while the rated current of inverters that supply axes 4–6 is 20 A. This separation in groups is done since the load on the first three axes is significantly higher, as they are supporting the weight of the robot, tool and load. Axes 4, 5 and 6 control the approach angle of the tool and could be considered for fine-tuning of the movement.

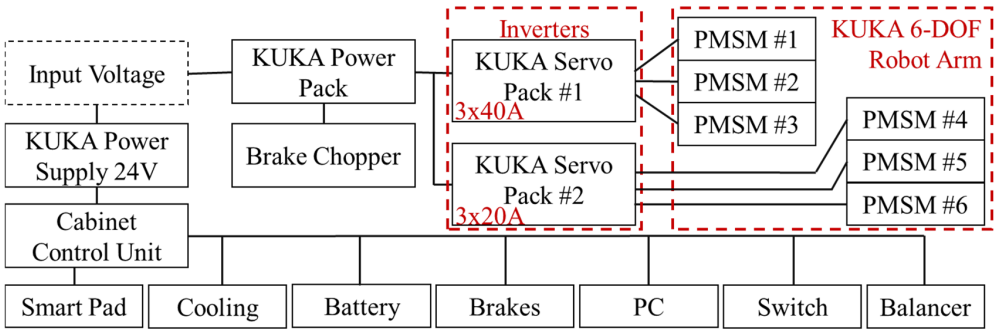


*Fig. 6.* Power supply circuit of KUKA industrial robot, including 2 KUKA Servo Pack modules to support the drive of robot axes.

For junction temperature estimation, the electrical losses of motors and input voltage of the DC bus change in time during robot movement are considered a mission profile. It contains data of current consumption for each of 6 degrees of freedom robot axis electric motors, as the motor current is supplied directly through semiconductor power modules of the inverter.

While mission profiles have the same constraints to maximal current consumption limited by hardware, different industrial robot applications will result in changing acceleration or deceleration slopes, duration, and other key parameters. In the presented model, the mission profile consists of six robot axis motor current consumption data in millisecond steps, through robot program duration. See sample motor current profile of each robot axis in Fig. 7-a.

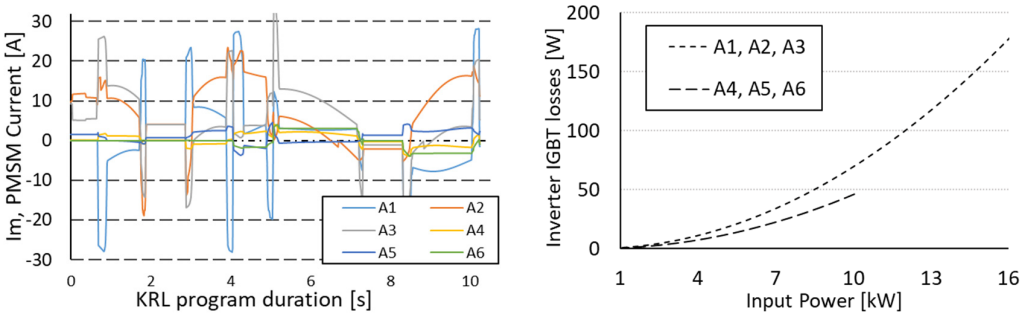


(a) (b)

*Fig. 7.* The current of robot motor supplied through inverters of each robot axis (a). Inverter IGBT losses as a function of input power (b).

The current model evaluates inverter performance data to determine and estimate the lifetime of electronics hardware. Isolated gate bipolar transistor power losses are inverter power level dependent – higher power consumption leads to higher losses at semiconductor power modules. IGBT losses relationship to input power is illustrated in Fig. 7-b. Switching and resistive losses are estimated from the motor current of each axis considering the defined efficiency values, as shown in Eq. (1). In this model, anti-parallel diode efficiency is not separated from the power module. Constant KUKA Servo Pack operating losses not related to isolated gate bipolar transistors are included in the inverter power loss calculation model as well.

$$\sum_{i=0}^{t} P_{cabinet}(i) = \sum_{i=0}^{t}\left( P_{PMSM}(i) + P_{inv_N}\left(\eta_{inv_{KSP}}\left(\frac{I_m(i)}{I_{inv_N}}\right) + \eta_{inv_{IGBT}}\left(\frac{I_m(i)}{I_{inv_N}}\right)^2\right)\right), \quad (1)$$

where

$P_{cabinet}$ – power consumption for each axis after addition of inverter losses (in W);
$P_{PMSM}$ – power consumption for permanent magnet synchronous motors of the robot for each axis (in W);
$I_m$ – motor current supplied through an inverter for each axis (in A);
$P_{inv_N}$ – rated power consumption of KSP for each of 6 axes (in W);
$I_{inv_N}$ – rated current of KSP (in A);
$\eta_{inv_{KSP}}$ – efficiency loss of KSP inverter not related to IGBT per inverter unit;
$\eta_{inv_{IGBT}}$ – efficiency loss of KSP inverter related to IGBT per inverter unit;
t – KRL program duration (in ms).

Further transformation of mission profile data is achieved by translation of instantaneous IGBT module electrical power losses to junction temperature, through the electro-thermal model of the semiconductor power module. To supply a motor of one robot axis, six modules are required and are considered equal regarding the distribution of power losses and other parameters through this model. Rated current and voltage values of industrial robot power modules can reach 75 A, 600 V. Material package type will affect the model outcome, as it must be able to withstand high junction temperature and dissipate high power in losses.

In the electro-thermal model, forced airflow from cabinet fan stabilizes ambient and heatsink temperatures. Total power losses at the IGBT module and anti-parallel diode are considered and included in IGBT/diode junction temperature calculation as shown in Eq. (2). It includes values of various thermal impedances of the module from junction to ambient environment.

$$T_j(t) = P(t) \cdot Z_{th_{j-c}} + P(t) \cdot Z_{th_{c-h}} + P(t) \cdot Z_{th_{h-a}} + T_a(t), \quad (2)$$

where
$T_j$ – junction temperature of IGBT/diode of robot axis drive inverter (in °C);
$T_a$ – the ambient temperature of power module in KUKA Servo Pack (in °C);
P – combined power loss of IGBT/diode module (in W);
$Z_{th_{j-c}}$ – thermal impedance of power module from junction to the case (in °C /W);
$Z_{th_{c-h}}$ – thermal impedance of power module from case to heatsink (in °C /W);
$Z_{th_{h-a}}$ – thermal impedance from the heatsink to ambient environment (in °C /W);
t – KRL program duration (in ms).

Parameters for simulation are obtained from technical datasheet. If the thermal impedance value of anti-parallel diode is available in the datasheet, it allows improving the accuracy of the model. Degradation of IGBT can be considered in the thermal model to improve accuracy as well [8]. Heatsink time delay is not considered in the current translation to junction temperature.

Wear-out of IGBT can be estimated from junction temperature data. Bond-wire damage and die-attach solder fatigue are common failure modes [9]–[11] accelerated by thermal cycling [8] in the field life or during accelerated testing, as they are caused by thermal expansion coefficient differences in package materials, leading from micro-cracks to eventual failure. Die-attach solder joint and bond-wire damage are linked, as degradation of a die-attach joint, lead to failure of bond-wire [12], [13].

## 3. MISSION PROFILE AND JUNCTION TEMPERATURE

Analysis of simulation results confirms a relationship between mission profile power consumption and robot motor inverter IGBT junction temperature. Two scenarios were reviewed during the research presented in this paper – changing tool mass and robot application type.

Junction temperature was compared simulating the same welding program mission profile and modifying tool mass. It was expected that heavier load will increase the junction temperature of IGBT modules. As shown in Fig. 8, the suggestion was confirmed and operating the same profile with heavier tool increased junction temperature. Axes 1–3 revealed a more significant increase in junction temperature as these axes are affected the most by the increase of tool weight, while robot axes 4–6 are less affected by the increased weight, due to the role of approach angle positioning and being less affected by the pull of gravity.

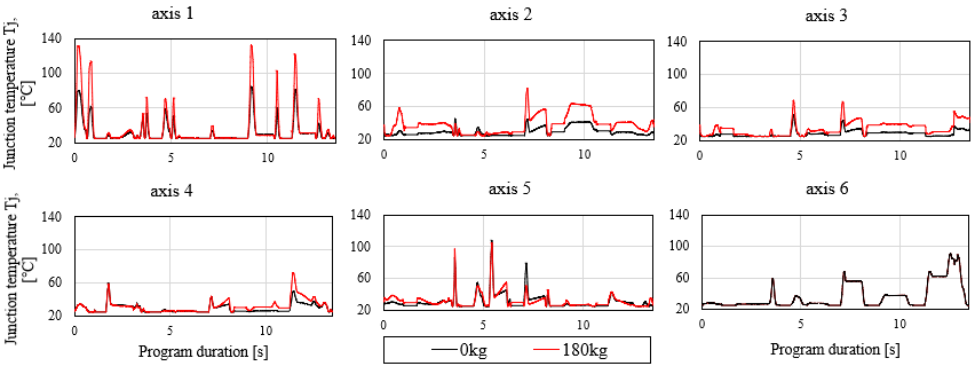


*Fig. 8*. Simulated IGBT junction temperature comparison of industrial robot with various weight tools performing spot-welding program.

IGBT junction temperatures of multiple six degrees of freedom industrial robot programs were simulated and analysed, changing the type of robot program. The expectation of this research is to confirm that more agile robot programs with overall higher velocity and power consumption lead to increased junction temperatures in robot hardware. See Table 1 for more detailed data of simulated robot programs.

**Table 1.** Detailed Data of Simulated Various Application Robot Programs

| Program name | Duration [s] | Tool mass [kg] | Average power [kW] | Program description |
|---|---|---|---|---|
| Handling | 10.25 | 125 | 3.70 | High velocity |
| Clinching | 9.31 | 50 | 2.45 | High velocity, stop & go |
| Spot welding | 13.66 | 180 | 2.65 | High velocity, stop & go |
| Adhesive bonding | 11.10 | 50 | 2.12 | High approach velocity; low velocity, high precision dispensing |

Designed characteristics of handling program are to change location from home location to load pick-up area with the highest velocity, i.e., transport load to processing point, unload, and return to a home position. Access of loading area is easy and does not require a lot of positioning angle adjustment. Handing operation is agile, with high velocity, to avoid creating any production bottlenecks.

Simulated clinching operation is similar to handling program – agile and with high velocity when moving between programmed points. It has five scheduled stop and wait commands through the program to support the clinching operation of the robot tool. Access to operation spots is sophisticated and requires extensive positioning angle adjustment.

Spot welding is agile and with high velocity as well, since moving from one weld location to other is expected to be done as quickly as possible to increase production output quantity. It has 6 scheduled welding spots as mentioned earlier. The main difference between spot welding or clinching from handling operation is more acceleration from complete standstill due to multiple processing points.

Adhesive bonding robot profile is designed manufacturing process speed-sensitive. The robot is approaching gluing location quickly, then moves the glue dispensing tool with process-safe velocity and returns to home location as soon as the glue application is complete.

IGBT junction temperature reaches higher values for programs with higher robot velocity – handling, clinching, also spot welding, as shown in Fig. 9. Temperature peaks during acceleration of axis motor remain steady during steady operating speed and cool down when the axis motor is stopped.

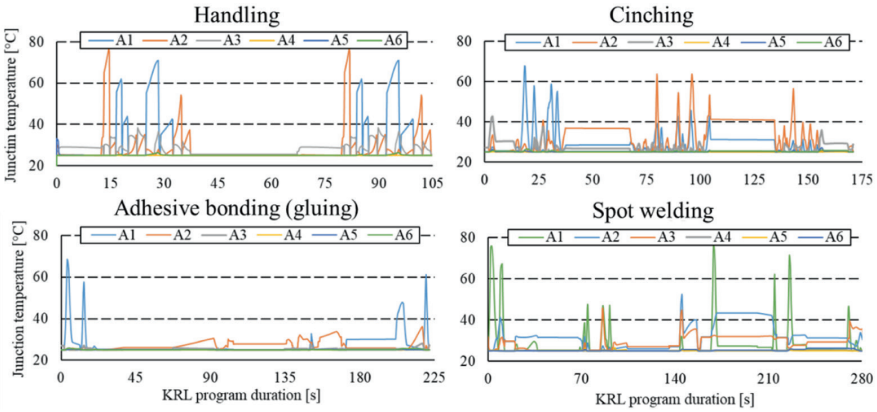


*Fig. 9.* The simulated IGBT junction temperature of each robot axis during sample robot programs in various applications – handling, clinching, adhesive bonding, welding.

To estimate degradation of IGBT modules of industrial robot inverter due to mission profile, calculation of thermal swing $\Delta T_j$ is required. Data from simulated robot programs are further translated, revealing the mission profile potential impact on the remaining lifetime of the semiconductor switch.

As shown in Fig. 10, the gluing operation has the least number of significant junction thermal cycles and amplitudes for robot axes are smaller, since just approach and return to home are completed at high velocity. Graphs of welding and handling operation quantity and amplitudes of thermal swing confirm that higher velocity mission profiles have larger and more significant junction temperature amplitudes. Comparison of simulated clinching program reveals that not only velocity is a factor of thermal degradation, but also start and stop cycles, since it includes multiple cycles to a standstill.

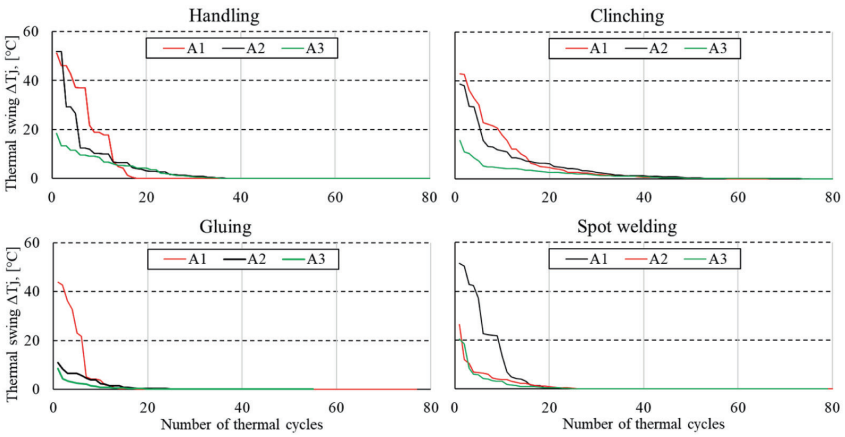


*Fig. 10*. Number of thermal swing amplitudes and cycles during simulated programs of sample robot applications.

## 4. CONCLUSIONS

The novel capability of IGBT junction temperature, thermal swing quantity and amplitude simulation has been added to the mechatronic system model of six degrees of freedom industrial robot. Introduced calculations are intended to be used for IGBT lifetime reduction evaluation regarding various mission profiles translated from robot program code.

While verification of current junction temperature results with field data is not completed, the current model already provides an opportunity to quickly test various remaining lifetime improvement concepts and highlight impact factors such as tool mass, stop-to-standstill cycles, program velocity, average current consumption, and others. Predictive maintenance schedule on-site can be adjusted depending on the robot program profile, as not all hardware has degraded equally.

Development of lifetime consumption models and lifetime distribution based on the developed mission profile translation is scheduled as future work to continue this research.

## ACKNOWLEDGEMENTS

The research has been supported by the Ministry of Economics of the Republic of Latvia, project RTUAER, project No. VPP-EM-AER-2018/3-0004.

## REFERENCES

1. Dassault Systems. (n.d.) *Assembly Robot Programmer*. Available at https://www.3ds.com/products-services/delmia/disciplines/industrial-engineering/
2. ABB, RobotStudio®. (n.d.). Available at https://new.abb.com/products/robotics/robotstudio
3. KUKA AG. (n.d.). *KUKA.Sim*. Available at https://www.kuka.com/en-gb/products/robotics-systems/software/simulation-planning-optimization/kuka_sim
4. Bormanis, O. (2015). Development of energy consumption model for virtual commissioning software. In *56th International Scientific Conference on Power and Electrical Engineering of Riga Technical University (RTUCON),* (pp. 1–4), 14 October 2015, Riga, Latvia.
5. Corke, P. (n.d.). *Robotics Toolbox for MATLAB*. Available at https://petercorke.com/toolboxes/robotics-toolbox/
6. Corke, P. (n.d.). *Robotics Toolbox 10 for MATLAB*. Available at https://petercorke.com/download/27/rtb/1050/rtb-manual.pdf
7. Hansen, C., Öltjen, J., Meike, D., & Ortmaier, T. (2012). Enhanced approach for energy-efficient trajectory generation of industrial robots. In *2012 IEEE International Conference on Automation Science and Engineering (CASE),* (pp. 1 – 7), 20–24 August 2012, Seoul, Korea.
8. Sintamarean, C., Blaabjerg, F., Wang, H., & Iannuzzo, F. (2015). Reliability Oriented Design Tool for the New Generation of Grid Connected PV Inverters. *IEEE Trans. Power Electron.*, *30* (5), 2635–2644.

9. Huang, H., & Mawby, P. A. (2013). A Lifetime Estimation Technique for Voltage Source Inverters. *IEEE Trans. Power Electron., 28*, (8), 4113– 4119.
10. Ciappa, M. (2002). Selected Failure Mechanisms of Modern Power Modules. *Microelectron. Reliab*., *42*, pp. 653–667.
11. Bayerer, R., Hermann, T., Licht, T, Lutz, J., & Feller, M. (2008). Model for power cycling lifetime of IGBT modules various factors influencing lifetime. In *Proc. 5th Int. Conf. Integr. Power Electron. Syst.*, (pp. 1–6), 6–8 March 2008, Nuremberg, Germany.
12. Scheuermann, U., & Hecht, U. (2002). Power cycling lifetime of advanced power modules for different temperature swings. In *Proc. PCIM Nuremberg*, (pp. 59–64), June 2002, Nuremberg, Germany.
13. Lee, W. W., Nguyen, L. T., & Selvaduray, G. S. (2000). Solder Joint Fatigue Models: Review and Applicability to Chip Scale Packages. *Microelectron. Reliab., 40*, 231–244.

sciendo

LATVIAN JOURNAL OF PHYSICS
AND TECHNICAL SCIENCES
2021, N 4

DOI: 10.2478/lpts-2021-0030

# GAS-NEUTRALIZING AND DUST-SUPPRESSING STEMMING OF BOREHOLE CHARGES FOR INCREASING THE ENVIRONMENTAL SAFETY OF EXPLOSION

O. Tverda*, O. Kofanova, O. Kofanov, K. Tkachuk, O. Polukarov, V. Pobigaylo

National Technical University of Ukraine "Igor Sikorsky Kyiv Polytechnic Institute", Institute of Energy Saving and Energy Management,
115 Borshchahivska Str., Kyiv, 03056, UKRAINE
*e-mail: tverdaya@ukr.net

The problem of environmental pollution during the explosive destruction of rocks in order to extract minerals is solved in the article. Two types of borehole charge stemming design have been developed, which, in addition to the function of locking the products of the explosion, allow completely neutralizing harmful gases. The first type is the stemming design, which includes the two-stage purification of harmful gases, formed during the explosive destruction of rocks, and is based on chemisorption of gases by quicklime or production waste and physicochemical sorption (adsorption) by zeolites. Such stemming can provide complete chemical neutralization of $NO_2$ and $CO_2$, as well as neutralization of CO by zeolites, during the explosion. The second type is stemming design, which includes chemisorption of gases by slaked lime. This type of stemming has a number of advantages over the previous one. It can not only provide complete chemical neutralization of $NO_2$, $CO_2$ and CO, but also allows abandoning zeolites, which significantly reduces the cost of its formation to obtain the effect of "irrigation" of the dust and gas cloud, which reduces the concentration of dust in the air after the explosion to provide a higher degree of conversion. The paper determines quantitative and qualitative characteristics of the adsorbent composition of the two types of stemming depending on the type of explosive, the amount and type of harmful gases formed during explosion, and the parameters of the borehole.

***Keywords:*** *Borehole charge, environmental pollution, explosion, explosive, harmful gases, neutralization of gases, stemming.*

## 1. INTRODUCTION

The mining industry is one of the main industries in many countries of the world. During the extraction of solid (strong) minerals, blasting operations are an integral part of the preparation for excavation. A large volume of gas and dust is produced during the blasting operation, especially in quarries, and then released into the atmosphere (Table 1). Commercial explosives are the major sources of pollutants. There is maximum detonation energy for destruction of the rock mass and minimum of harmful gases if the oxygen equilibrium of the explosive is zero. If the oxygen balance of the explosive deviates from zero gases caused by detonation can appear in the form of steam, carbon dioxide, nitrogen and some toxic and harmful gases, such as nitrogen monoxide, nitrogen dioxide and carbon monoxide [2].

During the interaction between oxides of nitrogen (except NO) and carbon (IV) oxide with water vapor, aerosols of nitric, nitrous and carboxylic acids are formed, the deposition of which on the soil leads to an increase of nitrates, nitrites and carbonates in it, and during entering water bodies – to acidification of water. Oxidizing hemoglobin to methemoglobin, nitrates and nitrites disrupt its transport function. Carbon (II) oxide, in turn, causes poisoning of the body due to the formation of carboxyglobin in the blood and thereby blocking the transport of oxygen. Carbon dioxide is one of the greenhouse gases and is involved in global warming [3].

It should be noted that the simultaneous formation of harmful gases and dust during the explosion is accompanied by the adsorption of these gases by the developed surface of dust particles [4]. These toxic gases pollute the mining area and its adjacent environment, which can endanger humans (workers), animals, and plants. A new blasting pattern and the controlling methods for the pollutants, especially by changing the stemming materials and length, can provide a safe environment for the ecosystem [2].

It is known that the efficiency of the explosion is largely determined by the parameters of the stemming [5]. Its volume and quality determine the level of explosive energy using to destroy the rock mass, the uniformity of rock mass fragmentation, as well as the volume of the dust and gas cloud [6]. The main purpose of stemming is to lock the products of the explosion reliably for a time until the secondary reactions of detonation decomposition of the explosive are carried out, and the energy of the expanding gases is converted into mechanical work of destruction and moving of the massif. Along with regulating the intensity of rock crushing, stemming should prevent premature gas ejection from the borehole, which is accompanied by incomplete decomposition of explosion products and leads to an increase in toxic components in the gas mixture, destruction of the wellhead with uncontrolled scattering of individual pieces of rock [5].

As a result of numerous studies, it has been established that the behaviour and efficiency of stemming during mass explosion depend on the physical and mechanical properties of the stemming material, the size of its particles, compression, friction with the walls of the charging cavity etc. [7].

A significant number of scientific papers are devoted to the choice of rational design and material of stemming [7]–[26]. However, mainly the stemming designs, which create the maximum resistance to the ejec-

tion of explosive products, are presented in these papers. At the same time, not enough attention is paid to the ejection of detonation products into the atmosphere through the stemming material [8].

**Table 1.** Estimated Emissions of Harmful Gases from Blasting Operations for the Extraction of the Most Common Minerals in the World

| Mineral | 2019 World production (according to Mineral Commodity Summaries 2020 – USGS, University of Waterloo) | | Specific consumption of explosive, kg/m$^3$ [1] | Volumes of explosives use/ average value, millions of kilograms | The amount of harmful gases (for example, an explosive – Granemit I–30), millions of liters | |
|---|---|---|---|---|---|---|
| | millions of metric tons | millions of cubic meters | | | | |
| Gravel | 50000 | 18519 | 0.7–1.4 | 12963–25927<br>19445 | $CO_2$ | 1516710 |
| | | | | | CO | 525015 |
| | | | | | $NO_2$ | 4083 |
| Iron Ore | 2500 | 481 | | 337–673<br>505 | $CO_2$ | 39390 |
| | | | | | CO | 13635 |
| | | | | | $NO_2$ | 106 |
| Bauxite | 500 | 200 | | 140–280<br>210 | $CO_2$ | 16380 |
| | | | | | CO | 5670 |
| | | | | | $NO_2$ | 44 |
| Lime | 430 | 154 | | 108–216<br>162 | $CO_2$ | 12636 |
| | | | | | CO | 4374 |
| | | | | | $NO_2$ | 34 |
| Gypsum | 140 | 64 | | 45–90<br>68 | $CO_2$ | 5304 |
| | | | | | CO | 1836 |
| | | | | | $NO_2$ | 14 |

In particular, in [9] it has been established that proper application of air-decking and stemming plugs may enhance explosive energy utilization to a good extent. The developed stemming plug has acronym SPARSH and can effectively be used with air-decking. Further, SPARSH does not restrict the type of stemming material and stemming length.

The authors of [10] propose using a shortened to 7–14 diameters of the charge stemming with an air gap under it, which allows you to qualitatively crush the upper part of the ledge and improve rock fragmentation in general. In [7], it is noted that increasing the intensity of rock crushing during explosion can be achieved as a result of application of scattered stemming, which provides not only tight locking of the detonation products in the charging cavity, but also the activation of gas-dynamic processes in the stemming material due to the creation of air gaps in it and the formation of inert rigid inserts.

The authors of [5] have set the dependence between the stemming effectiveness and the shape of its lower end, and size of the air gap between the stemming and the explosive charge. Yurchenko in [6] presents the stemming design based on the use of a rubber stopper with an anchor device. Vorobiov [8] substantiates the effectiveness of combined stemming use in borehole charges with the location in it the S-shaped line of the detonation cord.

A significant number of scientific papers are aimed at substantiating the most effective stemming material for blasting

boreholes. In particular, study [11] aims at assessing the impact of drill cuttings use as stemming on blasting results. The screened drill cuttings having size of 3–7 mm have provided the improved blasting results in terms of reduced gas ejection, less dusty environment, less fly rock, better fragmentation, loose muckpile and reduced explosive consumption.

The authors [12] argue that a correct material and size (length) of stemming can theoretically be determined if the detonation wave is known. In the case that the detonation wave is not available, it is suggested to follow some basic rules. First, it is better to choose a stemming material the impedance of which is greater than that of the explosive. Second, the stemming must be long enough to allow the detonation wave to be kept in the blast hole much longer than the total detonation time after the detonation is completed.

The three new stemming plugs are designed based on literature review and onsite observations by Atta Ur Rehman. In terms of ease of operation and utilization plastic molded stemming plugs have been better than quick setting cement and air-plugs. From the economic point of view, quick setting cement has been the best one. All of the stemming plugs have reduced the volume of secondary blasting [13].

In [14], the effect of different stemming types on the results of the explosion has been researched. Stemming types have been ranged from sand to various sized limestone. Use of different particle sizes of stemming material has shown a significant decrease in stemming ejection velocity than the use of increased particle sizes.

In [15], the developed plaster stemming method is researched and compared with the usual dry drill cutting stemming method for surface blasting in quarries. Dry drill cuttings eject very easily from blast holes without offering much resistance to blast energy. The plaster stemming method has been found to be better than the drill cutting stemming method due to the increased confinement inside the borehole and better utilization of explosive energy in the rock. The main advantage of the new stemming method is the reduction in the cost of blasting.

The recording of the blasting with the high-speed camera during testing surfactants as stemming has allowed observing the behaviour of these mixtures. The "mushroom effect" during blasting has shown that the mixture is able to retain dust closer to the ground, avoiding vertical dispersion and subsequent transport due to wind. The addition of glycerin to the mixture in the laboratory has proven to improve the surfactant characteristics, so its use has been recommended [16].

The authors [17] have developed stemming, which consists of a low-density porous material and a layer of drill cuttings. The aim of low-density porous stemming use is to enhance the explosive effect and the possibility of dust suppression. After the borehole is loaded with explosive, the space above the charge is filled with foam gel in the sleeve, the top of the sleeve is filled with drill cuttings. Improved explosive effect is explained by the fact that the propagation velocity of the stress wave has a finite value, and, depending on the blockiness of the massif, amounts to 800–3000 m/s in the rock, 330 m/s in air, and 1500 m/s in water, and in the low-density composition only 30–50 m/s.

However, the known designs of stemming are aimed to a greater extent at improving the efficiency of blasting. Such stemming makes it possible to partially reduce dust emissions, but does not neutralize harmful gases. Developed designs of stemming, which focus on their shape and

size, and which do not take into account the quality of the stemming material in terms of the ability to adsorb harmful gases, are not able to reduce the man-caused load on the environment from a mass explosion. Attempts to solve this problem have been made by the authors of [18]–[26].

In [18], it has been proposed to neutralize harmful gases using slaked lime directly in the stemming above the upper end of the charge. The authors of [4] present the results of experiments to reduce the level of hazardous emissions into the atmosphere during mass explosions due to the use of aqueous stemming with an admixture of steaming solution containing calcium hydroxide $Ca(OH)_2$. Due to this impurity coagulation of dust particles and partial neutralization of toxic gaseous substances are achieved. The optimal concentrations of this solution in internal, external and combined stemming are determined.

The authors of [19] have developed a method of dust and gas suppression during mass explosions using solid stemming moistened with an aqueous solution of a carbonic reagent with a concentration of 1–2 wt. %, and a protective screen in the form of a moistened layer of rocks on the surface of the block. The authors [20] propose adding to the composition of the stemming material salts of alkaline earth metal. The addition of salts of alkaline earth metal will reduce more than 3 times the yield of nitrogen (II) oxide and nitrogen (IV) oxide and more than 2 times carbon (II) oxide during the explosion. The presence of a plasticizer allows for the formation of different shapes of the stemming, which makes it possible to significantly expand the scope of its application. Katanov and Skachilov [21] have proposed filling the space above the explosive charge column with a low-density composition.

The authors of [22] have conducted extensive experimental research of different types of stemming. Higher quality of locking of explosion products by the combined stemming with the embedded element in comparison with the backfill stemming has been confirmed. Leschinsky has developed the design of a universal combined stemming, the spacer element of which is a concrete cone, which is installed in an explosive borehole on the backfill site where drill cuttings are placed [23]. In [24], it has been proven that during the layer formation of the combined stemming with alternating layers of drill cuttings and elements of stone material the resistance of its emission by the pressure of the explosion products increases sharply, which allows you to reduce the length of the stemming by half. Several types of stemming have been developed in [25], in particular: incomplete stemming (with a reduced mass of stemming material), step stemming (the stemming material is scattered in sections by air gaps) and closing charge.

In [26], algorithms for calculating the effect of explosive auxiliary materials on the oxygen balance of the system "explosive – auxiliary materials" are proposed. The influence of auxiliary materials on the enthalpy of the explosion process and the composition of the explosion products is shown on the example of Gramonite 79/21.

As a result of the analysis of technological and design solutions according to existing methods of stemming borehole charges the following should be noted. Stemming with an improved shape or inert gaps along the length or between the stemming and the charge is aimed at increasing the efficiency of the technological process and does not take into account modern requirements for the air of the working area and surrounding areas. In addition, its formation in borehole is quite time consuming. Liquid stemming, in addition to being expensive in terms of

component composition, requires the manufacture of special tanks and fasteners to form it in boreholes. Stemming in the form of a closing charge is used in cases when the upper part of the ledge is composed of stronger and denser rocks in comparison with its lower part. The use of such stemming leads to crushing, sometimes removal of the lower part of the ledge and subsidence of the upper dense part without any destruction. There is a danger of an air shock wave inherent in blasting without stemming. Therefore, the development of universal stemming, which would provide the necessary fractional composition of rock mass, a high level of environmental safety during explosive destruction of rocks, with low labour and financial costs, is an urgent scientific and practical task. The analysis has shown that attempts to reduce the man-made load on the environment during the explosion due to the rational choice of explosive do not provide the necessary results. The choice of explosive with higher environmental performance causes unsatisfactory results of the explosion (a significant amount of oversize, thresholds on the sole of the ledge, etc.) [27].

## 2. THEORY

Based on the possible composition of the dust and gas cloud (CO, $CO_2$, NO, $NO_2$), the authors have developed a stemming design [28], which involves two-stage cleaning of harmful gases during the process of explosive destruction of rocks and is based on chemisorption of gases by quicklime and physicochemical sorption (adsorption) by zeolites.

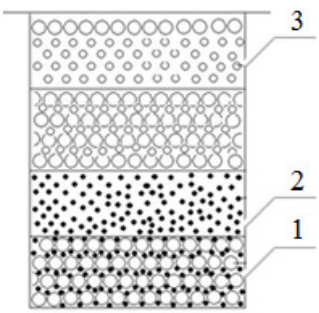


*Fig. 1.* The stemming design with two-stage cleaning of harmful gases: 1 – gravel; 2 – quicklime or waste containing it; 3 – zeolites or slags [28].

During the first stage, special attention is paid to the chemisorption of nitrogen (IV) oxide by quicklime, while other gases in a certain amount will be further adsorbed by zeolite (Fig. 1). It should be noted that during the first stage it is important to completely chemisorb $NO_2$. First, $NO_2$ is the most harmful component, and, secondly, it is able to form dimers $2NO_2 \leftrightarrow N_2O_4$, due to which its adsorption by zeolites can be significantly complicated.

Chemisorption of nitrogen (IV) oxide by quicklime during an explosion is described by the following reactions:

$$2NO+O_2=2NO_2,$$
$$2NO_2+CaO=0{,}5Ca(NO_2)_2+0{,}5Ca(NO_3)_2,$$
$$2N_2O_4+2CaO=Ca(NO_2)_2+Ca(NO_3)_2.$$

If we take into account that 50:50 % $2NO_2 \leftrightarrow N_2O_4$, the chemisorption of $NO_2$ by 1 kg of CaO is 0.6 $m^3$. Taking into account the degree of chemisorption (~ 99 %), the volume of chemisorbed gas decreases to 0.594 $m^3$.

As for CO, this oxide is non-salt-forming, and therefore does not react directly with CaO. However, during an explosion and in the presence of oxygen in the air, such processes are possible:

$$2CO+O_2=2CO_2,$$
$$2CO_2+2CaO=2CaCO_3.$$

For a precise calculation, the degree of conversion is taken into account by the reaction $2CO+O_2=2CO_2$. It is assumed that this reaction takes place with $\eta = 0.7$ (70 %), as there is a possibility of lack of oxygen. Taking into account the degree of conversion by this reaction of 70 %, 0.7 $dm^3$ is obtained, i.e., 0.7 liters of $CO_2$ are formed from each liter of CO.

Taking into account the reaction of quicklime with carbon (IV) oxide:

$$CaO+CO_2=CaCO_3,$$

it is calculated that 1 kg of CaO chemisorbs 400 $dm^3$ of $CO_2$. Taking into account the degree of conversion $\eta$=0.99, 1 kg of CaO theoretically chemisorbs 396 $dm^3$ of $CO_2$.

Conclusions on the degrees of conversion of nitrogen (IV) oxide and carbon (IV) oxide by quicklime are based on the values of the activation energy $E_A$ of these processes. Since the values of $E_A$ range from 40 kJ/mol to 100 kJ/mol, most of the collisions of the reacting particles lead to a chemical interaction, and, consequently, the reaction rate is very high. In addition, due to the explosion, the dispersion of the system increases sharply, and, consequently, the area of the interfacial surface increases, which, in turn, increases the rate of the interaction of the reacting particles.

Based on our research to increase the environmental safety level of the explosive destruction of rocks, the developed stemming design has been improved. The new stemming design is based on chemisorption of gases by calcium hydroxide (Fig. 2). Slaked lime as a suspension of dense consistency is proposed to pour directly into the borehole after the formation of the charge. To prevent the penetration of the suspension into the explosive, in the case of its placement without a sleeve, it is proposed to form a special "filling" in each borehole, on which the pre-prepared suspension of calcium hydroxide will be poured. The formation of the "filling" does not require significant labour and financial costs, as it is based on the addition to the suspension of slaked lime $Ca(OH)_2$ methylcellulose $C_6H_7O_2(OH)_x(OCH_3)_y$ or sodium silicate $Na_2SiO_3$ with the formation of calcium silicate ("filling") and sodium hydroxide, which, in turn, will actively neutralize nitrogen oxides and carbon dioxide:

$$Na_2SiO_3+Ca(OH)_2=CaSiO_3+2NaOH,$$
$$2NO_2+2NaOH=NaNO_2+NaNO_3+H_2O,$$
$$2NaOH+CO_2=Na_2CO_3+H_2O.$$

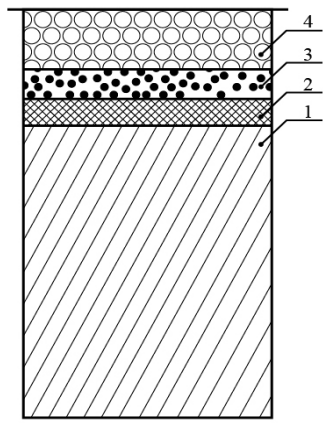


*Fig. 2.* The borehole charge stemming design, which includes chemisorption of gases by slaked lime: 1 – explosive; 2 – "filling"; 3 – slaked lime suspension of dense consistency; 4 – gravel.

The next and last step in the formation of the stemming is backfilling the gravel to increase the resistance of the ejection of stemming by detonation products.

$$2Ca(OH)_2+4NO_2=Ca(NO_2)_2+Ca(NO_3)_2+2H_2O,$$
$$2NO+O_2=2NO_2,$$
$$2NO_2+Ca(OH)_2=1/2Ca(NO_2)_2+1/2Ca(NO_3)_2+H_2O,$$

$Ca(OH)_2+CO_2=CaCO_3+H_2O$,

$2CO+O_2=2CO_2$,
$2CO_2+2Ca(OH)_2=2CaCO_3+2H_2O$.

The use of slaked lime suspension as a chemisorbent will allow not only neutralizing harmful gases formed during the explosion, but also providing the effect of irrigation of the dust and gas cloud, which, in turn, will reduce the concentration of dust in the air, as at a temperature above 520 °C:

$Ca(OH)_2=CaO+H_2O$.

In addition, calcium hydroxide reacts with carbon monoxide at a temperature of about 400 °C, which allows abandoning zeolites compared to the use of calcium oxide as a chemisorbent:

$Ca(OH)_2+CO=CaCO_3+H_2$.

## 3. RESULTS AND DISCUSSION

The results of calculating the amount of harmful gases that 1 kg of CaO and 1 kg of $Ca(OH)_2$ can chemisorb are given in Table 2. According to [29], the amount of gases formed from 1 kg of explosive is ($dm^3$/kg): $NO_2$ – 0.21; CO – 27; $CO_2$ – 78; $N_2$ – 215. Given that the diameter of the borehole is 250 mm, the diameter of the charge – 160 mm, the length of the borehole – 16 m, the length of the charge – 12 m and the length of the stemming – 4 m, the amount of gases from 1 borehole will be ($dm^3$): $NO_2$ – 60.9; CO – 7830; $CO_2$ – 22620; $N_2$ – 62350.

The total mass of CaO required for the planned chemisorption volumes will be:

$m_{CaO}=0.1+57.1+13.8=71$ kg.

Thus, 2349 $dm^3$ of CO should be adsorbed by the zeolite.

The total mass of $Ca(OH)_2$ required for the planned chemisorption volumes will be:

$m_{Ca(OH)2}=0.1+75.4+36.9\approx112$ kg.

**Table 2.** Volumes of Chemisorption of Gases Formed during the Explosion by One Kilogram of Quicklime and One Kilogram of Slaked Lime

| Gas formed during the destruction of rocks by explosive | The volume of gas chemisorption by 1 kg of CaO, $dm^3$ | The volume of gas chemisorption by 1 kg of $Ca(OH)_2$, $dm^3$ | The degree of conversion |
|---|---|---|---|
| $NO_2$ | 594 | 450 | 0.99 |
| $CO_2$ | 396 | 300 | 0.99 |
| $CO_2$ formed by the reaction $2CO+O_2=2CO_2$ | 396 | - | 0.70 |
| CO | - | 212 | 0.7 |

According to experimental literature data [30] for NO (and the adsorption of CO is similar due to the similar size of the molecules), 1 g of zeolite (KA) adsorbs (maximum) 0.35 g of CO or 0.28 $dm^3$. Therefore, 8389.29 g or 8.4 kg of zeolite are required to adsorb 2349 $dm^3$ of CO.

Given that with increasing temperature physical adsorption deteriorates, the mass of zeolite, in the case of quicklime,

it is proposed to double (17 kg). This takes into account not only the physicochemical adsorption processes during the explosion, but also the subsequent adsorption on zeolites, which will be in a suspended state for a long time (according to experimental data, the dust cloud in sedimentary dry weather will sediment (settle under the action of gravity) for 3−3.5 hours or more). At the same time, the degree of dispersion of the system during the explosion will cause an increase in the interfacial surface of the reacting particles and, as a consequence, an increase in the degree of conversion (adsorption) of carbon monoxide. Under these conditions, the sorption of oxygen and nitrogen in the air can be neglected due to the very small size of their molecules and, therefore, due to their insignificant adsorption on the pore surface of the zeolite.

Thus, based on the calculation of the required amount of adsorbent at each stage of purification and justification of its feasibility, the quantitative and qualitative characteristics of the adsorbent in stemming depending on the type of explosive, the amount and type of harmful gases formed during the explosion and borehole parameters have been obtained:

$$m_{CaO} = \frac{\pi}{4}\rho_{ex} d_{ch}^2 l_{ch}\left[\frac{V_{NO_2}}{594} + \frac{V_{CO_2}}{396} + \frac{0{,}7V_{CO}}{396}\right], \quad (1)$$

$$m_z = \frac{\pi}{2}\rho_{ex} d_{ch}^2 l_{ch}\,\frac{0{,}3\cdot V_{CO}}{1000\cdot n}, \quad (2)$$

$$m_{Ca(OH)_2} = \frac{\pi}{4}\rho_{ex} d_{ch}^2 l_{ch}\left[\frac{V_{NO_2}}{450} + \frac{V_{CO_2}}{300} + \frac{V_{CO}}{212}\right], \quad (3)$$

where $\rho_{ex}$ – density of explosive, kg/m$^3$; $d_{ch}$ – charge diameter, m; $l_{ch}$ – charge length, m; $V$ – volume of relevant harmful gas from 1 kg of explosive, dm$^3$/kg; $n$ – adsorption capacity of 1 g of zeolite, dm$^3$.

If it is necessary to prepare a special "filling" (if the explosive in the borehole is placed without a sleeve and stemming is based on use of $Ca(OH)_2$), an additional suspension of calcium hydroxide of dense consistency is required. For the given parameters of a charge design the rational length of a "filling" is 30 cm. Taken into account that the density of calcium silicate is 2.9 g/cm$^3$, it is calculated that the required amount of slaked lime suspension to form a "filling" of the required size is 28 kg, and sodium silicate – 46 kg.

The results of calculations of the mass of quicklime, slaked lime and zeolites for complete neutralization of harmful gases are given in Table 3. The diameter of the borehole – 250 mm, the length of the borehole – 16 m, the charge diameter – 160 mm, the length of the charge – 12 m. The required amount of zeolite of each grade is calculated according to their absorbency in compliance with [30].

Thus, the two-stage purification of harmful gases using the stemming design, which includes chemisorption of gases by quicklime and physicochemical sorption (adsorption) by zeolites, can provide complete

chemical neutralization of $NO_2$ and $CO_2$, as well as neutralization of CO by zeolites. The improved stemming design, which includes chemisorption of gases by slaked lime, not only provides complete chemical neutralization of $NO_2$, $CO_2$ and CO, but also allows abandoning zeolites, which significantly reduces the cost of its formation, to obtain the effect of "irrigation" of the dust and gas cloud, which reduces the concentration of dust in the air after the explosion in order to provide a higher degree of conversion.

In addition, such stemming must be taken into account when choosing a rational type of explosive for blasting under specific mining and geological conditions. With the implementation of the proposed stemming design in combination with the resource-saving design of the charge [31], it is possible not only to avoid or minimise the tax on pollutant emissions, but also to increase the efficiency of explosion and prevent mineral losses.

**Table 3.** The Required Amount of Reagent and Sorbent for Complete Neutralization of Harmful Gases during Detonating of Modern Explosives

| Explosive | Density of explosive, kg/m$^3$ | The amount of gases formed from 1 kg of explosive, dm$^3$ | | Required amount of lime, kg | | The required amount of zeolite (when stemming is based on use of CaO), kg | | |
|---|---|---|---|---|---|---|---|---|
| | | | | CaO | $Ca(OH)_2$ | KA | 13X | LiLSX |
| Polimiks GR4-T10 | 872 | $CO_2$ | 52.64 | 59 | 119 | 37 | 34 | 33 |
| | | CO | 82.66 | | | | | |
| Polimiks GR1/8 | 875 | $CO_2$ | 64.85 | 42 | 64 | 8 | 8 | 7 |
| | | CO | 18.48 | | | | | |
| Kompo-lait GS6 | 852 | $CO_2$ | 39.45 | 39 | 76 | 22 | 20 | 19 |
| | | CO | 50.02 | | | | | |
| Polimiks GR1/8 (74 %) + KRUK2 (26 %) | 1000 | $CO_2$ | 73.14 | 49 | 71 | 6 | 5 | 5 |
| | | CO | 10.7 | | | | | |
| Polimiks GR1/8 (85 %) + KRUK2 (15 %) | 950 | $CO_2$ | 69.99 | 46 | 68 | 7 | 6 | 6 |
| | | CO | 13.62 | | | | | |
| Hranemit I-30 | 1200 | $CO_2$ | 78 | 71 | 112 | 17 | 15 | 15 |
| | | CO | 27 | | | | | |
| | | $NO_2$ | 0.21 | | | | | |
| Hranemit I-50 | 1300 | $CO_2$ | 89.2 | 92 | 151 | 26 | 24 | 23 |
| | | CO | 38.8 | | | | | |
| | | $NO_2$ | 0.12 | | | | | |

## 4. CONCLUSIONS

The stemming design, which includes the two-stage purification of harmful gases formed during the explosive destruction of rocks, and is based on chemisorption of gases by quicklime or production waste that includes it and physicochemical sorption (adsorption) by zeolites, has been developed within the framework of the research. Such stemming can provide complete chemical neutralization of $NO_2$ and $CO_2$, as well as neutralization of CO by zeolites, during the explosion.

It is proposed to improve the developed stemming design by replacing quicklime with slaked lime. The improved stemming design, which includes chemisorption of gases by slaked lime, not only provides complete chemical neutralization of $NO_2$, $CO_2$ and CO, but also allows abandoning zeolites, which significantly reduces the cost of its formation in order to obtain the effect of "irrigation" of the dust and gas cloud, which reduces the concentration of dust in the air after the explosion to provide a higher degree of conversion.

For a borehole with a diameter of 250 mm and a length of 16 m, in which the charge of Hranemit I-30 with a diameter of 160 mm and a length of 12 m is formed, the total mass of CaO required to chemisorb nitrogen (IV) oxide and carbon (IV) oxide is 71 kg, mass of zeolite KA, which is required for complete adsorption of carbon (II) oxide, is 17 kg. Under the same conditions, the required amount of $Ca(OH)_2$ suspension for complete neutralization of all these gases is 112 kg.

As a result, the environmental conceptual framework of explosion by using the gas-neutralizing and dust-suppressing stemming of borehole charges has been developed. The study has identified quantitative and qualitative characteristics of the adsorbent composition of the two types of stemming depending on the type of explosive, the amount and type of harmful gases formed during explosion, and the parameters of the borehole.

## REFERENCES


1. Tverda, O., & Vorobiov, V. (2011). Specific Consumption of Explosives at Destroying the Rocks with Different Properties. *Herald of the National Technical University of Ukraine «Kyiv Polytechnic Institute», Series of «Mining»*, *20*, 52–58.
2. Abdollahisharif, J., Bakhtavar, E., & Nourizadeh, H. (2016). Monitoring and Assessment of Pollutants Resulting from Bench-Blasting Operations. *Journal of Mining & Environment*, *7* (1), 109–118. DOI: 10.22044/jme.2016.502
3. Perelot, T., Kriuchkov, A., & Kravets, V. (2010). Justification of the Method of Gas Suppression and Neutralization of Toxic Gases during Mass Explosions in Quarries. *Herald of the National Technical University of Ukraine «Kyiv Polytechnic Institute», Series of «Mining»*, *19*, 178–181.
4. Berezhetskyi, A., & Vovk, O. (2004). The Use of Steaming Solutions to Reduce Dust and Gas Emissions in Mass Explosions. *Herald of the National Technical University of Ukraine «Kyiv Polytechnic Institute», Series of «Mining»*, *11*, 72–78.
5. Kravets, V., Tkachuk, K., & Han, A. (2009). Increasing the Safety and Efficacy of Blasting Operations Using Special Designs Borehole Charges. *Herald of the National Technical University of Ukraine «Kyiv Polytechnic Institute», Series of «Mining»*, *18*, 53–57.

6. Yurchenko, A. (2010). Reducing Emissions from Mass Explosions in Quarries by Using a Rubber Plug with an Anchor Device as a Stemming of Downhole Charges. *Collection of Research Papers of the National Mining University, 35* (2), 111–117.
7. Komir, V., Blinkov, V., Romashko, A., & Sokurenko, V. (2007). Impact of Stemming Design on the Crushing Intensity of Rock Models. *KSPU Bulletin*, *42* (1), 90–92.
8. Vorobiov, V. (2000). The Effectiveness of the Use of Rational Design Taps Hole Charges. *Herald of the National Technical University of Ukraine «Kyiv Polytechnic Institute», Series of «Mining»*, *2*, 51–53.
9. Saharan, M., Sazid, M., & Singh, T. (2017). Explosive Energy Utilization Enhancement with Air-Decking and Stemming Plug, 'SPARSH'. *Procedia Engineering*, *191*, 1211 – 1217. doi: 10.1016/j.proeng.2017.05.297
10. Shevkun, E., & Leschinsky, A. (2006). Downhole Charges with Shortened Stemming. *Mining Informational and Analytical Bulletin*, *4*, 139–146.
11. Choudhary, B., & Arora, R. (2017). Screened Drill Cuttings in Blasthole for Tamping of Stemming to Reduce Generation of Fly Rock. *Journal of Mines, Metals and Fuels*, *65* (1), 19–23.
12. Zhang, Z. (2016). *Rock fracture and blasting: Theory and applications.* Butterworth-Heinenmann Elsevier. doi: 10.13140/RG.2.1.1498.2481
13. Rehman, A. (2016). *Design and development of stemming plug to enhance blast performance.* Lahore, Pakistan: University of Engineering and Technology. doi: 10.13140/RG.2.2.15991.47523
14. Armstrong, L. (1994). *The quality of stemming in assessing blasting efficiency.* Sydney, Australia: The University of New South Wales.
15. Cevizci, H. (2012). A Newly Developed Plaster Stemming Method for Blasting. *Journal of the Southern African Institute of Mining and Metallurgy*, *112* (12), 1071–1078.
16. Morera de la Vall González, G. (2018). *Dust production in mining. Suppression measures in quarry blasting.* Madrid, Spain: The Technical University of Madrid (UPM).
17. Katanov, I., Kondratyev, S., & Sysoyev, A. (2019). Increasing Safety at Rock Preparation by Blasting in Open Pits. *E3S Web of Conferences*, *134*. Available at https://www.e3s-conferences.org/articles/e3sconf/pdf/2019/60/e3sconf_sdemr18_01017.pdf
18. Vorobiov, V., Zakharov, V., Berezhetskyi, A., Yefremov, E., & Barannyk, V. (2003). Reducing Dust And Gas Emission During Mass Explosion in Quarries. *Herald of the National Technical University of Ukraine «Kyiv Polytechnic Institute», Series of «Mining»*, *8*, 163–169.
19. Tyschuk, V. (2010). Studies of Specific Dust and Gas Emissions during Mass Explosions in Open Pits and Methods for Reducing Harmful Emissions. *The collection "Up-to-Date Resource- and Energy-Saving Technologies in Mining Industry"*, *1* (5), 127–132.
20. Vozgrin, R., Mironov, Yu., & Moldovan, D. (2013). To the Question of the Properties of the Material for the Manufacture of Borehole and Drill Stemming. *Problems of Geology and Subsurface Development*, 11 (2), 304–305.
21. Katanov, I., & Skachilov, P. (2015). Improving the Design of Borehole Charge with Foam-Gel Tamping. *Bulletin of the Kuzbass State Technical University*, *5*, 43–46.
22. Shevkun, E., Leschinsky, A., Galimjanov, A., & Rudnitsky, K. (2014). Production Tests of Combined Shothole Stemming. *Mining Informational and Analytical Bulletin*, *4*, 97–107.
23. Leschinsky, A. (2014). Design Development Stemming Blast Holes. *Electronic scientific journal "Scientists Notes PNU"*, *5* (2), 66–71. Available at http://pnu.edu.ru/media/ejournal/articles-2014/TGU_5_57.pdf
24. Shevkun, E., Leschinsky, A., & Galimjanov, A. (2015). Short Combined Stopper Explosive Chinks of High Locking Ability. *Mining Informational and Analytical Bulletin*, *4*, 331–336.
25. Leschinsky, A., & Shevkun, E. (2008). *Clogging blast holes in quarries.* Khabarovsk: Pacific National University.

26. Gurin, A., Ermak, L., & Teterya, O. (2008). Analytical Researches of Influence of Auxiliary Materials of Punches of Explosives in Wells on Change of Parameters of Chemical Reactions of Explosion and Structure of Products of Explosion. *Labor and Environmental Protection at the Enterprises of the Mining and Metallurgical Complex*, *10*, 196–200.
27. Tverda, O., & Vorobiov, V. (2012). Justification of the Selection Criterion of a Safe and Effective Type of Explosive during Mass Explosions in Open Pits. *Collection of scientific works "Occupational Health and Safety Issues in Ukraine"*, *22*, 56–64.
28. Tverda, O., & Plyatsuk, L. (2018). The Design of Borehole Plug with a Two-Stage Absorbing System for Harmful Gases. *The collection "Up-to-Date Resource- and Energy-Saving Technologies in Mining Industry"*, *1* (21), 103–115.
29. Zvyagintseva, A., & Zavyalova, A. (2015). Analysis of the Basic Technological and Engineering Measures Aimed at Reducing Dust and Gas Emissions Mass Explosion at the Quarry Mining and Processing Plant. *Heliogeophysical Research*. Available at http://vestnik.geospace.ru/index.php?id=285
30. Prymyska, S., Beznosyk, Yu., Statyukha, G., & Reshetilowski, W. (2010). Prospects for Purification of Thermal Energy Exhaust Gases on Synthetic Zeolites. *Bulletin of NTU "KhPI"*, *10*, 70–77.
31. Tverda, O., Plyatsuk, L., Repin, M., & Tkachuk, K. (2018). Controlling the Process of Explosive Destruction of Rocks in Order to Minimize Dust Formation and Improve Quality of Rock Mass. *Eastern-European Journal of Enterprise Technologies*, *3* (10), 35–42. doi: 10.15587/1729-4061.2018.133743

sciendo

LATVIAN JOURNAL OF PHYSICS
AND TECHNICAL SCIENCES
2021, N 4

DOI: 10.2478/lpts-2021-0031

# FRACTOGRAPHIC STUDY OF MARINE DIESEL ENGINE CONNECTING ROD STUD BOLT CRACK

K. Carjova*, V. Priednieks, R. Klaucans, I. Irbe, A. Urbahs

Latvian Maritime Academy,
12 k-1 Flotes Str., Riga, LV-1016, LATVIA
*e-mail: kristine.carjova@latja.lv

Failures of marine diesel engine components can lead to serious consequences for a vessel, cargo and the people on board a ship. These consequences can be financial losses, delay in delivery time or a threat to safety of the people on board. This is why it is necessary to learn about connecting rod bolt failures in order to prevent worst-case scenarios.

This paper aims at determining the origin, velocity and the duration of fatigue crack development of a diesel alternator engine which suffered a significant failure of one of its mains, not long after a major overhaul had been completed and with less than 1000 running hours having elapsed.

It was verified with fatigue rupture of one of the four connecting rod stud bolts. Tensile tests were performed in the remaining connecting rod bolts. During this procedure, another fatigue crack in an adjacent bolt was identified. The probable root case of damage, and at the end some final remarks are presented.

***Keywords:*** *Acoustic emission, connecting rod, crack, diagnostics, fatigue crack growth rate, fractography, fatigue test, marine diesel engine failure.*

## 1. INTRODUCTION

The power generated by the piston in the combustion chamber of marine engine is transferred to the crankshaft using the connecting rod. While transferring this tremendous power, the connecting rod itself is subject to different stresses, which make is vulnerable to damage. For this reason, the connecting rod bolts are used to join the connecting rod and con-rod bearing cover under the tremendous stresses

generated by the running engine.

The most common type of connecting rod that is used in the ship auxiliary engine is oblique or crosscut connecting rod, which is made of two parts.

The connecting rod of the engine must be inspected at regular intervals of time to ensure there is no defect or problem to avoid any future accidents/emergency [1], [2].

The studies of how bolting assemblies are influenced by fatigue are presented below. In engineering, bolted connections are employed in a very large number of structural members. These connections may look simple on the surface level, but are complex assembles with varying geometric and fatigue properties, which need to be properly accounted for in order to provide a clear picture of their useful life in service. An introduction into fatigue and methods by which fatigue strength can be quantified are examined in the present paper.

The aim of the research is to examine the fatigue and crack propagation of the rod bolt or to find the effect of other destructive forces that cause the engine to collapse.

## 2. CASE STUDY

Significant damage of ships machinery, which happened not long after major overhaul had been completed and with less than 1000 running hours having elapsed, resulted in financial loss and insurance attention. In order to restore the engine and the vessel back to full operating capacity, replacement of the complete engine frame as well as a new crankshaft, along with other major components were required.

Study of diesel engine stud bolt resulted in fatigue crack after 39596 cycles of the bench operating time in resource test program were reached. Loading modes were determined according to the engine rotation speed.

The basic causes of failure were due to the fact that tensioning procedures and elongation checks for hydraulic bolts were not properly followed and re-tensioning checks were not done according to manufacturer instruction manual or with reference to engine technical service letters.

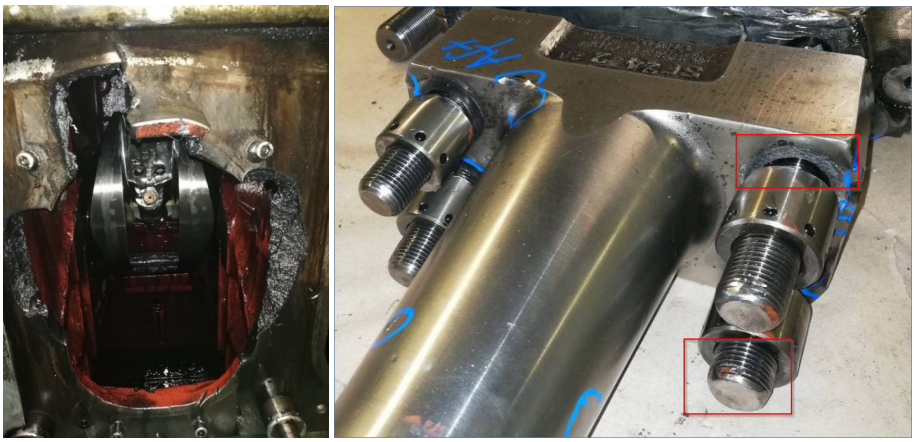

*Fig. 1 & 2*. Damaged engine frame and connecting rod.

## 3. MATERIALS AND METHODS

Two of the fractured bolts and bolts from the remaining connecting rods were selected for laboratory analysis. The analyses consisted of low magnification and scanning electronic microscopy (by scanning with a SEM HITACHI-S300 N scanning electron microscope) observation of the fracture surface, hardness, tensile tests and metallographic characterisation. Hardness was performed over the flat shank of some selected bolts using the Rockwell C scale (HRC). Tensile tests were performed with MTS 810 (MTS Corporation, Eden Prairie, MN). Metallographic analyses were done in two selected bolts: one broken during the failure, other during the tensile test.

## 4. DEFECT MECHANISM AND MATHEMATICAL MODEL DESIGNATIONS

Fatigue can be defined as a process of damage accumulated during each cycle of the dynamic load that the structure is subjected to with an important characteristic of load intensity lower than the values that would cause immediate failure [3]. Fatigue cracks start and evolve in two phases – formation (usually starting on the material surface) of a shear crack on crystallographic slip planes in the first phase, and growth of the crack in a direction normal to the applied stress in the second phase [4]. Cui proposed a division of the failure fatigue process in five stages, namely, crack nucleation, microstructurally small crack propagation, physically small crack propagation, long crack propagation and final fracture [5].

Many crack propagation equations have been proposed over the years to improve prediction accuracy and incorporate a variety of effects. The general form of these crack propagation equations may be expressed as:

$$\frac{dL}{dN} = f(\Delta\sigma, L \cdot c_i), \quad (1)$$

where, the crack length is denoted by L, mm, which is measured from the source of fatigue failure in the selected direction of propagation of the crack perpendicular to its front. The number of cycles of load applied is given by N, loading cycles: bench operating hours (in the calculations the operating time of the last day of testing is used); $\Delta\sigma$ is the stress range and $c_i$ – the material parameters.

Designations that are used further in the paper:

$V_L$, μ / cycle l – the crack growth rate, which is measured in increment of crack length per loading cycle.

h, nm / cycle – the fatigue damage mesoline pitch in one cycle.

$\Delta N_{CRi}$, loading cycles – the number of loading cycles during which the crack grew from the minimum analysed size to the current value of its length, at which the rate of crack growth $V_L$ was measured by the size of mesoline pitch h, μ (nm) (in the calculations, the bench operating time was used last day of testing).

$N_{CR}$, loading cycles – the number of loading cycles during which the crack grew from the minimum size to the current value of its length, at which the crack growth rate $V_{Li}$ , nm / cycle (μ / cycle) was measured by the mesoline pitch (in calculations, the operating time of the last test day is used).

Crack growth equations of the form are not a true differential equation, as they do not model the process of crack growth in a continuous manner throughout the loading cycle. Separate cycle counting or identification algorithms, such as the commonly used rain flow-counting algorithm, are required to identify the maximum and minimum values in a cycle. Although developed for the stress/strain-life methods, rain flow counting has also been shown to work for crack growth [6].

## 5. FRACTOGRAPHIC STUDY RESULTS

A fractographic study of fracture of stud bolt was carried out. A general view of the fracture of the bolt is shown in Fig. 3.

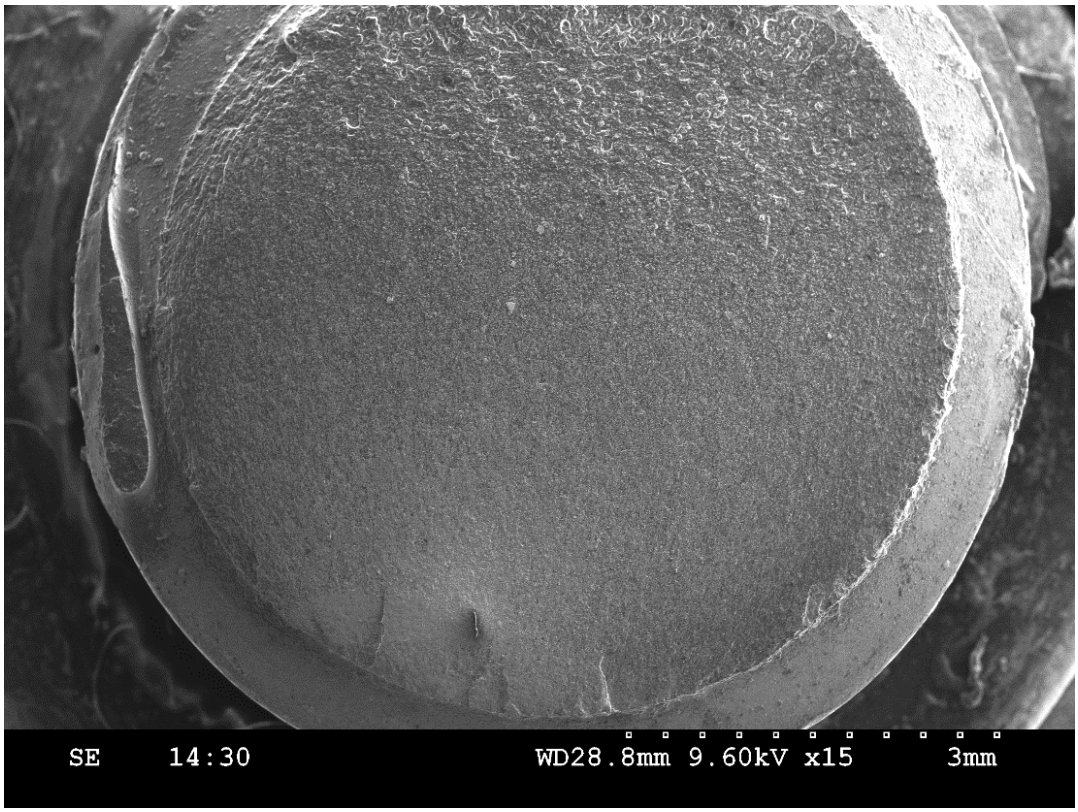


*Fig. 3.* General view of the crack of the bolt.

According to the performed fractographic analysis, it was found that the propagation of cracks in the stud bolt material was characterised by the formation of fatigue damage mesolines. The distance between fatigue damage mesolines generally increases, which characterises an increase in the crack growth rate as its length increases (the area of fatigue damage).

Destruction is multi-focal (Figs. 3–6).

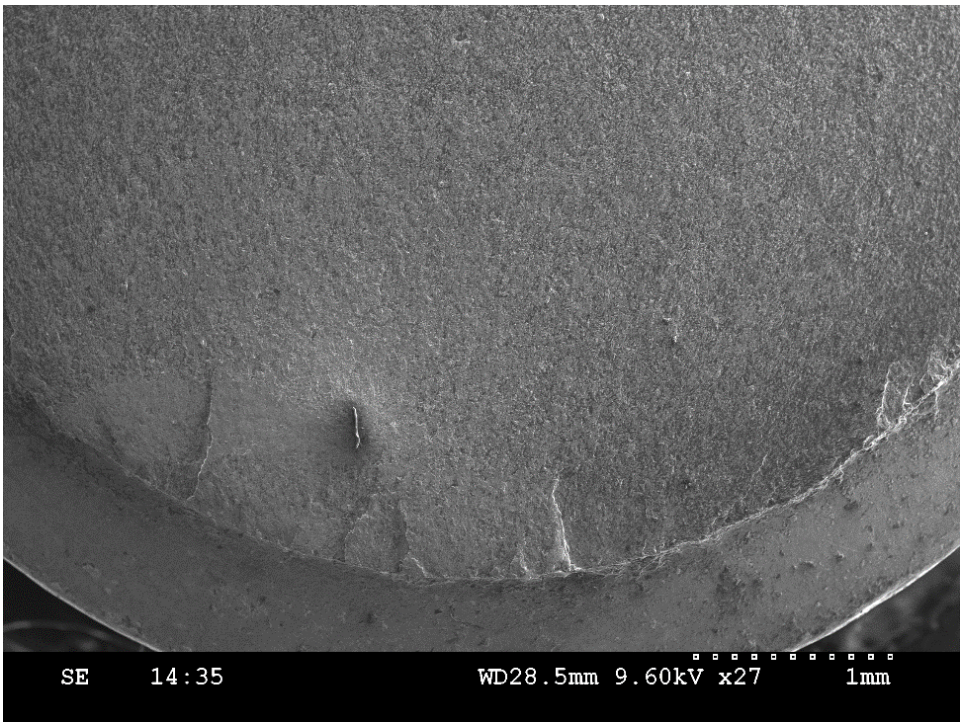


*Fig. 4.* Focal zone of the bolt.

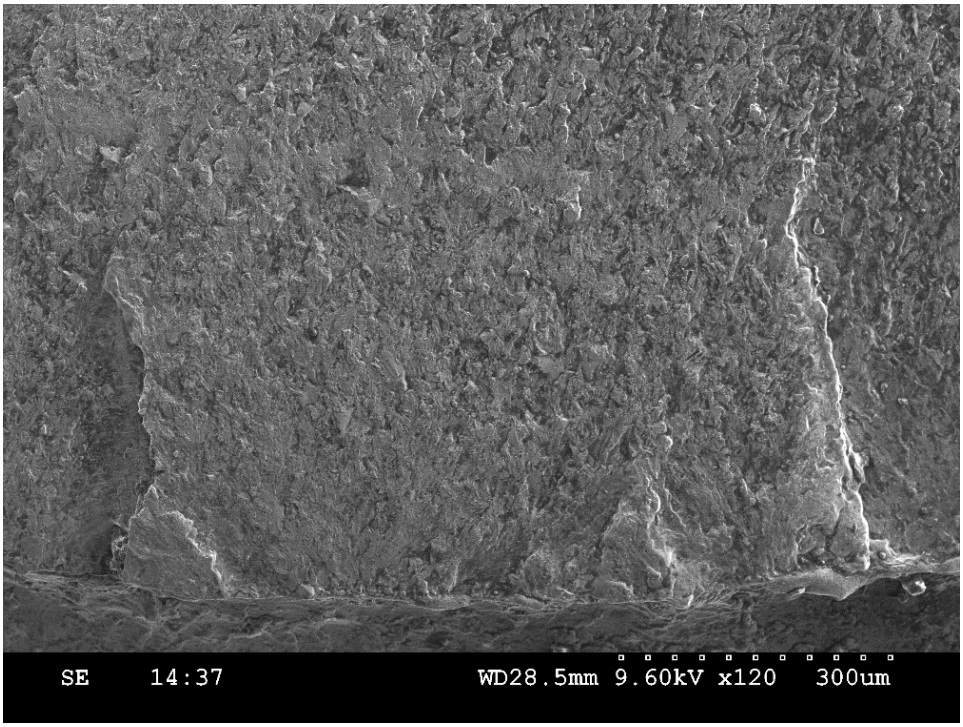


*Fig. 5.* Focal zone of the bolt.

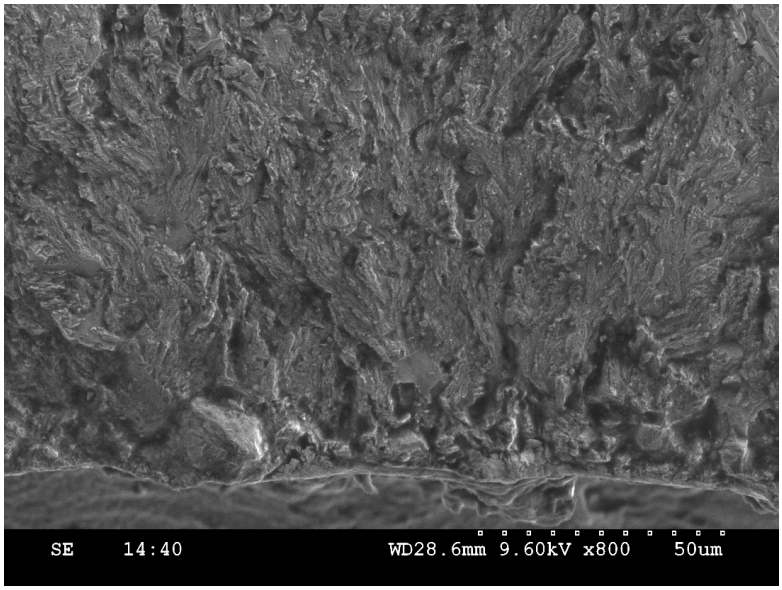


*Fig. 6.* The main nucleaus of the bolt.

Estimation of the length of a crack in a fracture of a bolt, respectively $L_1$ (the distance from the origin of the source to the current position of the front crack propagation, μ m ), and the speed of its propagation $V_{L1}$ ( μ / cycle ) was performed with respect to micro cracks nucleated from the main nucleus (hereinafter in the notation $L_i$, the index i corresponds to the crack number).

The microfractograms of the surface of the fracture fatigue zone, obtained by scanning with a SEM HITACHI-S300 N scanning electron microscope at different distances from the focus of the fatigue fracture, are shown in Figs. 7–19 for the main crack No. 1 with its length of 0.04 mm to achieve the length of 3.5 mm.

In the structure of crack fracture fatigue damage mesolines are observed reflecting the kinetics of fatigue crack propagation at regular loading of object bench tests. The mesoline pitch is associated with the propagation velocity of the fatigue crack in the bolt material as a change in the position of its front by the value of this step in one loading cycle.

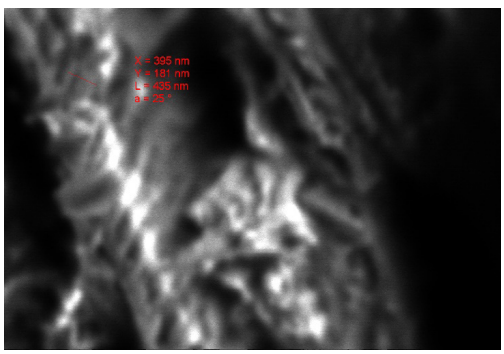


*Fig. 7.* Electronic microfractogram of crack No. 1, crack length $L_1$ = 0.04 mm, average mesoline pitch h = 145 nm / cycle.

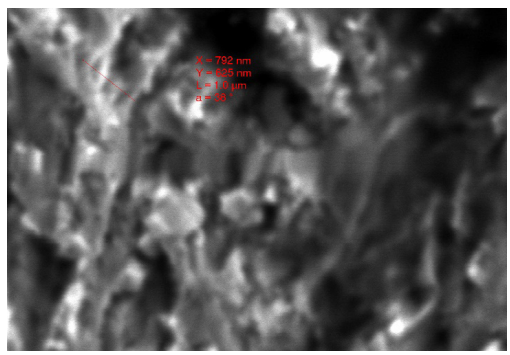


*Fig. 8.* Electronic microfractogram of crack No. 1; crack length $L_1$ = 0.08 mm, average mesoline pitch h = 250 nm / cycle.

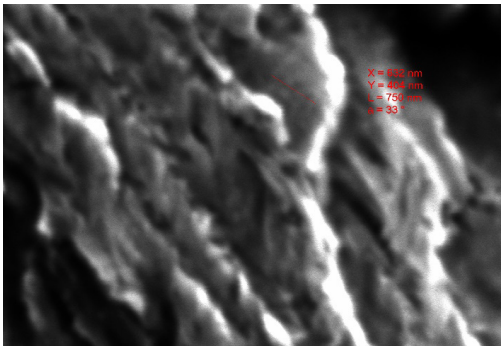

*Fig. 9.* Electronic microfractogram of crack No. 1; crack length $L_1$ = 0.27 mm, mesoline pitch h = 188 nm / cycle.

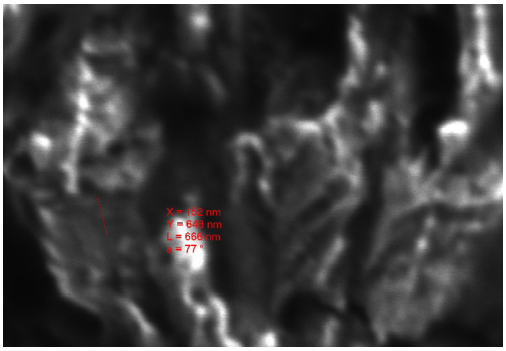

*Fig. 10.* Electronic microfractogram of crack No. 1; crack length $L_1$ = 0.33 mm, average mesoline pitch h = 222 nm / cycle.

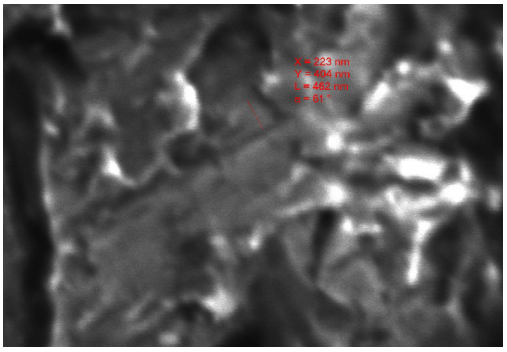

*Fig. 11.* Electronic microfractogram of crack No. 1; crack length $L_1$ = 0.60 mm, average mesoline pitch h = 155 nm / cycle.

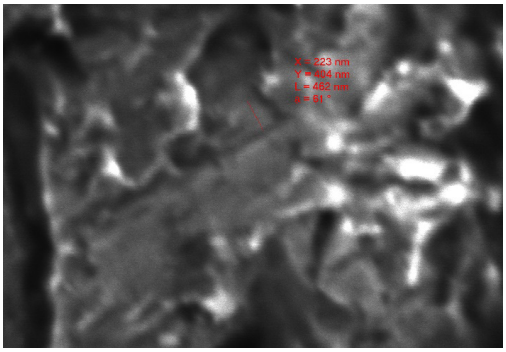

*Fig. 12.* Electronic microfractogram of crack No. 1; crack length $L_1$ = 0.65 mm, average mesoline pitch h = 188 nm / cycle.

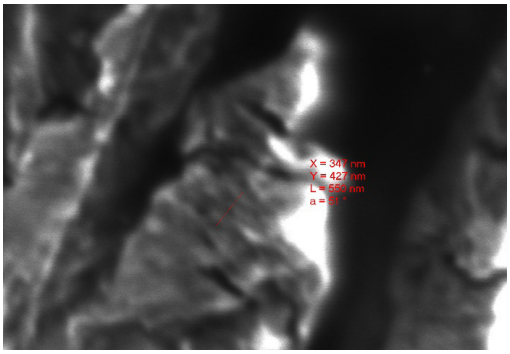

*Fig. 13.* Electronic microfractogram of crack No. 1; crack length $L_1$ = 0.95 mm, average mesoline pitch h = 185 nm / cycle.

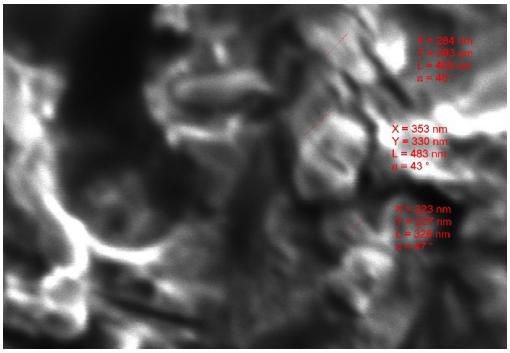


*Fig. 14.* Electronic microfractogram of crack No. 1; crack length $L_1$ = 1.40 mm, average mesoline pitch h = 153 nm / cycle.

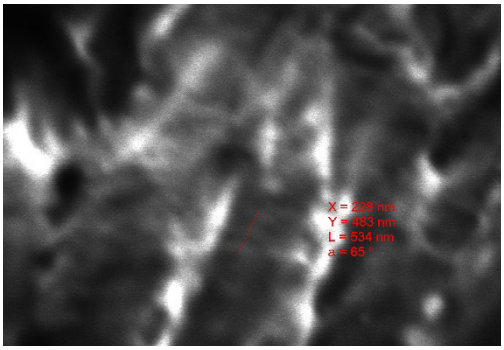


*Fig. 15.* Electronic microfractogram of crack No. 1; crack length $L_1$ = 1.44 mm, average mesoline pitch h = 178 nm / cycle.

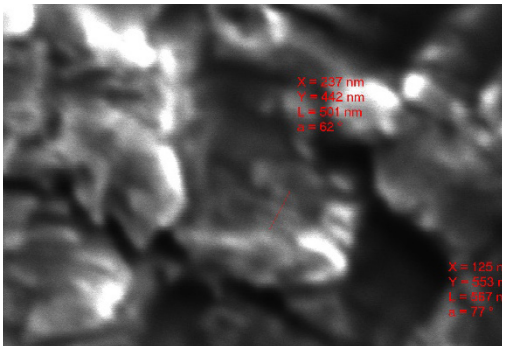


*Fig. 16.* Electronic microfractogram of crack No. 1; crack length $L_1$ = 2.00 mm, average mesoline pitch h = 178 nm / cycle.

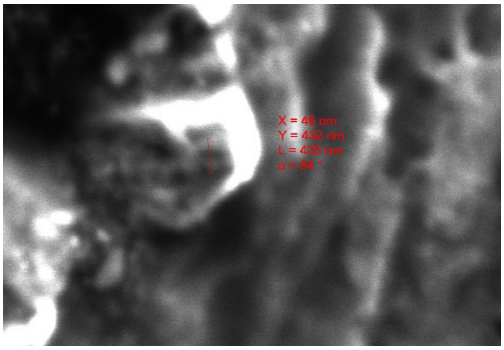

*Fig. 17.* Electronic microfractogram of crack No. 1 ; crack length $L_1$ = 2.50 mm, average mesoline pitch h = 218 nm / cycle.

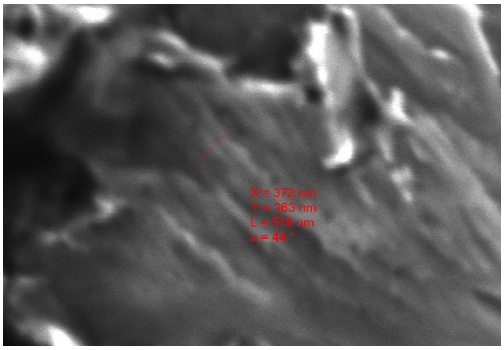


*Fig. 18.* Electronic microfractogram of crack No. 1; crack length $L_1$ = 3 .00 mm, average mesoline pitch h = 173 nm / cycle.

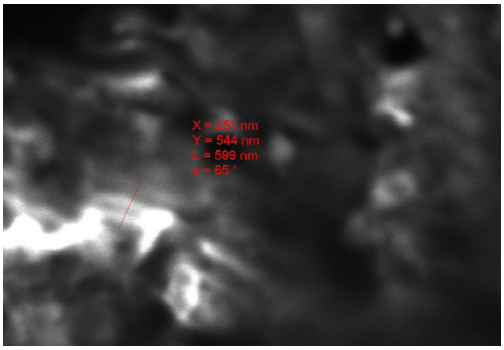


*Fig. 19.* Electronic microfractogram of crack No. 1; crack length $L_1$ = 3.50 mm, average mesoline pitch h = 200 nm / cycle.

The results of measurements of the length of the fatigue crack in the fracture of the stud bolt, the mesoline pitch as they develop from the fracture centre to the length $L_1$, respectively, as well as the calculation results of additional parameters are presented in Table 1.

**Table 1.** The Results of Fractographic Assessment of the Velocity $V_{L1}$ and the Growth Period of Fatigue Crack No. 1

| No. | $L_1$, mm | $V_{L1}$, μ/cycle | $1/V_{L1}$ cycle/μ | $\Delta N_i$, cycle | $N_{CRi}$, cycle | $N_1$, cycle |
|---|---|---|---|---|---|---|
| 1 | 0.04 | 0.145 | 6.897 | 276 | 276 | 15353 |
| 2 | 0.08 | 0.250 | 4.000 | 160 | 436 | 15513 |
| 3 | 0.27 | 0.188 | 5.333 | 1013 | 1449 | 16526 |
| 4 | 0.33 | 0.222 | 4.505 | 270 | 1719 | 16797 |
| 5 | 0.60 | 0.155 | 6.452 | 1742 | 3461 | 18539 |
| 6 | 0.65 | 0.128 | 7.813 | 391 | 3852 | 18929 |
| 7 | 0.95 | 0.185 | 5.405 | 1622 | 5474 | 20551 |
| 8 | 1.40 | 0.153 | 6.536 | 2941 | 8415 | 23492 |
| 9 | 1.44 | 0.178 | 5.618 | 225 | 8640 | 23717 |
| 10 | 2.00 | 0.178 | 5.618 | 3146 | 11786 | 26863 |
| 11 | 2.50 | 0.218 | 4.598 | 2299 | 14084 | 29162 |
| 12 | 3.00 | 0.173 | 5.780 | 2890 | 16975 | 32052 |
| 13 | 3.50 | 0.200 | 5.008 | 2504 | 19479 | 34556 |

Plotting crack growth diagrams and determining their growth rate on the polished surface of the sample, the moment when a crack appeared was clearly visible with a microscope. During the tests, after a certain number of loading cycles, the crack size $L_1$ was measured on the front surface of the specimen.

The results of such measurements were used to construct the crack growth diagrams in the $V_L$; L axes, i.e., dependence of the crack length on the crack growth rate, measured in increment of crack length per loading cycle. The rate of growth of fatigue cracks was determined by graphical differentiation of these diagrams. The most convenient is the scheme for determining the rate of crack growth using a graphical editor (Fig. 20).

In the calculation of fatigue crack growth rate $V_{L1}$ by the number of mesolines and the mesoline pitch where crack No. 1 had reached length of $L_1$ = 0.04 mm, mesoline pitch was assumed with reference to the average pitch, recorded in its length, which corresponds to $L_1$ = 0.04 mm (see Table 1).

Graphs of kinetic dependences $V_L$ = f (L) and crack growth curves L = f (N) (N is the current operating time during bench tests) are shown in Figs. 20 and 21.

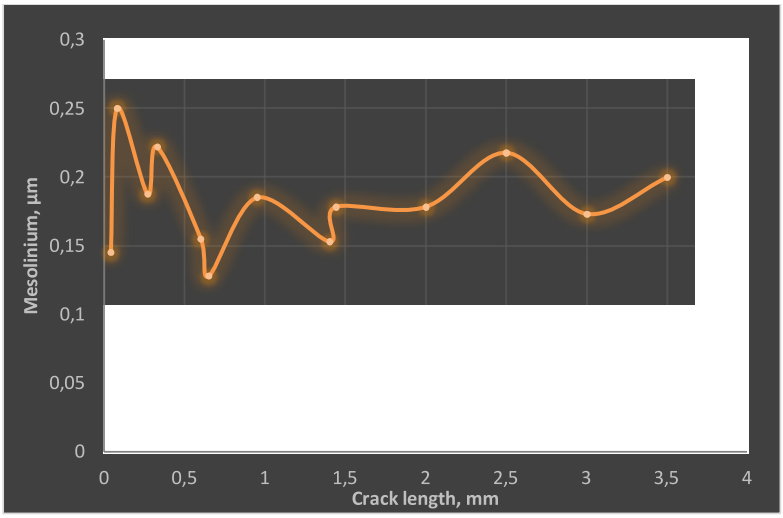


*Fig. 20.* Crack growth rate $V_{L1}$ of its length $L_1$, respectively.

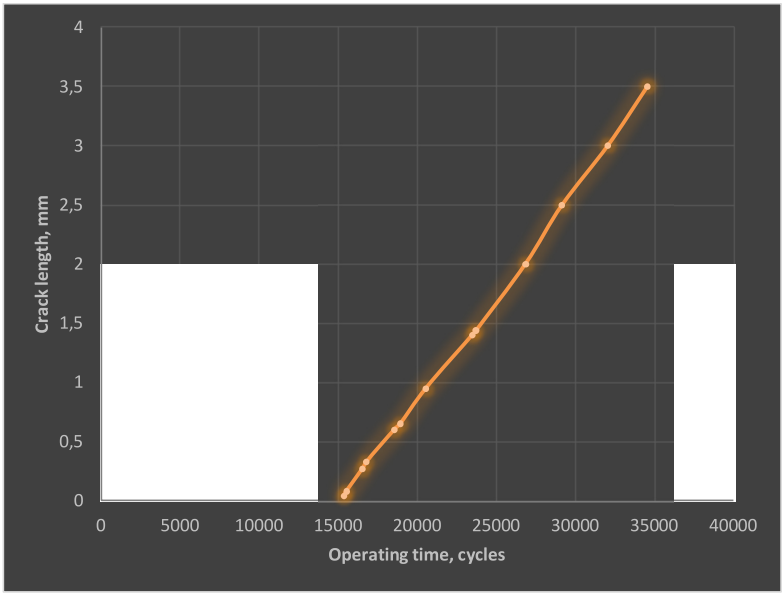


*Fig. 21.* The dependence of the length of the fatigue crack $L_1$ on the current operating time during testing.

The presented study was based on the methodical approach given in sources [7]-[9]. It should also be noted that the above estimate of the crack growth period is based on measurements of local velocities having a stochastic nature; therefore, the accuracy of the estimation of the crack growth period depends on the frequency of velocity measurements [10]. Taking into account the number of measurements performed in this study, the error in estimating the crack growth period with a probability of 90 % does not exceed ± 12 %.

In this way, fatigue crack in the material

of the bolt length of 0 and 0.4 mm with a probability of 90 % was formed with an operating time of 15353 ± 2337 loading cycles.

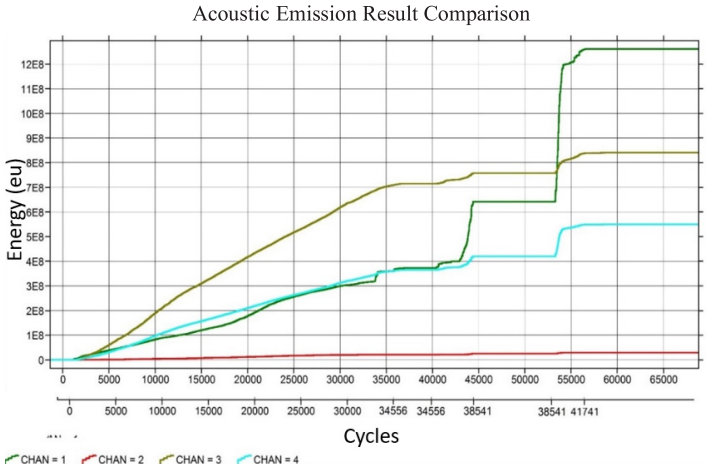


*Fig. 22.* The total energy of the acoustic emission signal on the last day of testing (lower scale – reduced loading cycles).

## 6. DISCUSSION

In order to cope with vessel equipment reliability, engineering designers rely heavily on the regulations prescribed by the classification societies. Classification societies' rules are based on a wide knowledge collected over hundreds of years and are mostly based on simplified, empirical equations. However, not all the problems occurring on modern ships can be successfully solved using this approach. To properly address issues of marine structural failures, engineers need to turn to failure analysis databases and, learning from the findings, improve procedures for ship designing.

Reviewing case studies, one can notice that most of them use solely experimental approaches in finding the causes of failures. Techniques such as NDT inspection, microscopy or crystallography are used to determine the origin of failures. Only a few studies use numerical analysis as a supplement to traditional experimental techniques applied in the field of failure analysis.

However, those who do combine experimental and numerical approaches tend to present more reliable results and go a bit further than usual failure analysis does – they suggest modifications to engineering design. Thus, a combination of failure analysis and design optimization is arising here.

The following points must be considered when checking the connecting rod stud bolt for re-use or replacement. If problems enlisted below are not acknowledged at the first opportunity, they may increase the risk of crack development of connecting rod bolts [11].

**Problem requiring design optimization** (Not objective of the research) **No. 1.** In some cases, during inspections, a small gap between the connecting rod bolt head and the connecting rod itself is identified in the assembled condition with fully tightened connecting rod bolts.

On some affected connecting rods, a

feeler gauge with up to 0.4 mm thickness could be introduced between bolt head and connecting rod (see Fig. 23) [12].

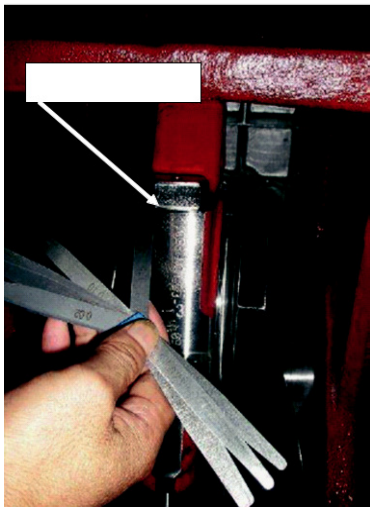

*Fig. 23.* Introduction of feeler gauge between connecting rod bolt head and connecting rod.

For correct loading of the connecting rod bolt, no gap is admissible. After correct assembly and tightening of the bolt, the connecting rod bolt has to rest without any gap on the connecting rod.

The investigation of the above cases has revealed that the chamfer of the connecting rod bolt bore was not machined properly so that the bolt was partly resting on the chamfer instead of the proper contact area under the bolt head (see Figs. 24 and 25).

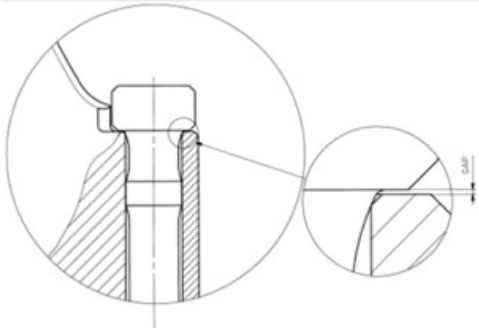

*Fig. 24*. Improper seat of the bolt on mismachined chamfer.

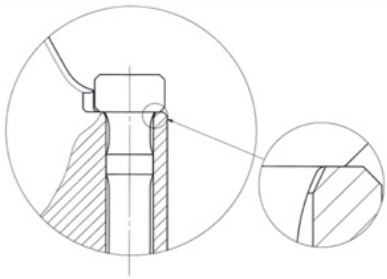

*Fig. 25.* Proper seat of the bolt on the contact surface under the bolt head.

In a worst-case scenario, such a gap between connecting rod bolt and connecting rod may lead to a plastic deformation (adaption) between bolt radius and mismachined chamfer during engine operation. This, with a certain setting of the bolt, may cause a partial loss of pretensioning of the connecting rod bolt.

Impact on engine: Unfortunately, based on the information available, it could not be excluded that GenSets are affected in a way that some connecting rods may show such a mismachined chamfer.

Measures recommended by MAN Diesel: Fortunately, the inspection procedure is very easy and this inspection should be accomplished according to MAN Service Letter SL08-500/JNN.

**Problem requiring design optimization** (Not objective of the research) **No. 2.** Elongation of hydraulically tightened bolts. The elongation measurement is introduced to reduce possible failures in connection with hydraulic tightening of bolts such as:

- Insufficient hydraulic pressure;
- Missing pressure at one or more hydraulic jacks due to incorrect fixing of hydraulic snap coupling at the hose connection[13].

With the introduction of elongation measurement, the elongation of each bolt is monitored during the tightening process and hereby it is possible to determine if the correct hydraulic pressure has been applied to each bolt.

The tightening procedure with elongation measurement is performed according to MAN Service Letter SL2018-656/JNN.

By introducing the elongation measurement, the retightening procedure is changed after overhaul as follows:

- Without elongation measurement: Retightening after 200 running hours.
- With elongation measurement: Retightening after starting up the engine, but before any load has been applied.

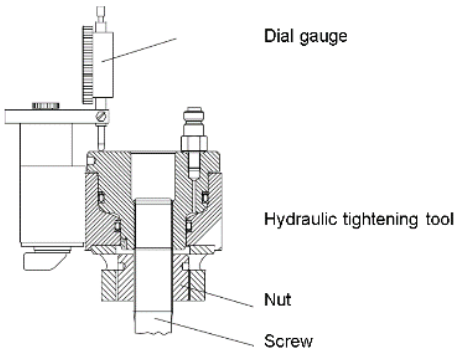


*Fig. 26*. Measuring tool, 1 pc hydraulic jack will be needed.

**Problem requiring design optimization** (Not objective of the research) **No. 3.** Fretting on connecting rod contact surface (see Fig. 23).

Depending on the engine type, the connecting rod itself consists of three different main parts which are tightened together with bolts. Due to operating forces, those connections as well as the part itself, are subjected to high load. Every connection fulfils high requirements towards mechanical load. Micro-movements between two parts under high load can in single cases lead to fretting marks. If those fretting marks are not grinded and smoothened at the first opportunity, they may increase the risk of crack development. To avoid a damage caused by fretting marks, we released precautions and countermeasures [14].

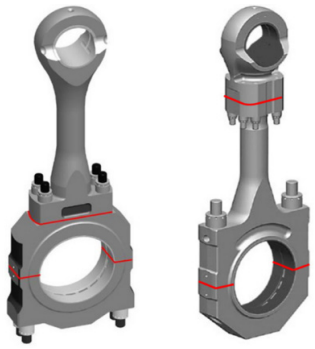

*Fig. 27.* Connecting rod contact surface.

Measures: To prevent dynamically loaded contact surfaces from fretting, certain preconditions have to be fulfilled. Every unevenness or deviation from the flat machined surface has to be precisely eliminated. Afterwards, during assembling, the surface has to be clean, dry and absolutely free of oil, grease or other fluids. To ensure a proper condition of each connecting rod part and a high operating reliability, all contact surfaces have to be checked and, if necessary, grinded and magnetically crack tested.

*Fig. 28*. Fretting on a connection surface.

## 7. CONCLUSION

In this paper, recent ship engine incident has been outlined to learn about connecting rod bolt failure nature. Unfortunately, this study is not able to affect the industry, and similar failures are still observed.

The research successfully proved that there were clear signs of fatigue and no other destructive forces that could cause the engine to collapse.

The study allowed concluding that a fracture in the material of bolt No. 7 in the diesel engine connecting rod stud is fatigue and the destruction is multi-focal.

The results of fractographic studies made it possible to determine the moments of nucleation of cracks in the fractures of the bolt material: a fatigue crack in the material of a bolt with a length of 0.04 mm with a probability of 90 % was formed with a bench operating time of 15353 ± 2337 loading cycles.

Particularly, to avoid future failures, the design optimization can be considered as a solution as described in the discussion paragraph.

It is strongly recommended as good engineering practice to replace diesel engine connecting rod stud bolt in every main overhaul due to possibility of bolt fatigue crack development during next service period and, as a result, expensive breakdown may occur.

## ACKNOWLEDGEMENTS

The research has been supported by the Latvian Science Council. Project "Development of Smart Technologies for Efficient and Reliable Waterborne Operations". (STEEWO) (No. LZP-2019/1-0478).

## REFERENCES

1. Gasparjans, A., Terebkovs, A., & Ziravecka, A. (2017). Application of resonance method for examining of piston ring technical condition. In *16th International Scientific Conference* (pp. 884–891), 24–26 May 2017, Jelgava, Latvia (Elsevier SCOPUS, Thomson Reuters Web of Science, AGRIS, EBSCO Academic Search Complete, Agricola).
2. Gasparjans, A., Terebkovs, A., & Ziravecka, A. (2019). Theoretical and experimental analysis of technical condition of piston rings of vessel diesel installations by method of resonance oscillations. In *18th International Scientific Conference* (pp. 1287–1294), 22–24 May 2019, Latvia University of Agriculture Faculty of Rural Engineering, Jelgava, Latvia. doi: 10.22616/ERDev2019.18.
3. Pastorcic, D., Vukelic, G., & Bozic, Z. (2019). Coil Spring Failure and Fatigue Analysis. *Eng. Fail. Anal.*, *1* (99), 310–318.
4. Lukacs, J. (2019). Fatigue Crack Propagation Limit Curves for High Strength Steels Based on Two-Stage Relationship. *Engineering Failure Analysis*, 431–442.
5. Cui, W. A (2002). State-of-the-Art Review on Fatigue Life Prediction Methods for Metal Structures. *Journal of Marine Science and Technology*, *7* (1), 43–56.
6. Schijve, J. (1979). Four Lectures on Fatigue Crack Growth. *Engineering Fracture Mechanics*, 169–181. doi:10.1016/0013-7944(79)90039-0. ISSN 0013-7944.

7. Shaniavsky, A. A. (2003). *Safe fatigue failure of aircraft structural elements*. Ufa: Publishing house of scientific and technical literature “Monograph”.
8. Stoyda, Yu.M. (1988). *The Development of the Method of Quantitative Fractography and the Study of Cyclic Crack Resistance of Structural Elements from Aluminium Alloys*. The Doctoral Thesis. Moscow: VIAM.
9. Guide for Designers (RDK). (1980). Aircraft Strength (vol. 3), Fatigue Strength, Resource and Reliability of an Aircraft (book 4), Determination by the Method of Fractography of the Growth Duration of Fatigue Cracks in the Structural Elements of an Airframe (issue 12). M. Ed. Department of TsAGI.
10. Urbahs, A., & Carjova, K. (2018) Research on the Bolting Elements of Helicopter Fuselage and Tail Boom Joints Using Acoustic Emission Amplitude and Absolute Energy Criterion. *American Journal of Aerospace Engineering, 32* (3). https://doi.org/10.1061/(ASCE)AS.1943-5525.0000963
11. Vizentin, G. (n.d.). *Marine Propulsion System Failures – A Review*. Available at https://www.mdpi.com/2077-1312/8/9/662/htm
12. MAN Service Letter SL08-500/JNN, MAN Diesel
13. MAN Service Letter SL2018-656/JNN, MAN Diesel
14. MAN Diesel & Turbo. (2015). *PrimeServ Customer Information No. 348 / June 2015*. Available at https://primeserv.man-es.com/docs/librariesprovider5/service-letter-marine/pci-348.pdf?sfvrsn=1cdb3fa2_4

sciendo

LATVIAN JOURNAL OF PHYSICS
AND TECHNICAL SCIENCES
2021, N 4

DOI: 10.2478/lpts-2021-0032

# DEVELOPMENT OF METHODOLOGY FOR CHARACTERIZATION OF SURFACE ROUGHNESS OF SOLID METALLIC SURFACES USING OIL SLIPPAGE METHOD

I. O. Ohijeagbon[1], A. A. Adeleke[2*], P. P. Ikubanni[2], T. A. Orhadahwe[3], G. E. Adebayo[1], A. S. Adekunle[1], A. O. Omotosho[4]

[1]Department of Mechanical Engineering,
University of Ilorin, Ilorin, NIGERIA.
[2]Department of Mechanical Engineering,
Landmark University, Omu-Aran, NIGERIA
[3]Department of Mechanical Engineering,
University of Ibadan, Ibadan, NIGERIA
[4]Department of Mechanical Engineering,
Covenant University, Ota, NIGERIA
*e-mail: adeleke.kunle@ymail.com

The study employed the phenomenon of friction between liquid droplets and solid metallic surfaces in surface roughness analysis of engineering materials. Five samples of mild steel plate were prepared to different degrees of surface roughness by facing operation. The sample surfaces were analysed to determine the roughness parameters (mean roughness, root mean square roughness, roughness skewness, and roughness kurtosis) and friction coefficient of the surfaces. Oil droplet sliding velocity was determined using the oil slippage test. The friction coefficient of the surfaces increased with increasing roughness parameter which varied from 26.334 μm at friction coefficient = 0.63 to 13.153 μm at friction coefficient = 0.46. The results from oil slippage test showed that the sliding velocity of the oil drop decreased as the friction coefficient of samples increased. At an inclination angle of 30°, sliding velocity varied from 0.51 cm/s at friction coefficient = 0.63 to 0.92 cm/s at friction coefficient = 0.46. Some of the samples exhibited a deviation in the trend of relationship between friction coefficient and sliding velocity which resulted from the variation in peak height of roughness between the sample surfaces. Oil slippage method predicts the surface behaviours of materials based on their surface parameters.

***Keywords****: Dry friction, image analysis, oil slippage, surface profilometry, surface roughness parameters.*

## 1. INTRODUCTION

Surface roughness is a term used to describe closely packed irregularities, the height, width, and direction that create the prevalent pattern on surfaces. These irregularities can be attributed to the production process. The impact of surface roughness on the behaviours of systems has been considered critical in the characterisation of engineering surfaces for industrial and commercial applications [1], [2]. Castillejos and Tania [3] show that thermal resistance of continuous casting mould slag depends on the surface roughness. The joining strength of two surfaces increases with an increase in surface roughness [4]. By implication, surface roughness has a positive influence on the adhesion behaviour of two surfaces. Conversely, surface roughness has been proven to have detrimental effect on fatigue loading capacity of metals. The notch-like features of rough surfaces serve as stress epicentres and crack initiation sites, thereby reducing the fatigue strength of the material [5]possible applications are direct production of casting molds, tools or turbine blades with internal cooling channels for an optimized cooling efficiency. A disadvantage of the technology is the process-inherent surface roughness, which is critical especially under fatigue loading conditions. Since internal surfaces often cannot be smoothened due to limited accessibility, the objective of this study is to assess the fatigue properties of Ti-6Al-4V samples designed with internal axial channels featuring a rough as-built surface. Samples with various diameters and numbers of channels have been tested not always exhibiting a deterioration of the fatigue performance compared to solid samples. Subsequent fractography by scanning electron microscopy revealed distinct failure mechanisms. Besides the fatigue crack initiation on features of the unmodified internal surfaces, residual porosity in the bulk, i.e. lack-of-fusion defects, keyhole defects and gas pores, respectively, could be identified as crack origin. Relatively low scatter of fatigue lives found is attributed to rapid crack initiation and, thus, the dominant influence of the (micro-. Similarly, the frictional force between two moving parts in contact depends largely on the texture of their surfaces. There are two main explanations for the phenomenon of friction: the adhesion and abrasion theories. Both of these theories are based on the integrity of the surfaces in contact. Therefore, the effects of friction between sliding surfaces depend greatly upon the surface roughness of contact surfaces. Surface roughness could therefore be considered as having a considerable influence on the long-term sustainability both when considering the properties of the finished product as well as during production [6], [7].

Lubricants are used to mitigate the adverse effect of friction, such as achieving lubricity and elongating the life span of machine components during application. The use of solid lubricants as additive to oils and grease is gaining global attention. Oshita et al. [8] reported that the roughness of the surfaces of metal substrates had a great influence on the lubrication performances of solid lubricants during cold forging operations. It was observed that the anti-seizure properties of these solid lubricant substrates were improved significantly as their surfaces became more roughened as a result of improved adhesion strength between the lubricant and the rough surface. Surface roughness plays an important role in determining how objects interact with each other. It is often a good predicting factor of the performance of mechanical

components [9]. For instance, it influences the rate of water absorption in stainless steel [10] and lowers the quenching time of hot surfaces during cooling [11].

Hence, it is of great importance to be able to describe the topography of material surfaces before the use of such materials in various engineering applications [12]. Researchers have shown several methods for investigating surface roughness parameters, which include the use of atomic force microscopy (AFM), power spectral density (PSD), optical profilometry, surface profiler and image analysis [13]–[15]. The use of image analysis as a technique in observing surface characteristics of materials is gaining wide acceptance. This implies that with the use of suitable image analytics software, the profile characteristics of surfaces can be measured electronically [16], [17].

The conventional method of surface roughness analysis involves the use of dry friction contact and wear testing, which may require complex tooling and is time consuming [18], [19]. The study explored the phenomenon of friction between a solid surface and a liquid droplet in surface roughness analysis. In the present study, a new method was developed in which oils of known viscosities were made to slide over solid metallic surfaces and the friction properties of the metallic surfaces were predicted from the interaction between the oils and the surfaces.

## 2. EXPERIMENTAL

### 2.1 Material Preparation

The experimental samples consist of five plates of dimensions cut from mild steel which was obtained from Ilorin Metropolis, Nigeria. The samples were prepared to different degrees of surface roughness by facing operation performed on a Lathe machine using a carbide tip boring tool at different speeds (48, 66, 92, 132, and 185 rpm) and depths of cut (2.5, 2.0, 1.5, 1.0, and 0.5 mm). Standard roughness parameters are: arithmetical mean deviation of the profile ($R_a$), ten point height of irregularities ($R_z$), maximum height of the profile ($R_{max}$), maximum height of profile peak ($R_p$), and profile bearing length ratio ($t_p$) [20]. Table 1 shows the machining details of the samples.

### 2.2 Surface Profilometry and Analysis

The prepared surfaces of the samples were scanned photographically with the aid of a Canon EOS 5D Mark IV Kit camera. The line profiling and surface profile analysis were done using Image J software version 1.4.3.67. The method of surface profilometry was adopted from the studies of Altan & Celik [4], and Castillejos and Tania [3].

**Table 1.** Machining Details of Samples

| Sample | Depth of Cut (mm) | Cutting Speed (rpm) |
|---|---|---|
| 1 | 2.5 | 48 |
| 2 | 2.0 | 66 |
| 3 | 1.5 | 92 |
| 4 | 1.0 | 132 |
| 5 | 0.5 | 185 |

## 2.3 Investigation of Solid Metallic Surfaces Using the Dry Friction Method

Experimental set-up for establishing the static friction coefficient projected specially for this investigation is shown in Fig. 1 (a and b). The schematic representation of the set-up is shown in Fig. 2. The test sample was placed on an inclined plane apparatus, as shown in Fig. 1. A solid block of known and recorded mass ($m$) was kept on the surface of the plane. The angle of inclination was adjusted until the block just began to move. The angle at which the first movement was observed was recorded, which indicated static friction [21]. The coefficient of static friction was calculated using Eqs. (1)–(3). The vertical and horizontal forces were balanced to obtain Eqs. (1) and (2).

$$\mathrm{N} = \mathrm{mg}\cos\theta, \tag{1}$$

$$F = \mathrm{mg}\sin\theta, \tag{2}$$

Coefficient of static friction,

$$\mu = \frac{\mathrm{F}}{\mathrm{N}} = \frac{\mathrm{mg}\sin\theta}{\mathrm{mg}\cos\theta} = \tan\theta, \tag{3}$$

where F – frictional force in Newton; m – mass of the body in kg; g – gravitational acceleration in m/s$^2$; N – normal force exerted on the body by the plane due to gravity and $\theta$ – the angle of inclination. The nature of the relationship between roughness parameter ($R_a$) and the static coefficient of friction ($\mu$) was investigated graphically.

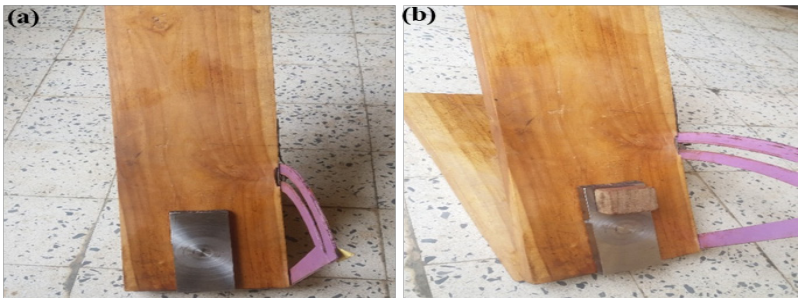


*Fig. 1.* Set up for dry friction investigation: (a) without the solid block; (b) with the solid block.

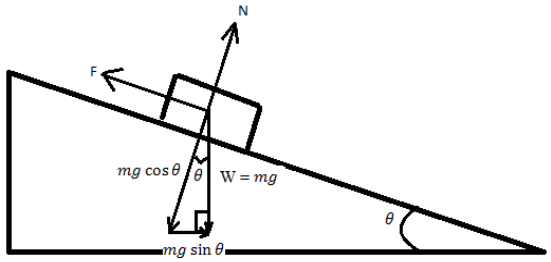


*Fig. 2.* Schematic representation of the dry friction inclined plane set-up.

## 2.4 Investigation of Solid Metallic Surfaces Using the Oil Slippage Method

An oil drop whose centre of mass moved with a steady velocity, $u$, down a plane inclined at an angle, $\alpha$ with the horizontal as shown in Fig. 3 was investigated. The fluid formed a steady stream moving downwards under the action of gravity. The

velocity distribution of different material properties and different inclination angles was examined. The impact of volume of drop and angle of inclination on drop sliding velocity were determined. The oil drop has the density, $\rho$, the surface tension, $\sigma$, and the viscosity, $\eta$. It was assumed that was dependent on $\sigma$, $\eta$, and $\rho$ [22]. Figure 4 shows the set up for the oil slippage test.

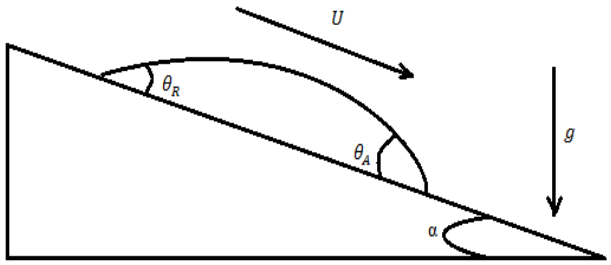


*Fig. 3.* Schematic diagram of a sliding drop down an inclined plane.

*Fig. 4.* Set-up for oil slippage test.

LUBCON Super XV 20W50 Oil of 165.5 mPa.s viscosity was used to vary the fluid dynamics and interfacial properties in this study. The experiments were carried out under standard laboratory conditions. The inclined plane was set up as shown in Fig. 4. The test sample was placed on the plane and set to various angles of inclination to investigate the velocity of oil drop. A known volume of oil is dropped on the plane and was allowed to slide down a marked distance ($s$) of 10 cm across the centre of the test material. The marked distance is 5 cm towards the centre and 5 cm away from the centre. Hence, an average distance of 5 cm was taken into account assuming the test material has a uniform surface texture over the average 5cm distance. The time taken ($t$) for the drop to travel through the marked distance ($s$) was recorded and the velocity ($u$) of the oil drop down the experimental plane was calculated by Eq. (4):

$$u = \frac{s}{t}. \tag{4}$$

The investigation was taken further by varying the volume of the oil drop on the sample surfaces to investigate the indepen-

dent effect of each of these parameters on the sliding velocity of the drop down the plane. The correlation between roughness parameter ($R_a$), the coefficient of friction ($\mu$) and the sliding velocity of oil drop is done by making a plot of the coefficient of friction against the sliding velocity. A mathematical relationship between coefficient of dry friction ($\mu$) and sliding velocity ($u$) due to oil slippage was deduced graphically.

## 3. RESULTS AND DISCUSSION

### 3.1 Surface Profilometry

The line profiling and surface profile analysis were done using Image J software version 1.4.3.67. Figures 5–9 show the representative line profiles of sample surfaces. Arithmetic mean deviation of the roughness profile ($R_a$) was calculated for all the line profiles. The results obtained from surface profilometry reveal the important parameters to be considered in this study. The roughness parameters are captured in Table 2. It reveals that the values of mean roughness ($R_a$) reduced from 26.334 µm in sample 1 (2.5 mm depth) to 13.153 µm in sample 5 (0.5 mm depth). This clearly depicts that the surface roughness depends on the depth of cuts made on the surface. However, the roughness kurtosis increased from 3.001 µm in sample 1 to 7.177 µm in sample 5, which demonstrated that as the depth of cut reduced, there was a reduction in the noise level of the image obtained thereby leading to a sharp curve with short tail [23]. Similarly, the roughness skewness, which is a measure of the direction where the bulk of the values lie either to the right or the left of the mean also increased from1.579 µm in sample 1 to 2.289 µm in sample 5. This shows that as the cutting depth decreases, the bulk of the values of the probability density function are to the right of the mean [24].

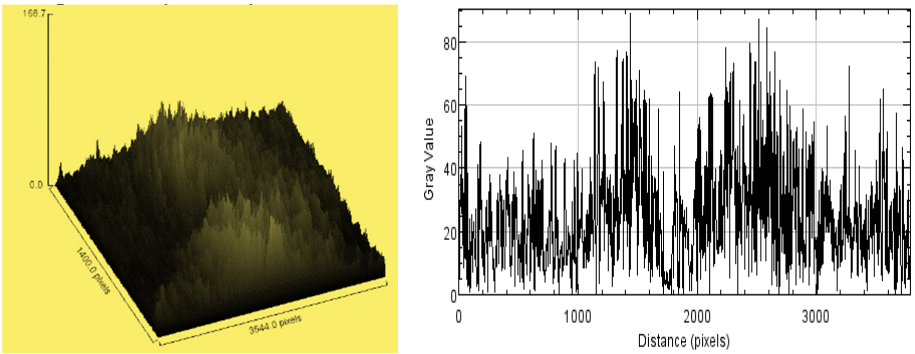


*Fig. 5.* Surface roughness $R_a$ for sample 1.

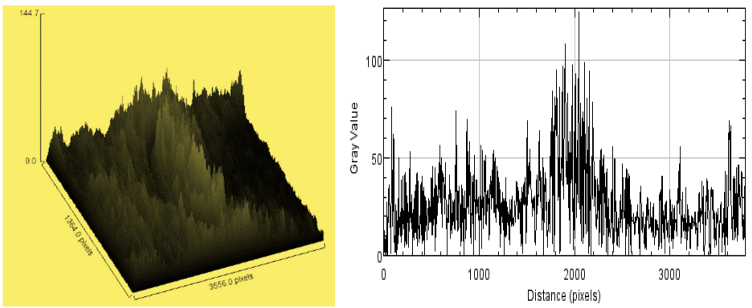


*Fig. 6.* Surface roughness $R_a$ for sample 2.

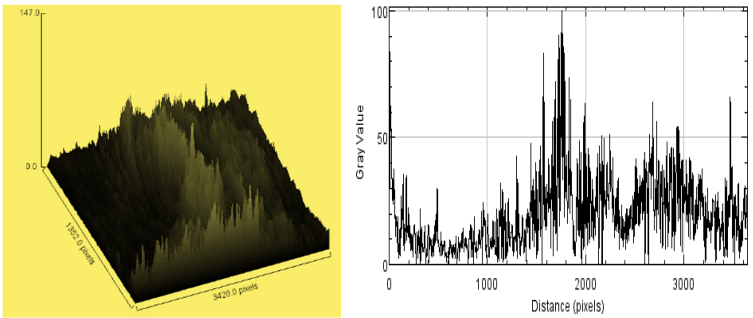


*Fig. 7.* Surface roughness $R_a$ for sample 3.

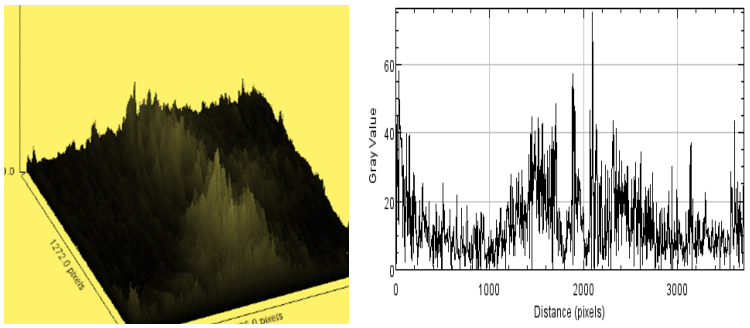


*Fig. 8.* Surface roughness $R_a$ for sample 4.

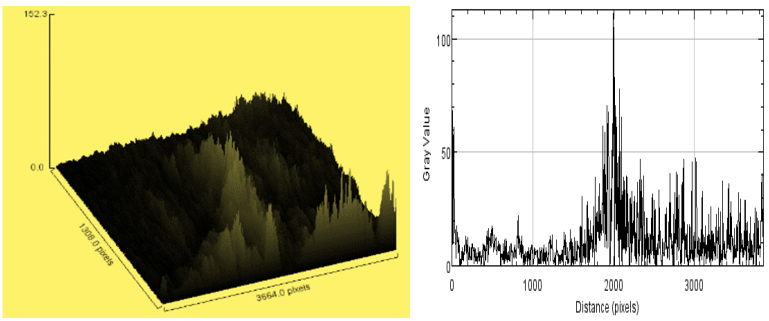


*Fig. 9.* Surface roughness $R_a$ for sample 5.

**Table 2.** Roughness Parameters

| Sample | $R_q$ (μm) | $R_a$ (μm) | $R_{sk}$ (μm) | $R_{ku}$ (μm) | Highest Peak (μm) | Lowest Valley (μm) | Total Height (μm) |
|---|---|---|---|---|---|---|---|
| 1 | 32.172 | 26.334 | 1.579 | 3.001 | 168.667 | 0 | 168.667 |
| 2 | 27.680 | 22.698 | 1.572 | 3.045 | 144.667 | 0 | 144.667 |
| 3 | 25.788 | 20.696 | 1.697 | 3.648 | 147.000 | 0 | 147.000 |
| 4 | 21.458 | 16.278 | 1.933 | 4.862 | 151.670 | 0 | 151.670 |
| 5 | 18.474 | 13.153 | 2.289 | 7.177 | 102.333 | 0 | 102.333 |

*$R_a$ – mean roughness, *$R_q$ – root mean square roughness, *$R_{sk}$ – roughness skewness and *$R_{ku}$ – roughness kurtosis

## 3.2 Analysis of Solid Metallic Surfaces Using the Dry Friction Inclined Plane Method

The experimental values obtained from the dry friction test of sample surfaces are shown in Table 3. This is a compilation of the average values of inclination angles and static coefficients of friction. The values varied from 26.334 μm at $\mu_1$ = 0.63 to 13.153 μm at $\mu_5$ = 0.46. The roughness values increased as friction coefficient increased. Figure 10 elaborates the variation of arithmetic mean deviation of the roughness profile ($R_a$) with respect to the friction coefficient during dry sliding. The plot shows a positive slope with increasing uphill trend. The profilometric feature analysis of the sample surfaces established the correlation between coefficient of friction and surface roughness. It affirms that coefficient of friction increases with an increase in surface roughness parameter [19].

**Table 3.** Results of Dry Friction Inclined Plane Method

| Sample | Angle of Inclination ($\theta^o$) | Friction Coefficient $\mu_S$ | Surface Roughness $R_a$ (μm) | Highest Peak (μm) |
|---|---|---|---|---|
| 1 | 32.33 | 0.63 | 26.33 | 168.67 |
| 2 | 30.83 | 0.60 | 22.70 | 144.67 |
| 3 | 30.00 | 0.58 | 20.70 | 147.00 |
| 4 | 27.67 | 0.52 | 16.28 | 151.67 |
| 5 | 24.83 | 0.46 | 13.15 | 102.33 |

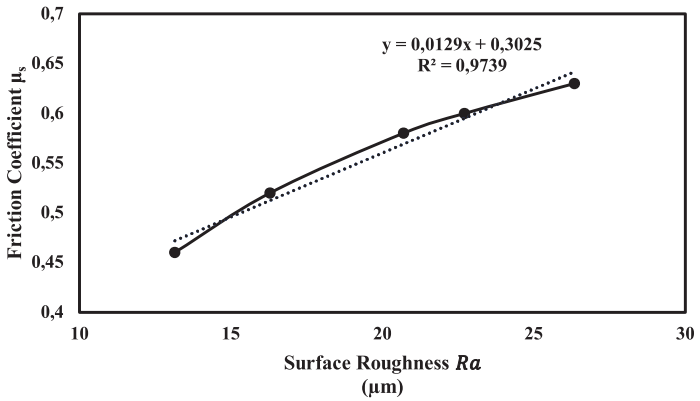


*Fig. 10.* Dependence of friction coefficient on surface roughness.

### 3.3 Analysis of Solid Metallic Surfaces Using Oil Slippage Method

The graphs of the experimental values obtained from the oil slippage test of sample surfaces are shown in Figs. 11 and 12. Figure 11 shows the graphical relationship between sliding velocity and angle of inclination. It was observed that at higher angles of inclination than the repose angles obtained from the dry friction test, the convergence in the values of velocity of all five samples became greater (the values of velocity started getting close). It could be opined that at greater inclination angles than the angle of repose obtained for a particular sample, the effect of surface roughness over the sliding velocity of oil drop reduced. Oshita et al. [8] posited that an increase in surface roughness led to an increase in adhesion strength between the oil and rough surface, which might result in a decrease in the sliding velocity of the oil.

However, the results of this study reveal that the sliding velocity of oil drops increases with greater values of inclination angle. This is due to the reduction in the pinning effect of the roughness ridges over the oil drop as the inclination angle increases, leading to a greater sliding velocity of the oil drop as it slides over the surface. A deviation in trend was observed from the plots for each sample at inclination angles close to or greater than the repose angles obtained from dry friction test. This can mean that the oil slippage test has its critical angle of operation. To establish the nature of the relationship between the volume of oil drop and the sliding velocity of the drop, values of sliding velocity obtained from oil slippage test of each sample surface were plotted against the set volumes of oil drop, as shown in Fig. 12.

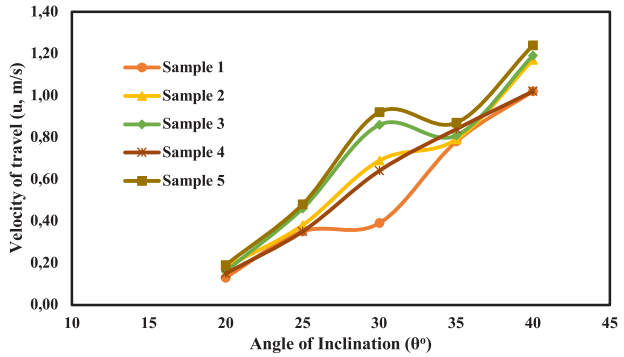


*Fig. 11.* Relationship between velocity of travel and angle of inclination.

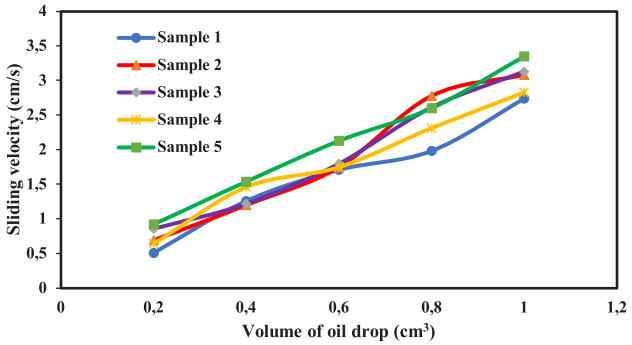


*Fig. 12.* Relationship between sliding velocity and volume of oil drop.

The results of experimental investigations reveal that the sliding velocity of oil drops increases with greater values of oil drop volume. This is because the forces acting on the oil drop as it slides down the surface depend upon the volume of the oil drop. The results of experimental investigations depict that the sliding velocity of oil drops increases as friction coefficient values decrease. The oil droplet encountered ridges of varying heights over each of the surfaces which affected the sliding velocity of the oil drop. It can be asserted that an increment in the values of dry friction coefficient could mean a decrement in the values of velocity. However, by careful observation of the data set obtained from the oil slippage test, sample 4 showed an unusual trend.

Despite the low value of friction coefficient, the sliding velocity appears lower than expected. As seen from the surface profilometry results, the highest peak value for sample 4 is only lower to that of sample 1. The oil drop has to travel through higher surface ridges in sample 4 than in samples 2, 3 and 5. Sample 3 has a higher peak value than sample 2, but the difference between their highest peak values are almost negligible. More so, at some inclination angles, the roughness ridges of sample 3 are more active than that of sample 2. It could be said that the roughness height of the surface is better taken into account with the oil slippage test method than in the dry friction method.

Mathematical model for the relationship between friction coefficient and sliding velocity was determined graphically from the plot in Fig. 13 and shown in Eq. (5). The mathematical relationship shows that if the sliding velocity is ascertained from oil slippage method, the coefficient of friction can be calculated for mild steel using the relationship. Hence, there would be no need for the conventional dry friction method. However, it is worth noting that the sliding velocity depends on certain parameters such as volume of drop and angle of inclination.

$$v = 0.0036\mu^2 + 0.0016\mu + 0.774 \quad (5)$$

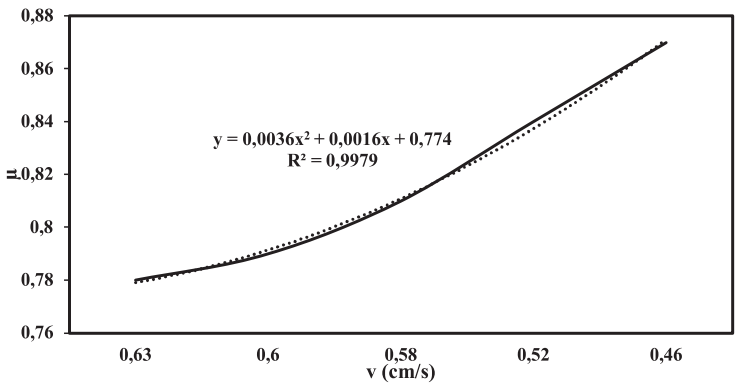


*Fig. 13.* Sliding velocity vs coefficient of dry friction.

## 4. CONCLUSION

Contact surface roughness has direct influence on the static friction coefficient. Generally, it can be stated that the static friction coefficient increases with surface roughness parameters. The machining processes employed in the preparation of

sample surfaces result in the difference in static friction coefficient values of the surfaces. The results of the study have also shown that there is a functional dependence between the friction coefficient and the sliding velocity of oil drop down a solid metallic surface. It should be noted that several other parameters affect the sliding velocity of the oil drop. It is important to pay close attention to these parameters. The relationship between the friction coefficient and the sliding velocity of oil drop is a good predicting factor in surface roughness characterisation studies. The oil drop method of investigation proves to be the development of the conventional dry sliding method as it puts all parameters that describe the texture of a surface into better consideration.

Subsequent study should examine a mathematical relationship between sliding velocity of the oil slippage method and coefficient of dry friction based on the angles of inclination in order to be able to predict the coefficient of dry friction from performing only the oil drop experiment, thereby eliminating the need for dry friction method.

## REFERENCES


1. Vazquez-Calvo, C., Alvarez De Buergo, M., Fort, R., & Varas-Muriel, M.J. (2012). The Measurement of Surface Roughness to Determine the Suitability of Different Methods for Stone Cleaning. *J Geophys Eng*, *9*, S108–17. https://doi.org/10.1088/1742-2132/9/4/S108.
2. Al-Samarai, R.A.H., Ahmad, K.R., & Al-Douri, Y. (2012). Evaluate the Effects of Various Surface Roughness on the Tribological Characteristics under Dry and Lubricated Conditions for Al-Si Alloy. *J Surf Eng Mater Adv Technol*, *2*, 167–73. https://doi.org/10.4236/jsemat.2012.23027.
3. Castillejos, E.A.H., & Tania, M.F.F. (2019). Characterization of Roughness, Porosity and Thermal Resistances of Continuous Casting Mold Slag Layers Devitrified and Crystallized in Laboratory. *Metall Mater Trans B Process Metall Mater Process Sci*, *50* (24), 36–53. https://doi.org/10.1007/s11663-019-01655-4.
4. Altan, T., & Celik, S. (2020). Effect of surface roughness of the metallic interconnects on the bonding strength in solid oxide fuel cells. *Int J Hydrogen Energy,* 1–12. https://doi.org/10.1016/j.ijhydene.2020.03.136.
5. Günther, J., Leuders, S., Koppa, P., Tröster, T., Henkel, S., Biermann, H., & Niendorf, T. (2018). On the effect of internal channels and surface roughness on the high-cycle fatigue performance of Ti-6Al-4V processed by SLM. *Mater Des*, *143,* 1–11. https://doi.org/10.1016/j.matdes.2018.01.042.
6. Bera, B. (2014). Generalized adhesion theory of friction. In *Asiat. Conf.* (pp. 2–4), 17–20 February 2014, Agra, India.
7. Anvari, A. (2016). Friction coefficient variation with sliding velocity in copper with copper contact. *Period Polytech Mech Eng, 60,* 137–41. https://doi.org/10.3311/PPme.8429.
8. Oshita, K., Yanagi, M., Okada, Y., Komiyama, S., & Wang, Z. (2017). Effect of surface roughness on improved lubricity under an ironing condition using a synthetic mica-organic intercalation compound. *Tribol Online,12*, 193–202. https://doi.org/10.2474/trol.12.193.
9. Zhai, C., Gan, Y., Hanaor, D., Proust, G., & Retraint, D. (2016). The Role of Surface Structure in Normal Contact Stiffness. *Exp Mech, 56*, 359–68. https://doi.org/10.1007/s11340-015-0107-0.
10. Manaf, N.D., Fukuda, K., Subhi, Z.A., & Mohd-Radzi, M.F. (2019). Influences of surface roughness on the water adsorption on austenitic stainless steel. *Tribol Int, 136*, 75–81. https://doi.org/10.1016/j.triboint.2019.03.014.

11. Deendarlianto, A., Takata, Y., Kohno, M., Hidaka, S., Wakui, T., Majid, A.I., … & Widyaparaga, A. (2016). The effects of the surface roughness on the dynamic behavior of the successive micrometric droplets impacting onto inclined hot surfaces. *Int J Heat Mass Transf, 101*, 1217–26. https://doi.org/10.1016/j.ijheatmasstransfer.2016.05.132.
12. Menezes, P.L., & Kailas, S.V. (2016). Role of surface texture and roughness parameters on friction and transfer film formation when UHMWPE sliding against steel. *Biosurface and Biotribology*, *2*, 1–10. https://doi.org/10.1016/j.bsbt.2016.02.001.
13. Feng, D., Shen, M., Peng, X.D., & Meng, X.K. (2017). Surface Roughness Effect on the Friction and Wear Behaviour of Acrylonitrile–Butadiene Rubber (NBR) under Oil Lubrication. *Tribol Lett, 65,* 1–14. https://doi.org/10.1007/s11249-016-0793-5.
14. Jacobs, T.D.B., Junge, T., & Pastewka, L. (2017). Quantitative Characterization of Surface Topography Using Spectral Analysis. *Surf Topogr Metrol Prop, 5*, 1-10. https://doi.org/10.1088/2051-672X/aa51f8.
15. Erinosho, M.F., Akinlabi, E.T., & Johnson, O.T. (2017). Characterization of Surface Roughness of Laser Deposited Titanium Alloy and Copper Using AFM. *Appl Surf Sci, 435,* 393–7. https://doi.org/10.1016/j.apsusc.2017.11.131.
16. Orhadahwe, T.A., Adeleke, A.A., Aweda, J.O., Ikubanni, P.P., & Odusote, J.K. (2020). Microstructural Image Analyses of Mild Carbon Steel Subjected to a Rapid Cyclic Treatment. *J Chem Technol Metall*, *55*, 198–209.
17. Adeleke, A.A., Ikubanni, P.P., Orhadahwe, T.A., Aweda, J.O., Odusote, J.K., & Agboola, O.O. (2019). Microstructural Assessment of AISI 1021 Steel under Rapid Cyclic Heat Treatment Process. *Results Eng*; *4*, 1–4. https://doi.org/10.1016/j.rineng.2019.100044.
18. Jiang, H., Browning, R., Fincher, J., Gasbarro, A., Jones, S., & Sue, H.J. (2008). Influence of Surface Roughness and Contact Load on Friction Coefficient and Scratch Behavior of Thermoplastic Olefins. *Appl Surf Sci*, *254,* 4494–9. https://doi.org/10.1016/j.apsusc.2008.01.067.
19. Sedlaček, M., Podgornik, B., & Vižintin, J. (2009). Influence of Surface Preparation on Roughness Parameters, Friction and Wear. *Wear, 266*, 482–7. https://doi.org/10.1016/j.wear.2008.04.017.
20. Ivković, B., Djurdjanović, M., & Stamenković, D. (2000). The Influence of the Contact Surface Roughness on the Static Friction Coefficient. *Tribol Ind, 22*, 41–4.
21. Ambekar, A.G. (2007). *Mechanism and Machine Theory*. Eastern Ec. New Delhi: Prentice-Hall of India Private Limited.
22. Kim, H.Y., Lee, H.J., & Kang, B.H. (2002). Sliding of Liquid Drops Down an Inclined Solid Surface. *J Colloid Interface Sci*, *247,* 372–80. https://doi.org/10.1006/jcis.2001.8156.
23. Kumar, V., & Gupta, P. (2012). Importance of Statistical Measures in Digital Image Processing. *Int J Emerg Technol Adv*, *2*, 56–62.
24. Motoyoshi, I., Nishida, S., Sharan, L., & Adelson, E.H. (2007). Image Statistics and the Perception of Surface Qualities. *Nature*, *447,* 206–9. https://doi.org/10.1038/nature05724.

sciendo

LATVIAN JOURNAL OF PHYSICS
AND TECHNICAL SCIENCES
2021, N 4

DOI: 10.2478/lpts-2021-0033

# EXPERIMENTAL STUDY OF THE CHAOTIC JERK CIRCUIT APPLICATION FOR CHAOS SHIFT KEYING

F. Capligins*, A. Litvinenko**, A. Aboltins,
E. Austrums, A. Rusins, D. Pikulins

Faculty of Electronics and Telecommunications,
Institute of Radioelectronics, Riga Technical University,
12 Azenes Str., Riga, LV-1048, LATVIA
*e-mail: filips.capligins@rtu.lv
**e-mail: anna.litvinenko@rtu.lv

The paper presents a study of the chaotic jerk circuit (CJC) employment capabilities for digital communications. The concept of coherent chaos shift keying (CSK) communication system with controlled error feedback chaotic synchronization is proposed for a specific CJC in two modifications. The stability of chaotic synchronization between the two CJCs was evaluated in terms of voltage drop at the input of the slave circuit and the impact of channel noise using simulations and experimental studies.

**Keywords:** *Chaotic communication, chaotic synchronization, chaos shift keying, experimental study, jerk circuit, secure communication system, Sprott circuit.*

## 1. INTRODUCTION

Possible applications of chaotic signals in the field of digital communications have been studied since the early 90s. The main features of chaotic signals that are desirable for telecommunications include noise-like appearance, high entropy, spread spectrum, resistance to jamming and robustness in multipath environments [1].

A chaotic system (including a chaotic generator) is a deterministic nonlinear dynamic system that can be mathematically described by a system of differential equations (e.g., Lorenz system) or using discrete maps (e.g., logistic map). It can also be implemented using an electronic circuit like Chua's circuit.

This study focuses on a chaotic jerk circuit (CJC). Chaotic jerk systems and their circuit implementations were discovered only at the beginning of the 21st century by

Sprott [2], [3]. Jerk circuits are relatively simple and robust to parametric mismatch, so they are suitable candidates for practical implementation.

In general, a *jerk* is a third-time derivative of some variable $x$, which would correspond to the first-time acceleration derivative in a mechanical system. Thus, a *jerk equation* is a third-order time differential equation. Within the specific parameter range, jerk equations can provide chaotic solutions. For example, simple jerk equation:

$$\dddot{x} + \ddot{x} + x + \alpha^2 \exp\left(\frac{\dot{x}}{\alpha}\right) = 0 \quad (1)$$

can provide chaotic solutions for $\alpha < 0.27$, except for some small periodic windows [4]. The CJC can be considered an analogue computer that solves the jerk equation using electronic components with voltage or current as variables.

Another useful property of chaotic systems is chaotic synchronization, when one chaotic system (*master*) is tuned to another (*slave*) so that they produce the same outputs. Two separate identical chaotic systems will generate two completely uncorrelated signals if there are even smallest differences in initial conditions, but with chaotic synchronization, their dynamics can be tuned so that their trajectories in phase space become equal. If the master chaotic system is in the transmitter and slave – in the receiver, their synchronization can be used to provide secure communications that are usually extremely difficult to intercept or decode by any other party without having the exact receiver system [1].

Two chaotic circuits must be coupled in an appropriate way for synchronization to be possible. One of the first and simplest chaotic synchronization techniques proposed by Pecora and Carroll in 1991 [5] uses direct coupling of two identical chaotic systems. In this case, one of the slave system variables is replaced by the corresponding variable from the master system, forcing other slave system variables adjust their trajectories to master system variables. Another common technique is error feedback synchronization [6] – the instantaneous difference between the signal received from the master system and the signal from the slave system (which is composed using the same function as in the transmitter) produces an error signal which, through the feedback loop, modifies the state of the receiver to minimise the error. It has been shown [7] that linear error feedback synchronization provides better performance than Pecora-Carroll synchronization. In the present study, specific controlled error feedback synchronization [8] is implemented and discussed in Section 3.

Existing chaos-based communication systems can be divided into two classes: with coherent and non-coherent detection. In coherent detection schemes, synchronization is exploited to generate a copy of the transmitted chaotic signal at the receiver, which is then used in various techniques to reconstruct the transmitted data. In non-coherent detection schemes, synchronization is not used. Data recovery is performed by detecting some features of the received signal without regenerating any local chaotic signal on the receiver side or the need for channel state information [9]. Common examples of coherent modulation techniques are chaotic masking and chaos shift keying (CSK). For non-coherent modulation, examples include chaos on-off keying (COOK), differential chaos shift keying (DCSK) and correlation delay shift keying (CDSK).

Chaotic communication systems with non-coherent detection are easier to implement, but they mainly rely on additional data encryption algorithms for secure transmission. Coherent systems involve cha-

otic synchronization for data transmission, which makes much higher levels of security possible, but achieving stable synchronization may be challenging.

In the present study, the CSK technique is chosen, and the concept of a communication scheme for CJC is proposed (see Section 4). For a typical CSK, the transmitter uses two different chaotic generators, one representing the "1" bit, the other – "0". Active switching between both transmitting chaotic systems is performed for each corresponding bit of the digital data sequence. On the receiver side, two chaotic generators, identical to those on the transmitter, receive the transmitted signal. During the transmission of a single bit, the synchronization occurs only in one of the receiving chaotic generators. Estimation of the transmitted bit is performed by comparing the synchronization errors or correlation coefficients between both receiver generators. If the chaotic generators used to transmit both data bits produce chaotic signals with very similar statistical properties, such a communication system is hard to intercept and decode without having exact chaotic generators and knowing exact parameters used for transmission setup. The drawback of CSK is speed – the bit duration must be long enough for synchronization to take place.

Due to the novelty of CJCs, the number of presented studies is somewhat limited, especially in the field of possible applications of CJCs in communication systems. One study [10] proposes using CJC in the DCSK communication scheme, and another [11] – in the CDSK scheme. The possibilities of using two synchronized CJCs for a chaotic masking communication system are studied in [12]–[15]. The present study is the first to propose the concept of a coherent CSK communication system with controlled error feedback synchronization of the jerk circuits.

This paper is organised as follows. Section 2 briefly describes the two CJCs used – Sprott's original jerk circuit and its modification. In Section 3, the implemented controlled error feedback synchronization method is reviewed. The proposed CSK scheme is described in Section 4. In Section 5, the synchronization stability between the same and different CJCs is investigated concerning voltage drop at the input of the slave circuit and the impact of channel noise. Finally, Section 6 provides conclusions.

## 2. SPROTT CHAOTIC JERK CIRCUIT

For the present study a specific CJC proposed by Sprott in [4] was chosen. This jerk circuit is a relatively simple chaotic oscillator that, unlike many other chaotic circuits, is robust to parameter variations and does not require careful tuning of component values. It uses a diode as a nonlinear element whose characteristics are not critical, and the only reactive components are three identical capacitors. As shown in Fig. 1, this CJC consists of three consequent operational amplifier integrators, an inverter, a diode, and two feedback loops. All resistors and all capacitors should be of the same nominal values, chosen as $R$ = 10 kΩ and $C$ = 100 nF for this study. This CJC electronically implements a system of three first-order equations:

$$\begin{cases} \dot{x} = y \\ \dot{y} = z \\ \dot{z} = -z - x - 10^{-9}\left[\exp\left(\frac{y}{0.026}\right) - 1\right] \end{cases} \quad (2)$$

that can be decomposed from the general jerk equation (1) with slight modification, so that the exponential function describes a simplified mathematical model of a typical silicon diode.

Since the CSK modulation scheme requires two chaotic generators, a modification of this CJC (see Fig. 2) with an inverted diode direction is proposed. Mathematical expression (2) can be changed into:

$$\begin{cases} \dot{x} = y \\ \dot{y} = z \\ \dot{z} = -z - x + 10^{-9}\left[\exp\left(\frac{-y}{0.026}\right) - 1\right] \end{cases} \quad (3)$$

to represent the modified Sprott CJC. Further on, the first CJC will be addressed as a CJC with a direct diode, the second – as a CJC with an inverted diode.

For a visual comparison of both CJCs, a projection of the chaotic attractor was recorded from the prototype circuits (reviewed in Section 5) for the CJC with a direct diode (see Fig. 3) and for the CJC with an inverted diode (see Fig. 4). Both attractors exhibit similar dynamics, but for opposite voltage values.

Sprott CJC generates broadband chaotic signal. However, it has a dominant oscillation frequency, which can be approximately predicted [4] as follows:

$$f_{\text{dom}} = \frac{0.792552}{2\pi RC}. \quad (4)$$

For the selected values of $R$ and $C$, this gives 126 Hz, which is close to the dominant oscillation frequency observed in simulations and experiments.

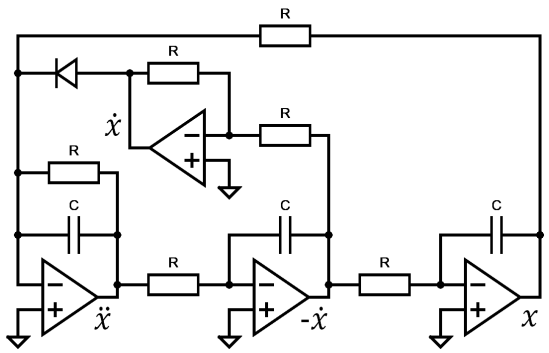


*Fig. 1.* Schematic of the Sprott CJC [4], with direct diode position.

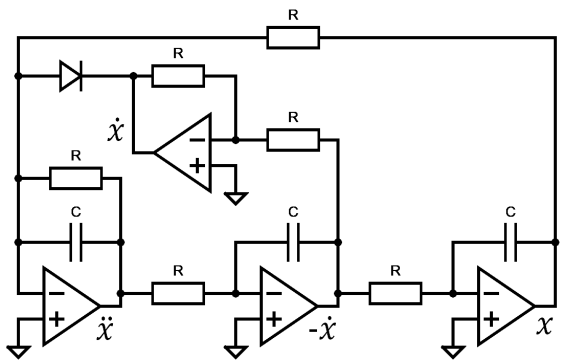


*Fig. 2.* Schematic of the modified Sprott CJC, with inverse diode position.

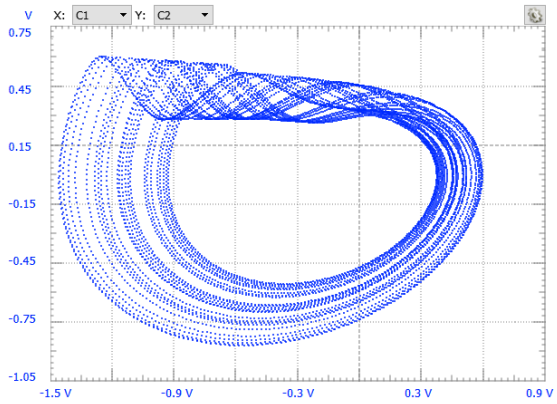


*Fig. 3.* Attractor projection in the phase plane, recorded from CJC prototype with direct diode position.

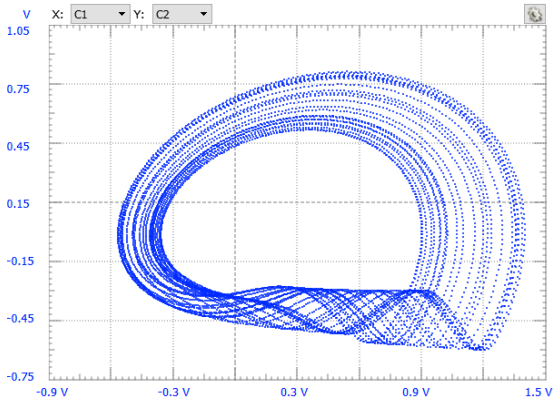


*Fig. 4.* Attractor projection in the phase plane, recorded from CJC prototype with inverse diode position.

## 3. ERROR FEEDBACK SYNCHRONIZATION

According to [8], two jerk circuits can be synchronized using a controlled error feedback method called practical finite-time synchronization. This method is designed explicitly for jerk circuits and aims at attaining fast convergence speed for the synchronization and reducing system cost.

In general terms, the master CJC can be described by the system of equations:

$$\begin{cases} \dot{x}_1 = x_2 \\ \dot{x}_2 = x_3 \\ \dot{x}_3 = a_1 x + a_2 x_2 + a_3 x_3 + f(x_1, x_2, x_3) \end{cases}, \tag{5}$$

whereas the slave CJC equation system:

$$\begin{cases} \dot{y}_1 = y_2 + k_1 S \\ \dot{y}_2 = y_3 + k_2 S \\ \dot{y}_3 = a_1 y + a_2 y_2 + a_3 y_3 + f(y_1, y_2, y_3) + k_3 S \end{cases} \tag{6}$$

will have additional components $k_i S$ (synchronization controller) added for each state variable of the slave system. According to the equation:

$$S = \sum_{i=1}^{3}(y_i - x_i), \tag{7}$$

$S$ is the sum of the differences between the state variables of both systems, which is also equal to the difference of the sums of the state variables of each system. If the $S$ value for coupled CJC reaches zero, both systems are synchronized, but in a practical synchronization, $S$ can only reduce to a small non-zero value. Further in this paper this difference is designated as a synchronization error, since its value directly corresponds to the difference between the states of the master and slave CJC. By employing the feedback, the synchronization error is applied to the slave system, but differently for each state variable. The coefficients $k_i$ are intended to individually modify the sign and/or strength of the synchronization error signal applied to each state variable of the slave system in a manner that ensures high convergence speed for the synchronization. Consequently, the dynamics of the slave CJC is modified in a way that reduces synchronization error when two identical jerk circuits are coupled.

This method was used for synchronization of the Sprott CJCs. As shown in Fig. 5, the sums of the state variables of each system and their differences (synchronization error) are calculated electronically using operational amplifiers. Essential parts of this synchronization scheme are resistors *Rc1*, *Rc2* and *Rc3*, which implement the function of $k_i$ variables by controlling the amount of current from the synchronization error signal applied to each state variable (feedback strength).

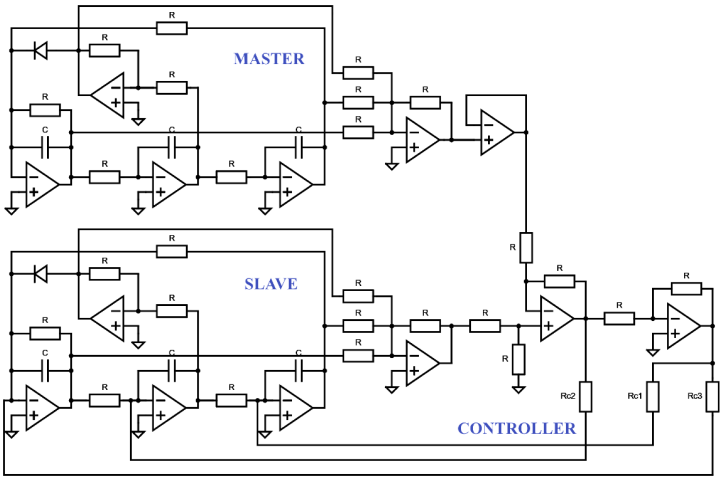


*Fig. 5.* Schematic of the synchronization circuit for two identical CJCs using the method presented in [8].

Resistance values that provide an acceptable quality of chaotic synchronization can be approximately calculated [8], but in this study, an empirical approach was chosen to determine appropriate resistance values. Using a prototype circuit with two synchronizable CJCs, the resistors were replaced with potentiometers, and the rms voltage of the synchronization error, as well as the correlation graph between the equivalent state variables on both (master and slave) CJCs, were observed with

different resistance values. Satisfactory synchronization results were obtained for *Rc1* = 50 kΩ, *Rc2* = 10 kΩ and *Rc3* = 500 Ω; therefore, these values were chosen for the further studies of synchronization stability, discussed in Section 5.

Synchronization simulation for two identical CJCs shows (see Fig. 6) that the time required for the synchronization error to converge to a small non-zero value is approximately 10 ms – the synchronization speed is related to the dominant frequency of the jerk circuit and, according to (4), the speed can be increased by decreasing *R* or *C* values to any preferred level. However, maintaining the stability of the electronic circuit becomes more challenging at higher frequencies.

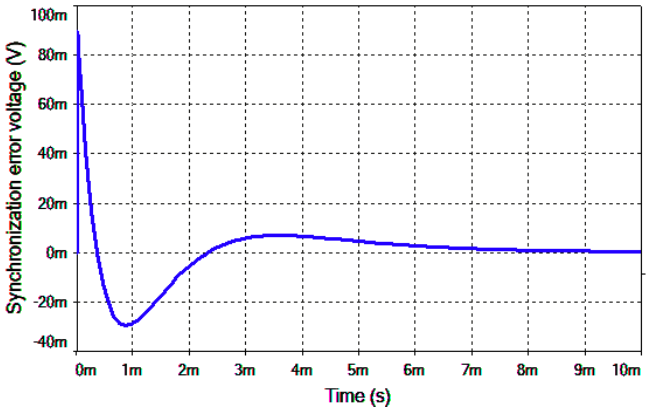


*Fig. 6.* Synchronization error signal reduction due to synchronization between master and slave CJCs with direct diode position and different initial conditions, obtained by *Multisim* simulation.

## 4. CHAOS SHIFT KEYING

It is notable that the error feedback synchronization method, described in the previous Section, works for two CJCs with direct diodes as well as for two CJCs with inverse diodes, without any additional tuning. Nevertheless, if two different CJCs are coupled in the proposed synchronization scheme, no synchronization occurs. To be more precise, some partial synchronization can be observed, but the rms voltage of the synchronization error is much larger than for two synchronized identical CJCs. This property plays a vital role in the proposed CSK communication system.

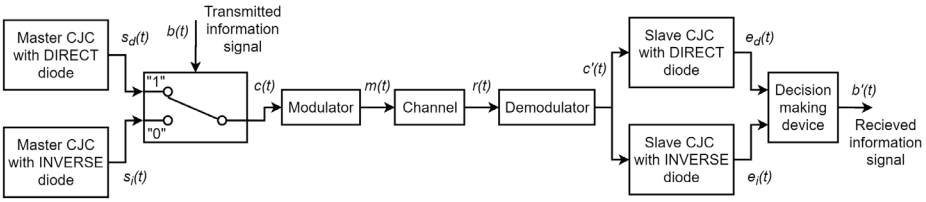


*Fig. 7.* Proposed coherent CSK communication system with controlled error feedback synchronization of jerk circuits.

The proposed concept (see Fig. 7) is as follows. The transmitter has two CJCs, with a direct diode and with an inverted diode, which produces two different chaotic signals $s_d(t)$ and $s_i(t)$. Both chaotic signals are the sums of the three CJC state variables. The value of the transmitted binary information signal $b(t)$ is used to control a switch that selects the corresponding chaotic signal. The selected signal $c(t)$ should be modulated for transmission over the wireless channel. At the receiver the transmitted signal is demodulated and used in the synchronization scheme for both types of controlled slave CJCs, producing two synchronization errors $e_d(t)$ and $e_i(t)$ as outputs. The rms values of these errors, calculated over the bit duration period, must be compared to determine the value of the transmitted bit.

This communication system can be further simplified by reducing the number of CJCs required. For a transmitter, switching between two different jerk systems can be achieved by switching between two diodes with opposite directions in the same CJC. This approach can slightly reduce the size and complexity of the transmitter, but it may also reduce the maximal speed of the communication system given for the same bit error ratio due to the additional time spent on transients within the transmitting CJC. In a receiver, a single synchronizable slave CJC may be sufficient to estimate the transmitted bit using a threshold level of synchronization error, but such simplified detection can potentially reduce the noise immunity of the communication system.

To validate the proposed concept of the CSK communication system, the stability of synchronization error was evaluated under different conditions for all four possible master and slave CJC interconnections. The evaluation was made for a simplified system model, for a baseband equivalent, without additional modulation and wireless channel. The experimental setup and results are discussed in the next section.

## 5. EVALUATION OF SYNCHRONIZATION STABILITY

The synchronization properties of the studied CJCs were evaluated using software simulations and hardware prototype. The first part of this section describes the experimental setup and evaluates some basic electrical properties of the output signal for both CJC types and synchronization errors at different CJC interactive connections. The impact of the slave input voltage drop on the synchronization error is assessed in the second part, and the impact of noise – in the last part of this section.

### 5.1. Setup

Simulations were carried out using *Multisim* model (see Fig. 8) with a maximal time step of $10^{-4}$ s. The structure of the model repeats the design of the prototype circuit (see Fig. 9). Both systems use TL074CD operational amplifiers, which are low cost, high speed, and maintain large gain bandwidth. A conventional 1N4001 silicon diode is used, and a bipolar power supply of ±5 V is applied to the operational amplifiers since the chaotic signal voltage does not exceed ±2 V. The prototype uses four (two per circuit part) low dropout voltage regulators to provide two stable ±5 V power supplies from four 9V batteries.

**Table 1.** Properties of the Master CJC Output Signal

| Model | CJC with direct diode | | | CJC with inverse diode | | |
|---|---|---|---|---|---|---|
| | rms(ac), V | dc, mV | p–p, V | rms(ac), V | dc, mV | p–p, V |
| Multisim | 0.45 | 4.2 | 1.1 | 0.45 | 4.2 | 1.1 |
| Prototype | 0.56 | 276 | 2.05 | 0.53 | -266 | 1.95 |

**Table 2.** Synchronization Errors for Different Circuit Connection Combinations

| Model | Circuit connection type | | | |
|---|---|---|---|---|
| | II sync. error rms, mV | DD sync. error rms, mV | ID sync. error rms, mV | DI sync. error rms, mV |
| Multisim | 0.05 | 0.05 | 210 | 210 |
| Prototype | 0.79 | 0.60 | 530 | 37 |

Some basic electrical properties of both types of master CJC output signals were evaluated (see Table 1). Simulation results are equal for both CJCs, but the prototype shows some differences. Simulations show a little dc value where as the prototype has a relatively significant dc value, which also has an opposite sign for different CJCs. This property of the prototype circuits is probably associated with a small parametric mismatch of the components used (and the imperfection of the operational amplifier) and should be considered an essential impact factor for understanding further experimental results.

Four combinations of interactive CJC connections – II, DD, ID, and DI – were studied, where the first letter denotes the type of master CJC (direct or inverse) and the second letter denotes the type of the slave circuit. According to Table 2, two CJCs of the same type produce much smaller synchronization error than two different coupled circuits, although the prototype has significantly different levels of synchronization error rms voltage for the ID and DI cases. Visual comparisons of synchronization errors for different cases of CJC connections are shown in Fig. 10.

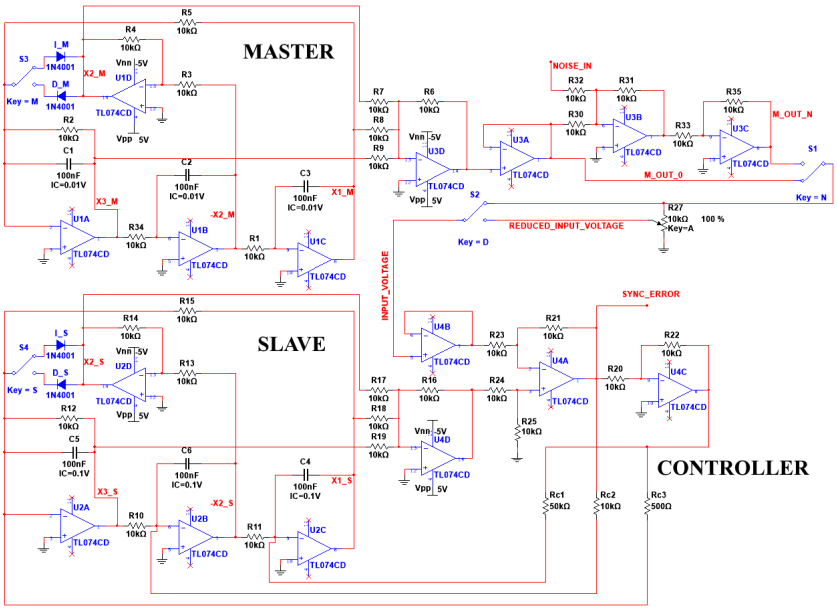


*Fig. 8. Multisim* model of two synchronizable CJCs with selectable noise addition and input voltage drop setup.

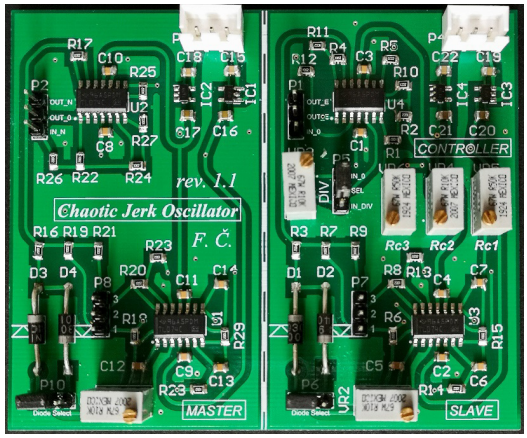


*Fig. 9.* Prototype circuit for evaluating the CJC synchronization properties, assembled on a printed circuit board.

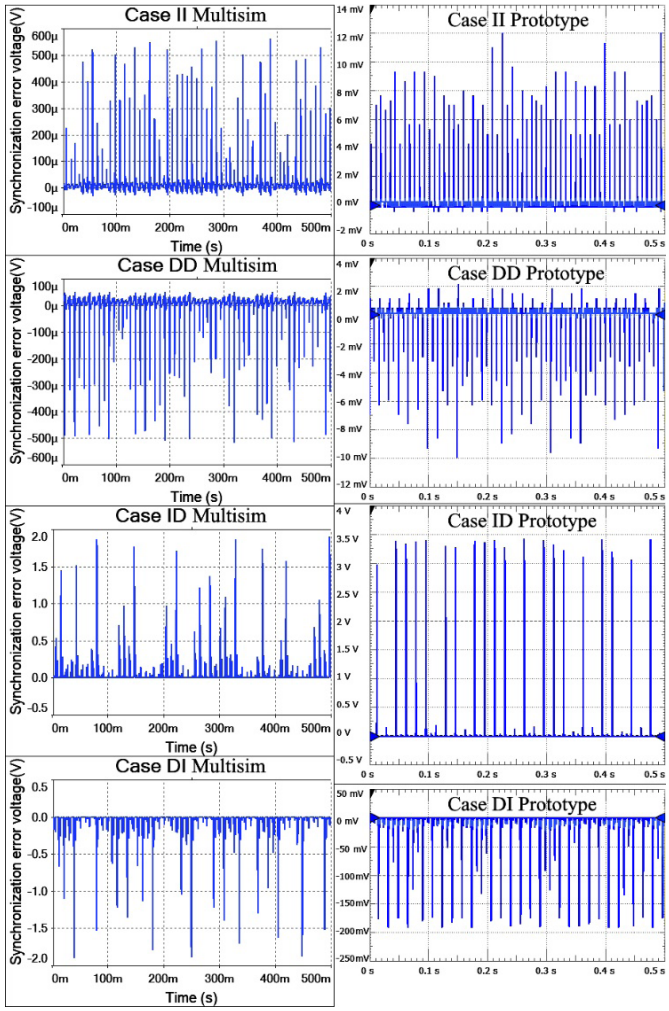


*Fig. 10.* Examples of simulated and experimentally measured synchronization error signals for all cases of possible CJC connections.

## 5.2. Impact of Input Voltage Drop

In order to understand the importance of correct voltage level at the input of a controlled slave CJC, the sustainability of the synchronization error was evaluated as a function of the input voltage drop. A simple potentiometer-based voltage divider was used to linearly ramp down the output voltage of the master CJC before supplying it to the slave CJC controller (see *R27* in Fig. 8).

Simulations of the slave CJC input voltage drop (see Fig. 11, a) show a distinct pattern of synchronization error dependence of input level between two equal and two different types of connected CJCs until the input signal drops to -3 dB from the nominal level. Experimental measurements (see Fig. 11, b) also show significant differences between synchronization errors for the same and different CJCs in range until the input level of the voltage drops by -3 dB. Further decrease of the input voltage merges synchronization errors for all types of connections, making it impossible to use the CSK detection scheme.

A general pattern of the synchronization error signal drop together with the input signal is observed during both simulations and during experimental measurements, but this reduction is not caused by the improvement of synchronization quality. If zero voltage (or ground) is supplied to the controlled slave CJC, the synchronization error signal, as well as all state variables of the slave CJC, will decrease to a near-zero value – such behaviour is predictable from the structure of synchronization scheme used (see Fig. 8). For this reason, the synchronization error rms voltage in Figs. 11 and 12 is normalized (divided) by the slave input rms voltage. In simulations, the normalized synchronization signal remains at the same level when the slave input signal drops below -3 dB, but in the prototype circuit, it is much less steady and increases slowly as the input voltage approaches zero.

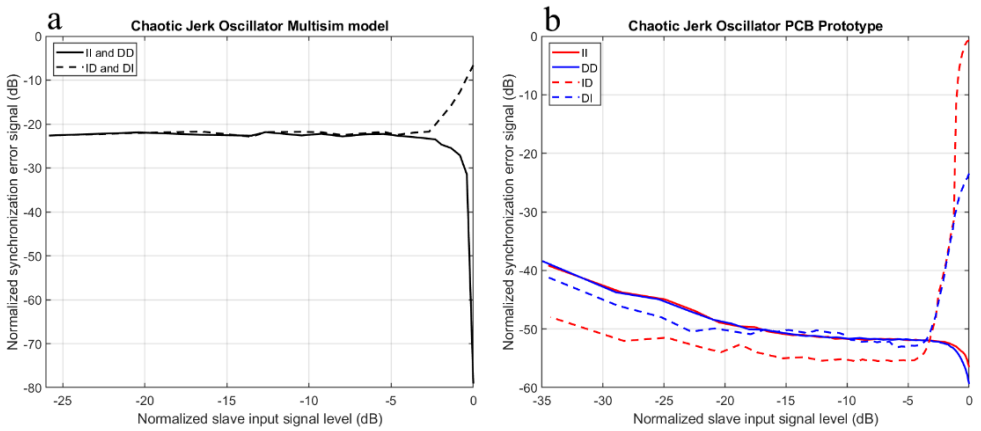


*Fig. 11.* Influence of slave input rms voltage level (normalized by its maximum value) drop on synchronization error rms voltage (normalized by the slave input rms voltage) for different combinations of CJC connections: a – simulated in the *Multisim*; b – measured in the prototype circuit.

If the slave input voltage level drops by 3 dB, the synchronization error (for the cases II and DD) increases, which indicates a degradation of the synchronization quality. In *Multisim* simulation, this degradation starts rather abruptly, but the prototype demonstrates much less synchronization loss at a slightly reduced input voltage.

The significant difference between ID and DI types of CJC interconnections for the prototype becomes minimal after the input voltage drops below -1.25 dB. This fact helps understand that the relatively large synchronization error signal for the ID case is an instability issue in the slave CJC for this specific CJC connection. The slave CJC variables, along with the synchronization error signal, tend to jump to relatively high voltages (see Fig. 10) that are limited by the saturation voltage of the operational amplifiers. Decreasing the input voltage below -1.25 dB no longer pushes the slave CJC to the divergent solutions. This issue is a peculiarity of the prototype circuit and may not repeat or may behave entirely differently in any other prototype circuit made according to the same design.

### 5.3. Impact of Noise

Noise resistance of the synchronization is evaluated by adding white noise to the output signal of the master CJC (see Fig. 8). The bandwidth of the transmitted chaotic signal is approximately 5 kHz, so the noise bandwidth is chosen the same. Simulation results (see Fig. 12, a) show very stable patterns for synchronized (II, DD) and desynchronized (ID, DI) cases of CJC connections that do not overlap or merge within the measured signal-to-noise ratios (SNR), whereas prototype measurements (see Fig. 12, b) show one case of overlap and less regular patterns.

In simulations, the synchronization error level for cases II and DD increases linearly with the noise level. However, in the experimental prototype, both cases show a different nonlinear pattern – for SNRs from 40 to 13 dB, the synchronization error level raises considerably slower than in simulations. However, for SNR below 13 dB, the case II error starts to increase almost linearly with noise, while in the DD case error increases much faster, almost reaching the error level of case ID at zero SNR. It is noteworthy that in the researched prototype, the slave CJC with a direct diode is much less stable. Similarly to the case ID in the previous experiment, when the input voltage in the DD case exceeds (due to the noise added) some specific level, the CJC begins to produce divergent results that lead to short peaks of saturated voltage values. Experimental cases II and DI are more stable than ID and DD, and they resemble simulation results more closely. Different and significant dc voltage offsets, that the prototype CJCs have, possibly are one of the reasons for this instability issue observed in the experiments. It is not a desirable feature and should be avoided in a practical communication system.

Altogether, this experiment did not show any indications of a possible undistinguishable synchronization error for SNRs above 9 dB (when noise rms voltage is about three times less than chaotic signal rms voltage), which should enable the proposed CSK communication at these noise levels. Prototype improvements are required to verify the communication possibility at lower SNR levels, to ensure minimal (and equal) dc voltage bias for CJCs with direct and inverted diode. In addition, the actual minimal transmitted chaotic signal bandwidth that is necessary for a sustainable chaotic synchronization in an ideal environment was not estimated in this study, but such additional research would make it possible to improve the noise immunity of the system by using an appropriate bandpass filter at the input of the receiver.

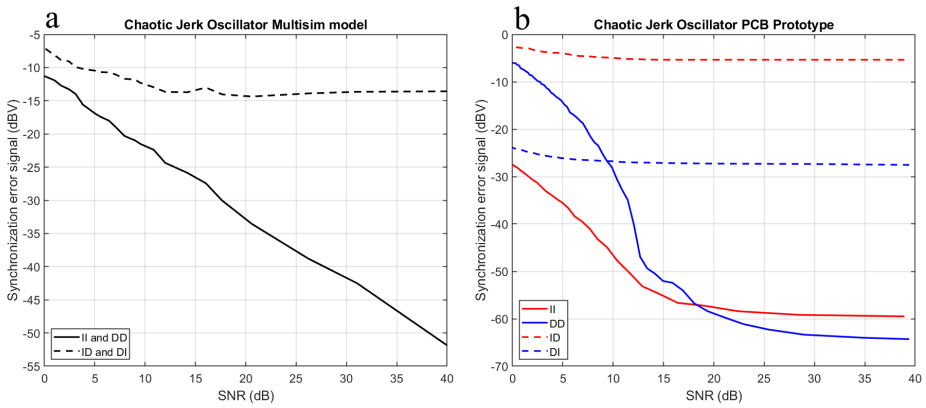


*Fig. 12.* Impact of signal-to-noise ratio on synchronization error rms voltage for different combinations of CJC connections: a – simulated in the *Multisim*; b – measured in the prototype circuit.

## 6. CONCLUSIONS

A coherent CSK communication system that uses two modifications of CJC with controlled error feedback synchronization has been proposed, and the stability of synchronization has been evaluated for different possible couplings between two equal and two different CJCs with respect to input voltage drop and channel noise, using simulations and a prototype circuit.

Synchronization error levels between synchronized (II, DD) and desynchronized (ID, DI) cases of CJC connections are distinguishable for the slave CJC input voltage level above -3 dB from nominal value and for SNRs above 9 dB.

The prototype circuit, created only for CJC synchronization evaluation, has identified several possible system weaknesses, such as dc bias of the chaotic output signal and possible CJC instability issues, that should be carefully considered when designing and implementing the CSK communication system based on the synchronization of the jerk circuits.

According to the results, the proposed digital CSK communication system with CJC synchronization can be practically implemented. However, this study is just the first step in the engineering design process. Further steps of this research should involve a practical implementation of the proposed CSK communication scheme for the evaluation of the impact of noise, interference, multipath propagation, frequency shift and other issues that are common for wireless communication systems.

## ACKNOWLEDGMENTS

The present research has been supported by Riga Technical University 2019/2020 project for strengthening scientific personnel capacity No. MP-2019/5, "Advanced Security Wireless Sensor Network Communication System with Chaotic Synchronization", and by the European Regional Development Fund within Activity 1.1.1.2 "Post-doctoral Research Aid" of the Specific Aid Objective 1.1.1 "To increase the

research and innovative capacity of scientific institutions of Latvia and the ability to attract external financing, investing in human resources and infrastructure" of the Operational Program "Growth and Employment" (No. 1.1.1.2/VIAA/2/ 18/ 345).

## REFERENCES


1. Stavroulakis, P. (2006). *Chaos applications in telecommunications*. CRC Press.
2. Sprott, J. C. (2000). A New Class of Chaotic Circuit. *Phys. Lett. Sect. A Gen. At. Solid State Phys.*, *266* (1), 19–23. doi: 10.1016/S0375-9601(00)00026-8.
3. Sprott, J. C., & Linz, S. J. (2000). Algebraically Simple Chaotic Flows. *Int. J. Chaos Theory Appl.*, *5* (2), 285.
4. Sprott, J. C. (2011). A New Chaotic Jerk Circuit. *IEEE Trans. Circuits Syst. II Express Briefs*, *58* (4), 240–243. doi: 10.1109/TCSII.2011.2124490.
5. Carroll, T. L., & Pecora, L. M. (1991). Synchronizing Chaotic Circuits. *IEEE Trans. Circuits Syst.*, *38* (4), 453–456.
6. Kolumbán, G., Kennedy, M. P., & Chua, L. O. (1998). The Role of Synchronization in Digital Communications Using Chaos - Part II: Chaotic Modulation and Chaotic Synchronization. *IEEE Trans. Circuits Syst. I Fundam. Theory Appl.*, *45* (11), 1129–114. doi: 10.1109/81.735435.
7. Pizolato, J. C., Romero, M. A., & Neto, L. G. (2008). Chaotic Communication Based on the Particle-in-a-Box Electronic Circuit. *IEEE Trans. Circuits Syst. I Regul. Pap.*, *55* (4), 1108–1115. doi: 10.1109/TCSI.2008.916424.
8. Louodop, P., Kountchou, M., Fotsin, H., & Bowong, S. (2014). Practical Finite-Time Synchronization of Jerk Systems: Theory and Experiment. *Nonlinear Dyn.*, *78* (1), 597–607. doi: 10.1007/s11071-014-1463-5.
9. Kaddoum, G. (2016). Wireless Chaos-Based Communication Systems: A Comprehensive Survey. *IEEE Access*, *4*, 2621–2648. doi: 10.1109/ACCESS.2016.2572730.
10. Liu, J., Sprott, J. C., Wang, S., & Ma, Y. (2018). Simplest Chaotic System with a Hyperbolic Sine and its Applications in DCSK Scheme. *IET Commun.*, *12* (7), 809–815. doi: 10.1049/iet-com.2017.0455.
11. Rajagopal, K., Pham, V. T., Çiçek, S., Jafari, S., Karthikeyan, A., & Arun, S. (2020). A Chaotic Jerk System with Different Types of Equilibria and its Application in Communication System. *Teh. Vjesn.*, *27* (3), 681–686. doi: 10.17559/TV-20180613102955.
12. Sambas, A., Ws, M. S., Mamat, M., Karadimas, N. V., & Tacha, O. (2013). Numerical simulations in jerk circuit and its application in a secure communication system. In *Recent Adv. Telecommun. Circuit Des. WSEAS 17th Int. Conf. Commun* (pp. 190–196), 16-19 July 2013, Rhodes Island, Greece.
13. Sambas, A., Sanjaya, M., Mamat, M., & Putra Prastio, R. (2016). Mathematical Modelling of Chaotic Jerk Circuit and its Application in Secure Communication System. *Adv. Chaos Theory Intell. Control. Stud. Fuzziness Soft Comput. Springer*, *337*, 133–153. doi: 10.1007/978-3-319-30340-6.
14. Çiçek, S., Kocamaz, U. E., & Uyaroğlu, Y. (2019). Secure Chaotic Communication with Jerk Chaotic System Using Sliding Mode Control Method and its Real Circuit Implementation. *Iran. J. Sci. Technol. - Trans. Electr. Eng.*, *43* (3), 687–698. doi: 10.1007/s40998-019-00184-9.
15. Nguemkoua Nguenjou, L. P., Kom, G. H., Mboupda Pone, J. R., Kengne, J., & Tiedeu, A. B. (2019). A Window of multistability In Genesio-Tesi Chaotic System, Synchronization and Application for Securing Information. *AEU - Int. J. Electron. Commun.*, *99*, 201–214. doi: 10.1016/j.aeue.2018.11.033.

sciendo

LATVIAN JOURNAL OF PHYSICS
AND TECHNICAL SCIENCES
2021, N 4

DOI: 10.2478/lpts-2021-0034

# METHODS OF FUZZY SET IN SIMULATION FOR PREDICTING UNOBSERVED STATES OF THE ECOLOGICAL AND GEOENGINEERING SYSTEMS

I. Yeremeyev[1], A. Dychko[2*], V. Kyselov[1], N. Remez[2],
S. Kraychuk[3], N. Ostapchuk[3]

[1] Taurida National V.I. Vernadsky University
33 Ivana Kudri, Kyiv, 04000, UKRAINE
[2] Institute of Energy Saving and Energy Management,
National Technical University of Ukraine
"Igor Sikorsky Kyiv Polytechnic Institute"
37 Peremohy Ave., Kyiv, 03056, UKRAINE
[3] Department of Economic Cybernetics,
Rivne State University of Humanities
12 Stepana Bandery Str., Rivne, 33000, UKRAINE
*e-mail: aodi@ukr.net

The present paper provides the ways of implementing methods of fuzzy set approach, which contributes to an increase in the accuracy, efficiency and functional flexibility of the complex control and recognition monitoring systems for the environmental and geoengineering system simulation. They are based on data mining methods and may be implemented with the help of intellectual technologies, including the combination of model pluralism, membership functions, methods of nearest neighbour, results of fractal and chaos theories, methods of ensuring robustness and retrospective analysis of the decision tree for success in decision making in similar situations.

It is proposed to use the model pluralism to explain a particular information process, which uses a number of adequate models, describing the behavior of objects in the case where each of the model reflects its behavior objectively, but under different circumstances, which are difficult to consider a priori in real time when choosing an adequate model. It is shown that the method of the nearest neighbour should be used if it necessary to identify causal relationships and predict further development of the environmental safety events.

***Keywords****: Fuzzy set, environmental simulation, geoengineering system, nearest neighbour method, predicting unobserved states.*

## 1. INTRODUCTION

Modern complex control and recognition systems of the environmental safety management and geoengineering systems monitoring, as a rule, operate in the context of incomplete and fuzzy information, which often affects their effectiveness. In addition, changes and fluctuations in the performance of systems that are probabilistic and fuzzy must be taken into account in the risk management [1]. To improve the efficiency, accuracy and functionality of such systems, different software and hardware solutions are used, that is, ensuring the sufficiency, completeness, timeliness and reliability of information on the basis of which those or other solutions are proposed by generating additional data from data mining methods [2]–[5]. For the identifying, processing, and data analyzing, the intelligence systems are used. Data, generated during the course of operations, including data generated from processes and the additional data, can be structured, semi-structured, or unstructured depending on the nature and conditions of the data use. Due to the amount of data generally generated during the course of operations, intelligence systems are commonly built on top of and utilize a data warehouse [6]. All these make the process of decision making more complicated, unclear and uncertain with appropriate consequences.

The method of "the nearest neighbour" [7] should be used if it is necessary to identify causal relationships and predict further development of the events. The method is based on the estimation of the states of the "nearest neighbours", which are within the accepted limits of the confidence interval $2\sigma$, i.e., the uncertainty interval. Characteristics of the researched object at the point of interest are compared with the data (characteristics) in the nearest (in time or in space) neighbouring points of the object. If a consistent change in the status indicators is observed at all adjacent (right and left) points within the standard deviation, one can assume that there is a certain trend that can be trusted.

The k-nearest neighbour rule is used for an adaptive process monitoring to solve the problems arising from nonlinearity, insufficient training data, and time-varying behaviours [8]. To simplify the process of calculating and making online monitoring possible the rule of a distance-based update is developed.

As it is rightly stated in [9], one cannot consider information without considering any situations of uncertainty. Analysis of the potential impact of the uncertainty of input variables on the performance of the wastewater volume forecasting model shows that a significant influence of the uncertainty of the input variables is demonstrated by water consumption, humidity, rainfall, while duration of sunshine, rainfall depending on certain conditions have a relatively weak impact of uncertainty of input variables [10].

Machine Learning models, including Deep Neural Networks, Convolutional Neural Networks, naïve Bayes and k-Nearest-Neighbour, are proposed to forecast biological species behaviour based on traits, and infer trait connections responsible for species interactions. It is demonstrated that such models are more flexible and informative compared to usual linear models used in ecological research [11].

A model-based diagnosis framework in which a Bayesian approach is used is proposed in Fault Augmented Model Extension work [12]. Fault diagnosis using a Bayesian approach is based on computing

a set of probability density functions, a process that is usually intractable for any reasonably complex system. Approximate Bayesian Computation helps bound the numerical and computational complexity. Such an approach gives a possibility to create probability distributions of possible outcomes and then compare those distributions against actual observations to perform parameter estimation.

The possible imperfections of the proposed methods of fuzzy set approach used for analysis of complex systems, processes and ecological data include the development of the only, more perfect model for simulation.

The above-mentioned aspects require a multi-vector analysis of problems, coverage of these problems from different sides in order to facilitate understanding (for example, based on analogies) and finding more successful ways of informational (including visual) provision of management procedures based on system analysis and data mining. Moreover, the application of such methods in practice is limited by economic and management sectors, or data processing for some ecological research. However, environmental issues are the most complex, fuzzy and uncertain that demand the innovative system approach for their decision.

With the aim of the problem elimination, it is proposed to use the intellectual technologies, including the combination of model pluralism with methods of fuzzy sets, membership functions, methods of nearest neighbours, results of fractal and chaos theories, methods of ensuring robustness and retrospective analysis of the decision tree for successful (by results) choices/decisions to be used in similar situations.

## 2. METHODS OF FUZZY SET APPROACH

Model pluralism, as one of the data mining methods, to explain (understand) a particular information process uses a number of adequate (relevant) models (by nature, usually empirical or semi-empirical) to describe the behaviour of objects in the case where each model reflects its behaviour objectively, but under conditions, difficult to consider a priori in real time.

The effect of uncertainty on the result of process can be demonstrated by the example of a biochemical wastewater treatment or anaerobic digestion system [5]. Such a biochemical technology is a classic model of a system operating under uncertainty: its states (indicators of the degree of contamination of wastewater and treated water by various pollutions) are usually determined not in real time, as well as there is a close, but unambiguous, relationship among external factors (temperature of the environment, atmospheric pressure, rainfall intensity, time during which purification processes take place, etc., and there is also a significant time lag between different events and changes in states of the system). Management of such a system should involve:

- monitoring of the states of the system and the degree of possibility of such states;
- determination of conditions that are impossible according to additional information (for example, wastewater indicators cannot be better or the same as natural water indicators);
- prediction of the states that are not actually observed, but fundamentally possible.

The values of the amplitudes of the actual output data of monitoring of the ecosystem or complex geoengineering system (%) can be presented as a function of time for the three selected models-standards of the response to the calibrated input parameter (for example, a single pulse) (Fig. 1).

Such a model is characterised by its distance (Euclidean metrics) $d_E$ from the distribution of really determined values of the amplitudes $y_i$ and the distribution of values $y_i^m$ corresponding to the $m$-th model:

$$d_E = \sqrt{\frac{1}{n-1} \sum_{i=1}^{n} y_i m} \quad (1)$$

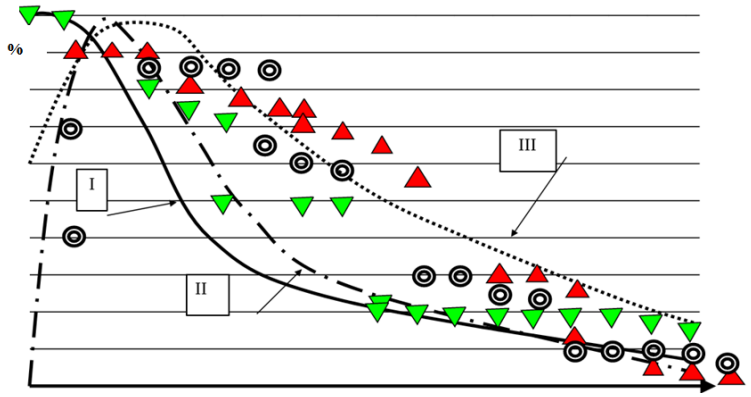


*Fig. 1*. Values of the amplitudes of output data (%) as a function of time for the three selected models-standards of response to the input parameter: n – the number of points at which the amplitudes are determined, m – the model number (I, II, III), ◎, ▲, ▼, – the value of the actually measured parameter (respectively, for the three variants of the real systems).

The use of multiple models instead of the only one allows supplementing the existing "reality" with those "nuances" inherent in alternative models, and provides the more comprehensive assessment of the situation (including behavioral motives) and informed decision making as a rule.

The choice of the optimal model $M_{opt}$ corresponds to the condition:

$$M_{opt} = M\ (min\ \{d^{I}_E,\ d^{II}_E,\ d^{III}_E\}). \quad (2)$$

The following heuristics is proposed to be used to estimate the trend by the "nearest neighbours" method:

$$IF\ [\ \underline{MSTAB}\ ]\ AND\ [\ \underline{SIGN\Delta ST}_{i \pm j}\ EQ],\ THEN\ [\ \underline{SOT}\ ] \quad (3)$$

where *MSTAB* – the situation when the measured value does not exceed the limits of the standard deviation; $SIGN\Delta ST_{i \pm j}\ EQ$ – the observation result, indicating that the sign of the state change at the current measurement at all points to the left and right of *i*, i.e., at points from *i* to *i-j* and from *i* to *i+j*, is the same relative to the state at the same points during the previous measurement or in the spatial distribution; *SOT* – a certain trend is observed (see Fig. 2).

Increase of the state $\Delta x_i$ in case of inconsistent movement of the state indicators at points $x_1 \ldots x_5$ has index 1 (that is $\Delta x_{i1}$), and in case of the consistent movement – index 2 (that is $\Delta x_{i2}$).

The method of comparing the characteristics of the nearest neighbours should not be considered a tool for improving reliability, but it allows estimating at least plausible trends in areas where more exact information is missing (or rather, hidden due to being in the range of uncertainty). However, such a technique in itself broadens boundaries of "vision" of the problem to some extent.

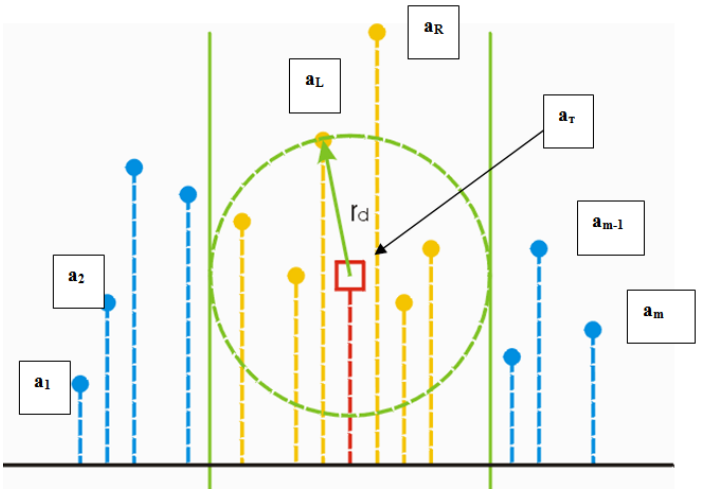


*Fig. 2.* Graphical interpretation of the nearest neighbour method:
$a_1$, $a_2$, $a_{m-1}$, $a_m$ – the measured values of the parameter, $r_d$ – the radius of the boundaries containing the trend values, $a_l$ – the measured value at the trend boundary, $a_R$ – the measured value beyond trend, $a_T$ – the defined value of the parameter.

## 3. PREDICTING UNOBSERVABLE STATES

Predicting unobservable states is one of the main goals of data mining. For the prediction of the states of the ecosystem that are not actually observed, but fundamentally possible, a nonzero degree of possibility $f_M(c)$, less than the minimum degree of possibility $f_M(\alpha)$ calculated for the observed states, is given.

For example,

$$f_M(c) = 0.5 \min_{\alpha} f_M(\alpha), \tag{4}$$

or

$$D_p\left[f_M(c), f_M(\alpha)\right] = \left\{ \frac{1}{n-1} \sum_{c \in C} \left[f_M(c) - f_M(\alpha)\right]^p \right\}^{1/p} \subseteq 0.5 \min_{\alpha} f_M(a) \tag{5}$$

where $p$ – a parameter of the distance function $D_p$ (for the Euclidean distance $p = 2$).

The fact that there is a possibility of predicting unobservable states assumes the connection among the event, the phenomenon and the state of the system. Such a connection does exist, but it is not straightforward and allows only evaluating at a qualitative level the possible states of the system, with a significant (up to a few tens of percent) error.

If we compile a table containing:

- the strata (boundaries within which wastewater pollution indicators may be observed, with appropriate estimates of the probability of observation);
- the set of states capable of observing a measure of zero (boundaries beyond which the observed variables never reach);
- the computed possible states (but not such that can actually be observed);
- the corresponding degrees of feasibility of the state realisation and the probable consequences of this realisation, it is possible to create the conditions for efficient management of processes based on heuristics.

We propose to determine the augmentation of the Euclidean distance (1) between pairs of actually observable states that occur nearby each other at a given time interval, as well as the probability and the possibility of transition from one state to another and the driving forces (internal and external) contributing to it.

The definition of the fundamentally possible states that cannot be recorded online but that may affect the system and its indicators globally, as well as the evaluation their feasibility and expected consequences are proposed further. Here, in the first step, it is necessary to make the definitions on the basis of available data (data from observation of the current process at a certain interval of monitoring). Then, at different levels of refinement, the best hypotheses regarding the feasibility estimates of those or other states of the generalised system are determined. The assumptions about the effect of these hypotheses on the real properties of the researched variables are formed then (these assumptions are formed on the basis of relevant experimental characteristics and specific functions). Finally, the given generalised limit is supplemented (or replaced) by the limits reconstructed with the help of better hypotheses, and each is associated with a degree of confidence. When using only the information contained in the data, the proposed approach allows including in the estimated uncertainty (generalised limit) some characteristics that cannot be established with the real observable data, i.e., it is possible to predict or update, with an estimated degree of certainty, the states of variables not included in the forecast or updated in the observation data.

If the measure of increasing the confidence *MB* to the hypothesis *h* based on the observation of the output *e*:

$$MB[h, e] = \{P(h \mid e) - P(h)\}/(1 - P(h)), \quad (6)$$

where $P(h|e)$ – conditional probability *h* with known *e*, and $P(h)$ – expert evaluation of probability for the specified time interval, then the degree of confidence increasing *MD* relatively *h* may be presented as

$$MD[h, e] = \{P(h) - P(h \mid e)\}/P(h), \quad (7)$$

and the factor of uncertainty *CF* may be presented as

$$CF[h, e] = MB[h, e] - MD[h, e]. \quad (8)$$

The values *MB*, *MD* and *CF*, obtained for every specific event, are placed in the table, which may be used to form the system control heuristics for operation under uncertainty conditions. These heuristics

make it possible to improve the quality of biochemical sewage treatment under conditions of uncertainty and action of the factors which are evaluated weakly.

The above-mentioned situation may be illustrated using the data concerned with quality of wastewater treatment at Zhytomir (Ukraine) treatment facilities (see Fig. 3 and Table 1, created on the basis of Fig. 3).

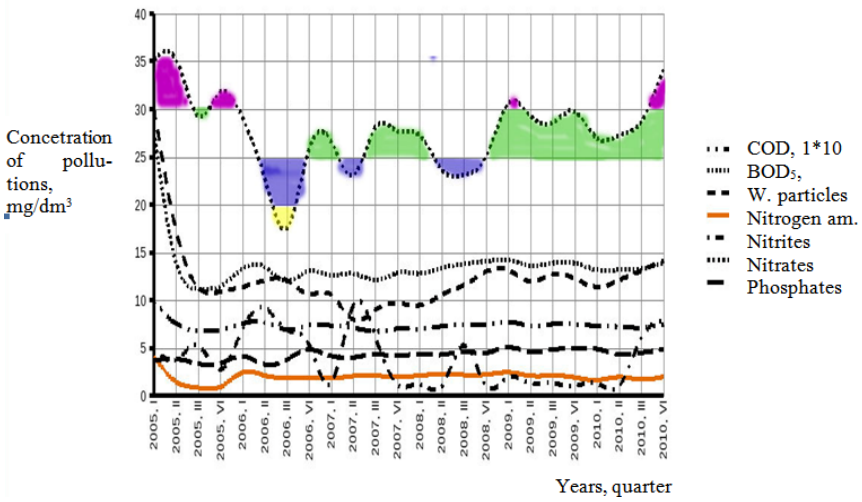


*Fig. 3.* Quality of wastewater treatment at the treatment facilities.

Decision about control action is made on the basis of selection (with the Monte-Carlo approach) of some contamination states (limits of existence, which in linguistic form may be presented as "Great value" (G), "Medium value" (M), "Low value" (L) and "Natural value" (N) (when no control actions are required) accounting the possibility of probability of its realisation. The spectrum of virtual contaminants obtained thus allows for the appropriate regulatory actions to be taken to minimise these contaminants. Thus, if the required ratio of biogenic elements in the aerotank is $BOD_{total}$:N:P=100:5:1, heuristics for the implementation of the feeding of active sludge with nitrogen and phosphorus compounds has the following form:

*IF [{(BOD_M) AND (CNSW_M) AND (CPSW_M)},*
*OR {(BOD_M) AND (CPSW_M)}], THEN {RAS_N},* (9)

*IF{(BOD_G) AND (CNSW_M) AND (CPSW_M)}, THEN {RAS_M},* (10)

*IF{(BOD_G) AND (CNSW_L)}, THEN {RAS_G},* (11)

where *BOD* – values of biological oxygen demands ($BOD_{Total}$) in wastewater (*SW*), *CNSW* – content of nitrogen, *CPSW* – content of phosphorus, *RAS* – replenishment of active sludge, while the probability $P_e$ of heuristic effective operation is calculated as

**Table 1.** The Boundaries of Annual Monitoring of Contamination at Treatment Facilities

| Type of contamination | Maximum value | Minimal value | Stratum | Realisation possibility |
|---|---|---|---|---|
| Biological oxygen demand ($BOD_5$) | 370 mg/l | 175 mg/l | G (370–250) | 0.71 |
| | | | M (250–200) | 0.20 |
| | | | L (200–150) | 0.09 |
| Suspension particles | 30 mg/l | 8 mg/l | G (30–15) | 0.08 |
| | | | M(15–10) | 0.75 |
| | | | L(10–5) | 0.17 |
| Nitrates | 27.5 mg/l | 12 mg/l | G(30–20) | 0.03 |
| | | | M (20–15) | 0.03 |
| | | | L (15–10) | 0.94 |
| Chemical oxygen demand | 100 | 70 | M(100–50) | 1.0 |
| Nitrites | 1.0 | 0.1 | G(1.0–0.5) | 0.3 |
| | | | M (0.5–0.1) | 0.7 |
| Phosphates | 5 | 3 | M (5–1) | 1.0 |
| Nitrogen ammonium | 5 | 1 | M (5–1) | 1.0 |
| pH | 10.6 $O_2$/l | 8.7 $O_2$/l | G(11–10) | 037 |
| | | | M(10–9) | 0,46 |
| | | | L(9–8) | 0.17 |

$$P_e = (1/K) \sum_{k=1}^{K} p_{jk}, \tag{12}$$

where $p_{jk}$ – the probability of realisation of $j$-th strate ($j=\overline{[1, J]}$) of $k$-th parameter (contamination), $K$ – the quantity of the parameters (contamination).

Heuristics for the use of the enhancement process may be formulated as:

*IF [{(VSWP_M) AND (BOD_M) AND (CAS_M) AND (IAS_M)} OR {(VSWP_L) AND (BOD_G) AND (CAS_G) AND (IAS_M)}], THEN (NCP_N),* (13)

*IF{(VSWP_M) AND (BOD_G) AND(CAS_G) AND (IAS_M),THAN(NCP_M),* (14)

*IF {(VSWP_G) AND (BOD_M) AND (CAS_M) AND (IAS_G), THAN(NCP_G),* (15)

where *VSWP* – velocity of *SW* passing; *CAS* – active sludge concentration; *IAS* – the index of active sludge (reflects its properties); *NCP* – necessity of treatment process enhancement.

Practicability of preliminary adjusting of pH level of sewage may be formulated as:

*IF {(LPH_M) AND (VSWP _M)}, THEN (NAL_N),* (16)

*IF{(LPH_L) AND (VSWP_G)}, THEN (NAL_G),* (17)

*IF{(LPH_G) AND (VSWP_L)}, THEN (NAL_M),* (18)

where *LPH* – the level of *pH*, *NAL* – necessity of level of *pH* adjustment.

## 4. CONCLUSIONS

1. Methods of fuzzy set can be implemented for the environmental simulation with the help of intellectual technologies, including the combination of model pluralism with methods of fuzzy sets, membership functions, methods of nearest neighbours, results of fractal and chaos theories, methods of ensuring robustness and retrospective analysis of the decision tree for successful decision making.
2. The use of multiple models of state of the ecosystem or complex geoengineering system instead of the only one allows supplementing the existing data with unobserved one in alternative models, and provides a more comprehensive assessment of the situation (including behavioural motives) and informed decision making.
3. The augmentation of the Euclidean distance between pairs of actually observable states of the geoengineering system allows including in the estimated uncertainty some characteristics that cannot be established with the real observable data, i.e., it is possible to predict or update, with an estimated degree of certainty, the states of variables not included in the forecast or updated in the observation data.
4. The calculation of the boundaries of annual monitoring of contamination at treatment facilities with definition of the stratum and the realisation possibility demonstrates the trends of the process and separate periodic variable processes from catastrophic ones.
5. The use of the created approach allows for effective environment control and management under condition when there is insufficient or fuzzy information about the real state, outward and interior disturbances, and also about their deviations.

## REFERENCES


1. Michna, J., Ekmanis, J., Zeltins, N., Zebergs, V., & Siemianowicz, J. (2012). Innovation Risk Management in the Rational Energy Use (Part 2). *Latvian Journal of Physics and Technical Sciences*, *49* (1), 3–15. doi: https://doi.org/10.2478/v10047-012-0001-9
2. Fayyad, U.M., Candel, A., Ario de la Rubia E., Pafka, S., Chong, A., Lee, J-Y. (2017). Benchmarks and Process Management in Data Science: Will We Ever Get Over the Mess? In *Proceedings of the 23rd ACM SIGKDD International*

*Conference on Knowledge Discovery and Data Mining* (pp. 31–32). doi: https://doi.org/10.1145/3097983.3120998

3. Mika, M. (2017). Interoperability Cadastral Data in the System Approach. *Journal of Ecological Engineering, 18* (2), 150–156. https://doi.org/10.12911/22998993/68303
4. Dychko, A., Yeremeyev, I., Kyselov, V., Remez, N., & Kniazevych, A. (2019). Ensuring Reliability of Control Data in Engineering Systems. *Latvian Journal of Physics and Technical Sciences*, *56* (6), 57–69. doi: https://doi.org/10.2478/lpts-2019-0035
5. Dychko, A., Remez, N., Kyselov, V., Kraychuk, S., Ostapchuk, N., Kniazevych, A. (2020). Monitoring and Biochemical Treatment of Wastewater. *Journal of Ecological Engineering*, *21* (4), 150–159. doi: https://doi.org/10.12911/22998993/119811
6. Johnston, M., & Kazemzadeh, E. (2018). U.S. Patent No. 10,114,612. Washington, DC: U.S. Patent and Trademark Office.
7. Han, J., Pei, J., & Kamber, M. (2011). *Data mining: Concepts and techniques*. Elsevier.
8. Zhu, W., Sun, W., & Romagnoli, J. (2018). Adaptive k-Nearest-Neighbor Method for Process Monitoring. *Industrial & Engineering Chemistry Research, 57* (7), 2574–2586. doi: 10.1021/acs.iecr.7b03771
9. Diduk, N.N. (2014). The Measures of Internal and External Information (on Example of Probabilistic Situations of Uncertainty). Part IV. *System Research and Information Technologies, 1*, 113–129.
10. Jurasz, J., Piasecki, A., & Kaźmierczak, B. (2019). Sewage Volume Forecasting on a Day-Ahead Basis – Analysis of Input Variables Uncertainty. *Journal of Ecological Engineering*, *20* (9), 70–79. doi: https://doi.org/10.12911/22998993/112507
11. Pichler, M., Boreux, V., Klein, A., Schleuning, M., & Hartig F. (2019). Machine Learning Algorithms to Infer Trait-Matching and Predict Species Interactions in Ecological Networks. *Methods in Ecology and Evolution, 11,* 281–293. doi: 10.1111/2041-210X.13329
12. Minhas, R., Kleer, J., Matei, I., Bhaskar, S., Janssen, B., Bobrow, D.G. & Kurtoglu, T. (2014). Using fault augmented modelica models for diagnostics. In *Proceedings of the 10th International Modelica Conference 2014* (pp. 437–445), 10-12 March 2014, Lund, Sweden. Linkping University Electronic Press. doi: https://doi.org/10.3384/ecp14096437